

# CAAP Annual Report

**Date of Report:** 09/27/2023

**Prepared for:** U.S. DOT Pipeline and Hazardous Materials Safety Administration

**Annual Period:** From (09, 27, 2022) to (09, 27, 2023)

**Contract Number:** 693JK32250009CAAP

**Project Title:** *All-in-One Multifunctional Cured-In-Place Structural Liner for Rehabilitating of Aging Cast Iron Pipelines*

**Prepared by:** Ying Huang

**Contact Info.:** 701-231-7651, [ying.huang@ndsu.edu](mailto:ying.huang@ndsu.edu)

## **Table of Contents**

Table of Contents .....	2
Section A: Business and Activities .....	4
(a) Contract Activities .....	4
(b) Financial Summary .....	7
(d) Status Update of the 4 <sup>th</sup> Quarter Technical Activities .....	9
Section B: Detailed Technical Results in the Report Period .....	10
1. Background and Objectives in the 1 <sup>st</sup> Annual Report Period .....	10
1.1. Background .....	10
1.2. CIPP Pipeline Liner .....	10
1.3. Task 2 Recent Development of Vitrimers and Their Application as Self-Healing Polymer .....	11
1.4. Task 3.1 High-performance Modified Epoxy .....	12
1.5. Task 3.3 Chemical Analysis of Surface Bonding and Permeability .....	12
1.6. Task 3.4 Finite Element Modeling of CIPP Liners .....	13
1.7. Task 4 Monitoring of CIPP Liners with Fiber Optical Sensors .....	14
1.8. Task 5 Risk Analysis of Pipelines and Liners .....	15
1.9. Objectives in the 1 <sup>st</sup> Annual Report Period .....	18
2. Experimental Program in the 1 <sup>st</sup> Annual Report Period .....	18
2.1. Experimental Design .....	18
2.2. Test Procedure .....	20
2.2.1. Task 2 Development of healable and sustainable CIPP structural liner .....	20
2.2.2. Task 3.1 and 3.2 Nanocomposite characterization and Performance evaluation .....	21
2.2.3. Task 3.3 Finite element numerical analysis (FEA) .....	26
2.2.4. Task 3.4 Reducing the permeability and investigating the interfacial bonding chemical analysis .....	30

2.2.5. Task 4 Enabling self-sensing for the developed CIPP structural liner .....	32
2.2.6. Task 5.1 Development of CIPP liner risk index for the pipeline integrity management enhanced by AI algorithms.....	32
3. Results and Discussions.....	35
3.1. Task 2 Development of healable and sustainable CIPP structural liner .....	35
3.2. Task 3 Enhancing mechanical and bonding performances and reducing permeability of the healable CIPP structural lining through nanofiller .....	42
3.3. Task 4 Enabling self-sensing for the developed CIPP structural liner .....	63
3.4. Task 5 Integration of the multifunction with the pipeline integrity management system .....	65
4. Future work.....	69
References.....	71

## **Section A: Business and Activities**

### **(a) Contract Activities**

- Contract Modifications: N/A
- Educational Activities:
  - Student mentoring:

#### *North Dakota State University*

1. Xingyu Wang, Postdoc Research Fellow, Department of Civil, Construction, and Environmental Engineering, Advisor: Ying Huang, 10/01/2022-current
2. Tofatun Jannat, Ph. D. Student, Department of Civil, Construction, and Environmental Engineering, Advisor: Ying Huang, 10/01/2022-current
3. Leonard Chia, Ph. D. Student, Department of Civil, Construction, and Environmental Engineering, Advisor: Ying Huang, 10/01/2022-08/15/2023
4. Yasir Mahmood, Ph. D. Student, Department of Civil, Construction, and Environmental Engineering, Advisor: Ying Huang, 01/01/2023-current
5. Zahoor Hussain, Ph. D. Student, Department of Civil, Construction, and Environmental Engineering, Advisor: Zhibin Lin, 01/01/2023-current
6. Austin Knight, Ph. D. Student, Department of Mechanical Engineering, Advisor: Long Jiang, 01/01/2023-current
7. Kathryn S. Quenette, Undergraduate Student, Department of Civil, Construction, and Environmental Engineering, Advisor: Ying Huang, 01/01/2023-current

#### *Purdue University*

1. Junyi Duan, Ph.D. Student, School of Construction Management Technology, Advisor: Chengcheng Tao, 9/27/2022-current
2. Xiaoyue Zhang, Ph.D. Student, School of Construction Management Technology, Advisor: Chengcheng Tao, 9/27/2022-7/1/2023
3. Yizhou Lin, Ph.D. Student, School of Construction Management Technology, Advisor: Chengcheng Tao, 8/15/2023-current

#### *University of Oklahoma*

1. Qiuhaio Chang, Ph.D. Student, Department of Sustainable Chemical, Biological and Materials, Advisor: Liangliang Huang, 10/01/2022-05/15/2023

2. Madeleine C. Oliver, Ph. D. Student, Department of Sustainable Chemical, Biological and Materials, Advisor: Liangliang Huang, 10/01/2022-current
  - Student internship:
 

Madeleine C. Oliver, 05/15/2023-08/15/2023, Internship at Los Alamos National Laboratory.
  - Educational activities:
    1. On Oct 25<sup>th</sup> 2022, Dr. Huang and the graduate students, Leonard Chia, Yasir Mahmood, offered a half-day BrainSTEM workshop (8am-1:30pm) to 7<sup>th</sup> graders in Fargo-Moorhead (F-M) Community on “Pipeline Challenges” with hands-on projects for students to explore pipeline concepts. The workshop provided outreach on pipeline to a total of 60 7<sup>th</sup> graders in the F-M community.
    2. From Dec 23<sup>th</sup> 2022 to Jan 2<sup>nd</sup> 2023, Dr. Huang and the graduate student, Leonard Chia, offered a seven-day camp session to the YMCA School Age Learning Center at Fercho Site, Fargo, ND. The camp provided outreach to elementary school age students on pipeline to a total of more than 150 elementary students in F-M community.
    3. Dr. Tao worked with Purdue K-12 Science Outreach programs on K-12 Superheroes of Science education videos related to sustainable and resilient infrastructure. Undergraduate students Gracyn Wyman, Andraya Fuller, Joy Gao and Ph.D. student Junyi Duan, Xiaoyue Zhang at Purdue University worked as volunteers in filming the videos.
  - Career employed:
 

Leonard Chia, 08/15/2023 employed by Intertek PSI;

Qiu hao Chang, 07/01/2023, employed by University of Canterbury, New Zealand.
  - Others: N/A
- Dissemination of Project Outcomes:
  1. Junyi Duan, Ph.D. student in the School of Construction Management Technology at Purdue University, won the 2<sup>nd</sup> place at Purdue Polytechnic Institute (PPI) Research Impact Areas (RIA) - Holistic Safety and Security (HSS) - Student Poster Symposium for his poster presentation from this project “*Numerical Analysis of Cured-in-place Pipe Structural Liner for Underground Pipeline Rehabilitation*”, Purdue University, West Lafayette, IN, March 24, 2023.
  2. Junyi Duan and Xiaoyue Zhang, Ph.D. students in the School of Construction Management Technology at Purdue University presented two conference papers “*Numerical analysis of cured-in-place pipe structural liner for underground pipeline*”

*rehabilitation*” and “*Machine learning-based risk model for pipeline integrity management*” at the ASCE International Conference on Computing in Civil Engineering (i3ce 2023), Corvallis, OR, June 25 - 28, 2023.

Citations of The Publications:

1. Zhang, D., Huang, Y., Xu, L., Tao, C., Yang, X., and Wang, X. (2023). Synergistic effects of nanoparticle geometric shape and post curing on carbon-based nanoparticle reinforced epoxy coatings: Characterization, microstructure, and adhesion properties. *Progress in Organic Coatings*, 185, 107929. (Published)
2. Zhang, D., Huang, Y., Xia W., Xu L., and Wang X. (2023) "Dispersion characteristics and mechanical properties of epoxy nanocomposites reinforced with carboxymethyl cellulose (CMC) functionalized nanodiamond (ND), carbon nanotube (CNT), and graphene (GNP)." *Polymer Composites*. (Accepted)
3. Duan, J., Tao, C., and Huang, Y. (2023). Numerical analysis of cured-in-place pipe structural liner for underground pipeline rehabilitation. ASCE International Conference on Computing in Civil Engineering, Corvallis, Oregon, June 25 - 28, 2023.
4. Zhang, X., Tao, C., and Huang, Y. (2023). Machine learning-based risk model for pipeline integrity management. ASCE International Conference on Computing in Civil Engineering, Corvallis, Oregon, June 25 - 28, 2023.
5. Duan, J., Tao, C., and Huang, Y. (2023). Computational modeling of cured-in-place structural liner for aged pipeline rehabilitation. ASCE Infrastructure Innovation & Adaptation for a Sustainable & Resilient World (INSPIRE) conference, Arlington, VA, Nov 16-18, 2023. (accepted)
6. Zhang, X., Tao, C., and Huang, Y. (2023). Risk assessment models for pipeline infrastructure failure. ASCE Infrastructure Innovation & Adaptation for a Sustainable & Resilient World (INSPIRE) conference, Arlington, VA, Nov 16-18, 2023. (accepted)
7. Duan, J., Tao, C., and Huang, Y. (2024). Finite element analysis of structural lining materials for pipeline rehabilitation. ASCE Construction Institute (CI) and Construction Research Congress (CRC) Joint Conference 2024, Des Moines, IA, March 20-23, 2024. (accepted)
8. Duan, J., Tao, C., and Huang, Y. (2024). Pipeline integrity analysis through data-driven approaches. ASCE Construction Institute (CI) and Construction Research Congress (CRC) Joint Conference 2024, Des Moines, IA, March 20-23, 2024. (accepted)

Manuscripts of the publications have been submitted on the reporting website.

- Others: N/A

**(b) Financial Summary**

- Federal Cost Activities:
  - PI/Co-PIs/students involvement:

The PIs and student involvements and other expenditures of the project are detailed in Table 1 below. The table is a summary of all the expected expenditure till September 30<sup>th</sup> 2023. A total expenditure of Year (Yr) 1 is expected to around \$7,1387.62. The annual financial report till June 30<sup>th</sup> 2023 is also submitted in the reporting website. The next financial report till September 30<sup>th</sup> 2023 will be available on Oct 2<sup>nd</sup> 2023 and will be updated to PHMSA on that date. The actual final financial report may have a slight difference with the table below due to the gap between the report and the availability of next financial report.

Table 1 Summary of Yr 1 spending

<i>Institution</i>	<i>Category</i>	<i>Amount (\$)</i>	<i>Amount (\$)</i>	<i>Subtotal (\$)</i>
<i>North Dakota State University</i>	<i>Personnel</i>	<i>Salary (\$)</i>	<i>Benefit (\$)</i>	
	<i>PI: Y Huang</i>	<i>8839</i>	<i>1825</i>	<i>10664</i>
	<i>Co-PI: Z. Lin</i>	<i>10200</i>	<i>2055</i>	<i>12255</i>
	<i>Co-PI: L. Jiang</i>	<i>11302</i>	<i>2334</i>	<i>13636</i>
	<i>Postdoc: X. Wang</i>	<i>10710</i>	<i>7427</i>	<i>18137</i>
	<i>Ph. D. Students</i>			
	<i>Tofatun Jannat</i>	<i>5625</i>	<i>12.68</i>	<i>5637.68</i>
	<i>Leonard Chia</i>	<i>3825</i>	<i>8.85</i>	<i>3833.85</i>
	<i>Yasir Mahmood</i>	<i>3600</i>	<i>8.34</i>	<i>3608.34</i>
	<i>Austin Knight</i>	<i>5100</i>	<i>307</i>	<i>5407</i>
	<i>Undergraduate Student</i>			
	<i>Kathryn S. Quenette</i>	<i>1065</i>	<i>2.23</i>	<i>1067.23</i>
	<i>Materials</i>			<i>27447</i>
	<i>Operation fee</i>			<i>9644.3</i>
	<i>Travel</i>			<i>0</i>
	<i>Consultant: RagulaTech</i>			<i>2475</i>
	<i>Total Direct</i>			<i>40634</i>
	<i>Indirect</i>			<i>18285.1</i>
	<i>Subtotal</i>			<b><i>58918.62</i></b>
	<i>Purdue University</i>	<i>Co-PI: C. Tao</i>	<i>6102</i>	<i>1830.66</i>
<i>Ph. D. Students</i>				
<i>Junyi Duan</i>		<i>0</i>	<i>0</i>	
<i>Xiaoyue Zhang</i>		<i>0</i>	<i>0</i>	
<i>Materials</i>				<i>111.85</i>
<i>Travel</i>				<i>0</i>
<i>Indirect</i>				<i>4424.49</i>
<i>Subtotal</i>				<b><i>12469</i></b>

<i>University of Oklahoma</i>	Co-PI: L. Huang	0	0	0
	<i>Ph. D. Students</i>			
	Qiuhao Chang	0	0	0
	Madeleine C. Oliver	0	0	0
<i>Total</i>				<b>71387.62</b>

o Cost Share Activities:

- o Cost share contribution: The table below details the cost share in NDSU and Purdue during Yr 1 of the project. A total of \$40,435.4 was provided as match fund in Yr 1.

Table 2 Summary of Yr 1 cost share

<i>Institution</i>	<i>Category</i>	<i>Amount (\$)</i>
<i>North Dakota State University</i>	Graduate Tuition	
	Tofatun Jannat	3394.2
	Leonard Chia	4582.09
	Yasir Mahmood	6874.22
	Indirect	7177.73
	Subtotal	23128.25
<i>Purdue University</i>	Faculty salary	2887.44
	Graduate Salary and Tuition from Purdue Office of Research - Executive Vice President for Research and Partnerships	16267.96
	Graduate Salary and Tuition from School of Construction Management	18180
	Travel	3100
	Subtotal	40435.4

**(c) Project Schedule Update**

- Project Schedule:

According to the project schedule planned in the proposal as shown in Table 3 below, we are on schedule (X in table indicated the portion of that task has been completed).

Table 3 Project schedule and Yr 1 accomplishments

Tasks (Milestones, Completion Date)	Year 1				Year 2				Year 3			
	Q1	Q2	Q3	Q4	Q1	Q2	Q3	Q4	Q1	Q2	Q3	Q4
Task 1 (Milestone 1) (M.1: 01/10/2023)	x											
Task 2 (Milestone 2) (M.2: 10/10/2024)	x	x	x	x								

Task 3 (Milestone 3) (M.3: 01/10/2025)	x	x	x	x								
Task 4 (Milestone 4) (M.4: 04/10/2025)		x	x	x								
Task 5 (Milestone 5) (M.5: 07/10/2025)			x	x								
Task 6 (Milestone 6) (M.6: 09/30/2025)	x	x	x	x								

- Corrective Actions: N/A

**(d) Status Update of the 4<sup>th</sup> Quarter Technical Activities**

Please refer to the submitted 4<sup>th</sup> quarterly report.

## **Section B: Detailed Technical Results in the Report Period**

### **1. Background and Objectives in the 1<sup>st</sup> Annual Report Period**

#### **1.1. Background**

This project is designed to develop and test the feasibility of an all-in-one multifunctional Cured-In-Place Pipe (CIPP) structural liner that is self-healing and self-sensing with high performance. Specifically, the all-in-one CIPP structural liner has the following innovations to achieve the multifunction: 1) the healing capacity is enabled by using the solvent-free and catalyst-free vitrimer epoxy/anhydride and/or epoxy/acid resins for recyclable, sustainable, and environmental friendly liner applications; 2) the high performance is achieved by modifying the epoxy resin using surface treated nanofillers (e.g. carbon nanotubes) and guided by molecular dynamics simulation and computational finite element analysis to enhance the liner's mechanical and bonding properties and reduce the permeability; and 3) the self-sensing function is supported by embedding distributed fiber optic sensors along with the fabric of the liner to monitor its health condition during installation and service, such as damages, debond, cracks, etc., and by integrating with the artificial intelligence to develop a CIPP liner risk index for risk assessment and integrity management. Upon validation, the multifunction of such an all-in-one CIPP structural liner can be partially or fully implemented with commercially available CIPP solutions to enhance the sustainability and reliability of CIPP technologies in practice for better mitigating risks of the repaired aging cast iron pipelines. In the first quarter of this project, literature review was expected to direct the research to the right direction for the development of the all-in-one liner in future quarters.

#### **1.2. CIPP Pipeline Liner**

Currently, the United States still has 26,060 miles of cast iron pipelines in service. These cast iron pipelines mostly have a service period of more than a hundred year. With aging and corrosion, some of them may leak or crack and need to be repaired, rehabilitated, or even replaced. Replacing leaking pipeline segments using open-trench approach is the most common practice. However, it may not be feasible to replace the pipeline segments using open-trench method in some circumstances, such as when the pipelines are in highly populated areas, in areas with congested pipeline systems and do not have sufficient right-of-way space for open trench, or in areas where it is not cost-effective for excavation and restoration costs. In these circumstances, trenchless technologies became a potential alternative to rehabilitate the aging cast-iron pipelines [1]. There are two major trenchless technologies to rehabilitate oil and natural gas production applications, including the composite pipes and the CIPP structural liners. The commercially available composite pipes include the primus line [2], the high-density polyethylene smart pipe, FlexSteel pipe, Fiberspar LinePipe [3], the Polyflow Thermoflex Tubing, and the Flexpipe system. Many of the composite pipes are spoolable pipes manufactured in various sizes and in continuous lengths up to 35,000 ft for pipes of small diameters. These composite pipes usually have an internal thermoplastic liner surrounded by laminates made of carbon, glass, or other fibers in an epoxy

resin base as the pressure-carrying components of the composite. The use of those different materials allows for high pressure ratings for those pipes to be utilized for transmission lines. Although the applications of composite pipes can bear high pressures, the expensive cost and the small diameter features have limited their wide applications [1].

To seek more affordable and flexible trenchless alternatives for preventing pipeline leakage and increasing the service life of cast-iron pipelines, the CIPP liner has evolved into a well-accepted technology in practice [1,4]. Worldwide, it is estimated that nearly 75,000 miles of pipelines, including natural gas pipes, water and wastewater pipes, have been rehabilitated with CIPP liners, with nearly \$3 billion spent annually on the trenchless renovation method. The CIPP liner (e.g. Starline HPL-G29) is a hollow cylinder containing a non-woven or woven fabric material impregnated by a cured thermosetting resin. The resin is impregnated into the fabric in a factory and prefabricated and transported to sites. Then, the liner is installed by using inversion or pulled in place technique at the construction site and the thermosetting resin is cured in place to bond the liner tightly to the existing pipe [1]. Thus, the CIPP liner can be installed remotely inside existing underground cast-iron pipelines with minimum outside disturbance through trenchless construction procedures [5,6]. The most commonly used Starline HPL-G liner can rehabilitate a high-pressure pipeline with a diameter up to 24 inches with existing and future pitting corrosion of up to 2 inches or cracks up to 1 inch under an operating pressure up to 250 psig [7]. The Starline HPL-G liners have shown efficiencies in removing those pipeline defects fast, while accommodating bends and changes at the pipe cross-section of the pipe. Previous studies focused on developing advanced equipment and installation techniques, establishing limit state design approaches for the linings [8,9], and quantifying the effects of imperfections that may result from the installation process.

### **1.3. Task 2 Recent Development of Vitrimers and Their Application as Self-Healing Polymer**

Thermosetting resins used in Cured-In-Place Pipe (CIPP) liners primarily include epoxy resin, unsaturated polyester, and vinyl ester resin, especially for applications requiring chemical resistance. Epoxy resin is a popular choice due to its unique properties, such as low shrinkage, low viscosity, strong adhesion, and desirable thermal and mechanical characteristics. However, conventional anhydride-cured epoxy resin curing can be slow, incomplete, and complex without catalysts, making repairs and recycling challenging due to their infusible and insoluble nature once cured. Developing environmentally friendly or reusable epoxy alternatives, like vitrimer polymers, has garnered significant attention.

*Self-healing coatings*, using materials like vitrimers, have gained traction as they can sustain numerous healing cycles with minimal external intervention, often involving temperature or light adjustments. Recent advancements include ultra-thin self-healing vitrimer coatings, which maintain hydrophobicity and transparency even after damage, and the ability to apply these coatings to various substrates.

*Recyclability of vitrimers* is another key area of interest, with studies showing that vitrimer products can be ground into fine powder and hot-pressed to create new products. This recycling process has been successful in maintaining the mechanical properties of the original material, highlighting its potential for sustainability.

*Biobased vitrimers*, which combine vitrimers with renewable biopolymers like lignin, offer a promising avenue for creating high-performance and sustainable materials. Lignin, found in wood and various plant sources, provides functionality through its abundant hydroxyl groups, making it suitable for use in vitrimers.

*UV-cured vitrimers*, which utilize UV or combined UV and thermal curing, have gained popularity due to their cost-effectiveness and efficiency. These vitrimers can offer flame resistance and mechanical robustness, making them suitable for various applications.

In conclusion, vitrimers represent an exciting development in the field of thermosetting polymers, offering the potential for self-healing, recycling, and sustainability. These materials, which have been introduced relatively recently, rely on covalent bond exchange mechanisms to achieve their unique properties. The combination of vitrimers with bio-based monomers and the exploration of their fundamental physics and flow characteristics hold promise for a more sustainable future. Further research and development in vitrimer technology can open up new application domains and contribute to the realization of a sustainable society.

#### **1.4. Task 3.1 High-performance Modified Epoxy**

In the recent decade, the development of high-performance nanocomposites has gained significant attention due to their potential to revolutionize research fields and industries. The shape and concentration of the nanoparticles used as reinforcements are critical factors influencing the performance of nanocomposites. To investigate these effects, this study focuses on evaluating the influence of nanoparticle morphology, including carbon nanotubes (CNT), graphene nanoplatelets (GNP), and nanodiamonds (ND), on the performance of epoxy-based nanocomposites. CNT, GNP, and ND are well-known nanoparticles having typical 1-D, 2-D, and 0-D microstructures, respectively [10,11]. Furthermore, the study explores how varying weight concentrations of these nanoparticles can impact the overall properties of the composites, as well as the influence of the shape of the nanoparticles.

In order to comprehend the impacts of different nanoparticle shapes and concentrations on the performance of nanocomposites, carbon nanotubes, graphene nanoparticles, and nanodiamonds were introduced into an epoxy matrix at concentrations of 0.5, 1.0, and 2.0 wt.%. Comprehensive experimental studies and analyses have been conducted to assess the performance of the nanocomposites. These include transmission electron microscopy (TEM) imaging of the nanoparticles, particle size distribution, viscosity tests, tensile properties tests, abrasion resistance tests, coating adhesion strength, and water contact angle tests. The results of these performance evaluations will provide valuable insights into the effect of nanoparticle shape and concentration on the resulted properties of the nanocomposites. This information will contribute to the ongoing research of this project about the development of an all-in-one liner with superior mechanical and durability properties.

#### **1.5. Task 3.3 Chemical Analysis of Surface Bonding and Permeability**

To analyze the surface bonding of the CNT-modified healable epoxy resin, it is needed to analyze the chemistry at the CNT-modified healable epoxy resin/cast-iron interface and to evaluate the permeability of methane, carbon dioxide and their mixtures over a range of temperatures and

pressures which are of interest to field applications.

*(a) Force Field:* The COMPASS (Condensed-Phase Optimized Molecular Potentials for Atomistic Simulation Studies) force field, derived from the Polymer Consistent Force Field (PCFF), is employed to model polymer segments and their interactions in molecular dynamics (MD) simulations. This force field is extensively validated using condensed-phase properties and empirical data, enabling predictions of various polymer properties. Free volume is assessed using Voronoi tessellation and cavity enumeration techniques. The expected outcomes encompass an atomistic composite model and its temperature-dependent structural changes.

*(b) Binding at the Interface:* This project aims to understand the formation and chemistry of the interface in CNT-modified healable epoxy resin/cast-iron models. Ab initio density functional theory (DFT) calculations will investigate the nature of the interface and bonding between epoxy resin segments and cast-iron (Fe (110) facet), focusing on atoms at the interface due to computational cost constraints. Experimental data, like positron annihilation lifetime measurements, will be used as references to adjust simulation parameters. The VASP software, with van der Waals interaction correction, will be used for DFT calculations.

*(c) Structural and Mechanical Properties of the Interface Model:* The project involves calculating stress-strain properties, specifically Young's modulus, to assess the stiffness of the interface model. Various computational methods, such as box length enlargement and continuous elongation, will be employed to determine Young's modulus. The point of yielding and yield strength will also be determined from stress-strain diagrams. These properties play a crucial role in understanding the material's mechanical behavior.

*(d) Permeability Calculations:* MD simulations will be used to evaluate permeability in polymer networks, focusing on CH<sub>4</sub>, CO<sub>2</sub>, and their mixtures. Permeabilities will be assessed using Fick's First Law, transition rates, and a Bayesian analysis of the inhomogeneous solubility-diffusion model. Rigid composite models will be adopted unless experimental evidence suggests otherwise. Different models will represent CH<sub>4</sub> and CO<sub>2</sub>. Properties such as self-diffusion coefficients, molecular orientation, density profiles, atomic fluctuations, permeability, and selectivity will be calculated and compared to experiments. The study will provide insights into how interaction, permeability, and selectivity change with time, temperature, and pressure. Both CPU and GPU versions of LAMMPS will be used for MD calculations.

### **1.6. Task 3.4 Finite Element Modeling of CIPP Liners**

In addition to assessment and monitoring technologies, numerical analysis plays a crucial role in studying the performance of Cured-in-Place Pipe (CIPP) liners. In this section, we concentrate on finite element modeling of CIPP liners, specifically addressing their mechanical performance and the bond between the liner and the pipeline. The forthcoming finite element analyses will significantly contribute to the development of high-performance CIPP liners for this project:

*(a) General Mechanical Properties Analysis:* 3D numerical models can be used to assess the mechanical properties of pipelines after rehabilitation using Cured-in-Place Pipe (CIPP) technology. Factors such as cover depth, CIPP thickness, traffic load, and fluid load are critical. Notably, the axial bending stress becomes critical when the void diameter to pipe inside diameter

ratio approaches unity.

*(b) Pipeline Performance with CIPP Enhancement:* The presence of CIPP significantly improves pipeline integrity and safety. The width of pipe corrosion is inversely related to CIPP thickness but positively correlated with corrosion depth, traffic load, cover depth, and water quantity.

The composite liner can be simulated as a homogenous material, and finite element analysis (FEA) is used to predict liner conditions during the installation process. Pull-in-place installation is discussed, considering the relationship between liner inflation and the number of wrap tapes. CIPP lining can reduce stress concentration and displacement differences in damaged pipes, leading to a 45% to 70% reduction in stress and displacement after installation. Liner thickness has a relatively minor effect on rehabilitation.

*(c) Elastic Buckling Analysis:* The elastic buckling behavior of polyhedral polymer structural liners can be studied under external hydrostatic pressure using analytical methods and FEA. Factors affecting buckling pressure are discussed, including thickness-to-radius ratio and polygon base shape. The gas permeation can affect the modulus and critical buckling pressure of HDPE liners. Higher temperatures have a detrimental effect on critical buckling stress.

*(d) Crack Effects and Buckling Behavior:* FEA can be used to investigate the effects of liners on pipes with different crack patterns. The study concludes that circumferential cracks have a smaller impact on buckling strength than axial cracks. Liner stiffness and thickness influence the critical crack length and buckling behavior.

*(e) Varying Liner Thickness:* Numerical analysis explores the buckling behavior of pipes with varying liner thickness, revealing that pipes with decreasing thickness from bottom to top have lower critical pressure.

*(f) Gas Penetration and Debonding:* High-pressure conditions can lead to gas penetration and debonding in the polymer layer of the liner. Different material models are evaluated, with elastoplastic with strain hardening being the most suitable.

*(g) Combined Effects of Pressure and Cover Depth:* The combined effect of internal pipe pressure and cover depth on CIPP liners is studied, showing stress reduction when using rehabilitation options like CFRP and GFRP liners.

Overall, these analyses provide valuable insights into the mechanical behavior and rehabilitation of pipelines using CIPP technology under various conditions and loading scenarios.

### **1.7. Task 4 Monitoring of CIPP Liners with Fiber Optical Sensors**

Once the CIPP lining has been fully installed, the rehabilitated pipelines need to be certified or evaluated. There are various technologies can be used to evaluate, assess, and certify the CIPP liners. This section summarizes the current state-of-practice for the liner inspection and monitoring.

*(a) Visual Inspection:* Typically, visual inspection is conducted following ASTM F1743 or closed-circuit television (CCTV) cameras before and after CIPP lining installation. This helps ensure that

the quality of the CIPP-lined pipes meets the required standards. CCTV inspection uses recorded videos or images to identify defects, including those that are easily visible. However, it has limitations in assessing intermediate stages of deterioration or liner distortions.

*(b) Focused Electrode Leak Location (FELL) Inspection:* Developed by Electro Scan Inc., FELL inspection and low voltage conductivity (LVC) are used to test, certify, and accept CIPP lining projects. FELL technology can consistently detect defects missed by CCTV inspections, such as wrinkles, accelerant burns, resin issues, weak liners, and more. However, FELL is applied upon request and not for continuous condition assessments.

Temperature Monitoring During Curing: Monitoring the temperature during the curing process of CIPP liners is crucial. New technology allows for temperature readings along the entire length of the pipe during curing. Sensors are placed inside the pipe before inserting the liner. These sensors transmit exothermic condition data to a computer or smartphone, ensuring proper and complete curing. The data can also be uploaded to a web server for reporting. Fiber optic cure verification (FCV) is another method that continuously measures temperature along the CIPP liner's full length, reducing blind spots in temperature measurement. These technologies help reduce the risk of curing failure.

While temperature monitoring is essential during curing, other mechanical properties may also be important but are typically not measured during the curing and service periods. These evaluation and certification methods collectively ensure the quality and reliability of CIPP liners for pipeline rehabilitation.

It's important to highlight that many municipalities collect quality assurance (QA) samples or coupons for laboratory testing or potential warranty claims. However, these coupons may not accurately reflect the real conditions of the repaired pipes. Assessments conducted by the Environmental Protection Administration (EPA) revealed that 69% of sewer pipes rehabilitated with CIPP liners exhibited defects, with greater defect flow measurements observed after rehabilitation. There is a pressing need for more in-situ monitoring techniques to enhance the assessment of rehabilitated CIPP liners.

### **1.8. Task 5 Risk Analysis of Pipelines and Liners**

The data obtained from all the material testing, property assessments, and numerical analysis can be beneficial to the management of the CIPP liners and the corresponding rehabilitated pipelines through risk analysis. In this section, we reviewed the risk assessment methods in ASME pipeline standard, stochastic/probabilistic approaches, and machine learning-based approaches. We also reviewed different types of risk in the pipelines in terms of the pipe failure effect, construction & in-service risk, and environmental risk.

*(a) The ASME Pipeline Risk Assessment process involves seven steps for managing pipeline integrity:*

- 1) Identify Potential Threats: ASME classifies 22 pipeline integrity threats, one category is "unknown." The others are divided into 9 categories, including external corrosion, internal corrosion, stress corrosion cracking, manufacturing-related defects, welding/fabrication

related, equipment, third-party/mechanical damage, incorrect operational procedure, and weather-related and outside force

- 2) Gather, Review, and Integrate Data: Limited data sets are collected for each threat, using data from the operating company, external sources, and existing databases. Data sources are essential for program initiation.
- 3) Risk Assessment: Risk assessment includes prescriptive and performance-based programs, considering the likelihood and consequences of adverse events. Four risk assessment methods are used: Subject Matter Experts (SMEs), Relative Assessment Models, Scenario-Based Models, and Probabilistic Models.
  - a. Prescriptive Integrity Management Programs: Reinspection intervals are determined based on a table that considers the maximum allowable operating pressure (MAOP) for pipeline segments.
  - b. Performance-Based Integrity Management Programs: Initial integrity assessments prioritize methods such as those mentioned above, considering attributes, resources, history, and more.
- 4) Integrity Assessment: An appropriate integrity assessment method is identified for each pipeline system or segment, including In-line inspection (ILI), Pressure testing, Direct Assessment, or other recognized methodologies.
- 5) Responses to Integrity Assessment, Mitigation (Repair and Prevention), and Setting Inspection Intervals: After the integrity assessment, it is required to take measures to mitigate the impact based on the response to the integrity assessment.
- 6) Update, Integrate, and Review Data: After doing initial integrity assessments, the updated information shall be retained and added to the database of information used to support future risk assessments and integrity assessments.
- 7) Reassess Risk: Periodic risk assessments are conducted at regular intervals and when significant changes occur in the pipeline.

This comprehensive process ensures the integrity and safety of pipelines by assessing and mitigating potential risks.

In the context of risk analysis for pipelines, various stochastic and probabilistic approaches have been explored, the reviewed approaches include:

*(b) Stochastic/Probabilistic:*

1. Artificial Neural Network-Based Models (ANN) and Fuzzy Inference System (FIS): These models were used to predict risk indices. FIS considered 8 main causes and 30 root causes, selecting their probabilities using Matlab fuzzy toolbox. ANN models were chosen based on performance metrics like MSE and  $R^2$ .

2. Fuzzy Bayesian Networks (FBN): FBN was applied for safety risk analysis in tunnel construction, predicting the probabilities of various factors.
3. Bayesian Network (BN): BN was used to assess pipeline safety due to third-party damage (TPD), considering factors like machinery hits, pipeline strength, and geological disasters. A failure model was developed using Monte Carlo simulation and FOSM method.
4. Reliability Assessment Model: Non-homogeneous Poisson process (NHPP) was used to evaluate the normal and defective states of oil pipelines, considering factors like corrosion and shock damages.
5. Oil & Gas Pipeline Internal Corrosion Risk Assessment: A Bayesian belief network combined various corrosion models to predict the probability of failure, with sensitivity analysis showing the importance of factors like operating pressure and defect depth.
6. Fuzzy Bayesian Network with Bow-Tie Model: This approach assessed gas pipeline risk, considering both external and internal factors, and used fuzzy probability to calculate failure probabilities.
7. Fuzzy Bayesian Belief Network Model: This model assessed the risk of oil and gas pipelines, highlighting factors such as construction defects, overload, mechanical damage, bad installation, and worker quality.

*(c) Machine Learning-based Approaches:*

1. K-Means and Gaussian Mixture Model (GMM): These models classified corrosivity levels for soil corrosivity assessment in external pipeline integrity management. A failure model combining regression analysis and artificial neural networks (ANNs) was developed to predict oil pipeline failure.
2. Fuzzy Inference System (FIS): FIS was used to establish a risk index model, considering various factors. Sensitivity analysis and Monte Carlo simulation were employed for model evaluation.
3. Data-Driven Model (DDM): DDM combined simulation and regression algorithms to predict water pipeline failure, considering factors like water pressure and flow velocity.
4. Multiple Neural Networks and Fuzzy Logic System: These were used to establish a pipeline assessment model, considering features such as pipeline length, angle, and area to detect cracks and service laterals.
5. Pipeline Leakage Model: A bow-tie model was used to relate pipeline leakage to possible accidents. Bayesian network modeling and fault tree analysis were applied to assess factors contributing to pipeline leakage.

*(d) Types of Risk:*

- Three types of risks were considered: pipe failure effects, construction risk, in-service risk,

and environmental risks.

- Pipe failure effects were evaluated based on factors like chemistry-related changes in pipeline properties, age, diameter, and operating conditions.
- Construction risk assessment included a risk index (R) to account for the risk of landslides during pipeline construction.
- Environmental risk factors during pipeline construction were also identified and assessed.

These approaches and risk assessments contribute to better understanding and management of pipeline integrity and safety.

### **1.9. Objectives in the 1<sup>st</sup> Annual Report Period**

In Year 1, according to the planned schedule, the major objectives as aligned in the proposal include:

- (1) Complete Task 1 Kick-off meeting with PHMSA personnel and literature review on related topics of the proposed research;
- (2) Complete 45% of Task 2 Development of healable and sustainable CIPP structural liner;
- (3) Complete 40% of Task 3 Enhancing mechanical and bonding performances and reducing permeability of the healable CIPP structural lining through nanofiller;
- (4) Complete 30% of Task 4 Enabling self-sensing for the developed CIPP structural liner;
- (5) Complete 20% of Task 5 Integration of the multifunction with the pipeline integrity management system;
- (6) Complete 34% of Task 6 Reporting and student mentoring.

The planned objectives are achieved as planned above. Task 1 was completed in the first quarter. On Nov. 22<sup>nd</sup>, 2022 (1:30 -3:00 pm CT), a zoom kick-off meeting was conducted between the PHMSA program managers, the advisory board member, and the research team. All PIs attended the kick-off meeting. A web presentation was made to the PHMSA personnel followed by questions/answers and discussions. The literature review was presented in the background above. The results and findings in addition to experimental designs of Tasks 2 to 5 are detailed below.

## **2. Experimental Program in the 1<sup>st</sup> Annual Report Period**

### **2.1. Experimental Design**

The experimental study for this project, illustrated in Figure 1, consists of four primary tasks: a) designing, developing, and assessing the all-in-one liner's performance, b) performing finite element numerical analysis to model and forecast the liner's performance, c) carrying out

permeability simulations and interfacial bonding chemical analysis to explore the molecular-level mechanics in nanocomposite, and d) employing an AI-driven risk analysis and integrity management system. As this section centers on the experimental study (part a), additional information is offered in Figure 1.

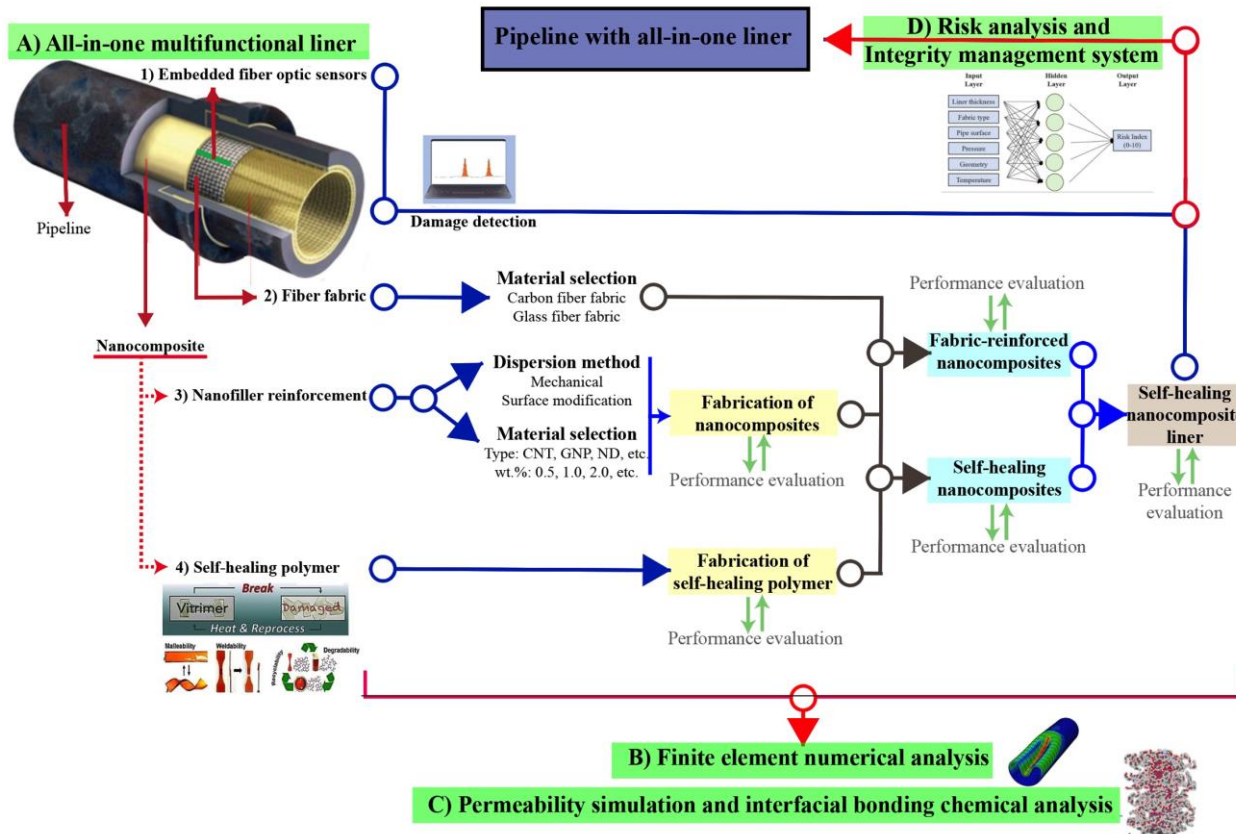


Figure 1. General strategy of the experimental study

The proposed all-in-one liner is composed of four elements: 1) integrated fiber optic sensors for damage detection, 2) fiber fabric reinforcement to boost mechanical properties, 3) incorporation of nanoparticles to enhance the overall performance of the nanocomposite liner, and 4) self-healing polymers for self-repair any damages or cracks that might develop in the liner.

The research study at this reporting period focused on exploring nanofiller reinforcement and developing self-healing polymers. Consequently, the nanofiller reinforcement investigation is being carried out by incorporating nanoparticles a commonly used commercial polymer, EPON 828. This part includes optimizing dispersion methods and nanomaterial selection; currently, CNT, GNP, and ND with 0.5, 1.0, 2.0 wt.% are chosen for experimental investigation. The developed nanofiller-reinforced nanocomposite will be subject to performance evaluation, and the nanocomposite design or dispersion techniques may be adjusted based on the results.

After the nanocomposite has been developed, it will be combined with self-healing polymers or fiber fabric to create self-healing nanocomposites and fabric-reinforced nanocomposites, respectively. The performance of both nanocomposites will be evaluated, and the nanocomposites'

designs may be modified based on the results. Subsequently, the self-healing nanocomposites and fabric-reinforced nanocomposites will be merged to fabricate self-healing nanocomposite liners, with the final design determined by adjustments based on results from performance evaluation.

Once the nanofiller-reinforced nanocomposites are successfully developed, they will be integrated with either self-healing polymers or fiber fabric to develop self-healing nanocomposites and fabric-reinforced nanocomposites, respectively. The performance of both types of nanocomposites will be assessed, and adjustments to their designs may be made in response to their performance. Subsequently, the self-healing and fabric-reinforced nanocomposites will be combined to create self-healing nanocomposite liners, with the final design established through adjustments based on performance evaluation outcomes.

Upon successful development of the nanofiller-reinforced nanocomposites, they will be combined with self-healing polymers or fiber fabric to produce self-healing nanocomposites and fabric-reinforced nanocomposites, respectively. The performance of both types of nanocomposites will be evaluated, and design may be modified based on their performance. Following this, the self-healing and fabric-reinforced nanocomposites will be merged to develop self-healing nanocomposite liners, with the final design determined through adjustments that are dependent by performance evaluation results.

Finally, upon the successful development of the self-healing nanocomposite liner, exhibiting exceptional mechanical, chemical, and self-healing properties, fiber optic sensors will be integrated to furnish the liner with damage detection capabilities. This step completes the fabrication process of the all-in-one liner, the physical product of this project. It should be noted that finite element numerical analysis (part b), permeability simulation (part c), and interfacial bonding chemical analysis (part c) will work closely with the experimental study to offer direction via numerical analysis and simulations. In conclusion, the entire system will undergo optimization through risk analysis and the establishment of an integrity management system (part d).

## **2.2. Test Procedure**

- Laboratory Testing:

### **2.2.1. Task 2 Development of healable and sustainable CIPP structural liner**

For the thermally-Curable Vitrimer Resin, the dynamic transesterification (DTER) mechanism is a common method used to give thermosets the ability to self-heal and to be recycled, as well as other vitrimer properties. In this work, this is accomplished by incorporating ester bonds and hydroxyl groups into the polymer through the reaction between an epoxy and an anhydride or a carboxylic acid.

Curing epoxy resins with anhydrides requires additives to induce the ring-opening of the anhydride to form a carboxylic acid. The carboxylic acid can then react with the epoxide groups at elevated temperatures, crosslinking the epoxy resin and producing a secondary hydroxyl group. The hydroxyl group produced can then induce the ring-opening of the anhydride which causes further crosslinking of the epoxy resin. Typically, organic salts or strong bases are used as catalysts to induce the ring opening which may bring toxicity or cause corrosion of the substrate material.

Alternatively, primary hydroxyl groups can induce ring-opening, similar to how the secondary hydroxyl group functions in causing further crosslinking but occurring at relatively lower temperatures. Glycerol is a good fit for this role because it possesses two primary and one secondary hydroxyl groups.

To synthesize the thermally-curable vitrimer resin, epoxy resin, anhydride, and glycerol were added to a container and mixed at room temperature for 10 minutes. Then, the temperature was increased to 130°C and mixed for 1 hour. After mixing at 130°C the sample became clear as the glycerol reacted with the anhydride making it miscible in the epoxy resin (Figure 2). Then, the mixtures were placed in a vacuum oven at 110 °C to remove the trapped gas. The resultant mixture is either coated on a metal plates plate (precleaned with acetone) using a film applicator (6 mils) to control the coating thickness or poured into a dumbbell or rectangular shape silicon mold. The resin was then cured at 190°C for 2hr in a convection oven. After curing, the sample was cooled naturally to room temperature.

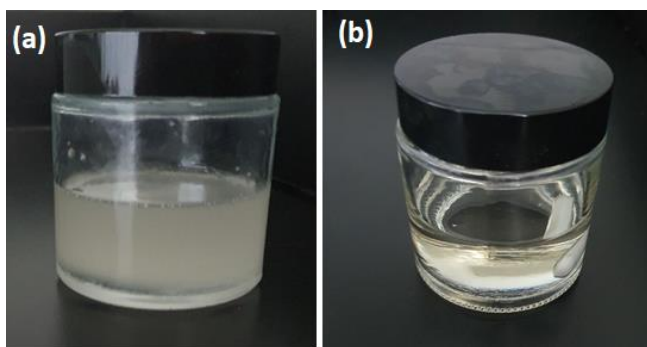


Figure 2. Photos of the resin system (a) before and (b) after heating at 130 °C for 1 h. The white solid in the glass bottle is a magnetic stirrer.

## 2.2.2. Task 3.1 and 3.2 Nanocomposite characterization and Performance evaluation

### 2.2.2.1. Materials for nanocomposite development

Commercially commonly used epoxy was employed to study the nano-reinforcement; an undiluted clear difunctional bisphenol A/epichlorohydrin derived liquid epoxy resin, Epon 828, was used to crosslink with a modified polyamide curing agent, Epikure 3175, to formulate high solid ambient cure polymer composite, which offers great overall performance. To explore the impacts of the morphology of different nanoparticles on the performance of nanofiller-reinforced nanocomposites. Additionally, three types of carbon-based nanoparticles were selected due to 1) they have been proven to have a promising improvement in the performance of nanocomposite, 2) all of them are carbon-based materials, so the chemical interaction between nanofiller and polymer can be eliminated during the comparative study, and the effect of nanoparticle's shape can be focused. Therefore, this study aimed to provide a comprehensive, comparative investigation to systematically assess the impacts of nanoparticles on the tribological, mechanical, and wettability of the epoxy coatings using three representative 0D, 1D, and 2D nanoparticles: nanodiamond (ND), graphene nanoplatelets (GNPs), and carbon nanotubes (CNTs). The nanomaterials were purchased from Skyspring Nanomaterials Inc. and their properties are summarized in Table 4.

Table 4 The properties of the selected nanoparticles

Nanodiamond (ND)	Multi-walled carbon nanotube (MWNT)	Graphene Nanoplatelets (GNP)
Purity: > 95% Appearance: Grey Morphology: spherical Diameter: 3-4 nm Surface Area: ~282 m <sup>2</sup> /g True density: 3.05-3.30 g/cm <sup>3</sup>	Purity: > 95% Appearance: Black powder Morphology: fibrous Outside diameter: 50-100 nm Inside diameter: 5-10 nm Length: 5-20 μm Surface Area: >60 m <sup>2</sup> /g True density: ~2.1 g/cm <sup>3</sup>	Purity: 99.5% Appearance: Black powder Morphology: platelets Thickness: 6-8 nm Average Diameter: 15 micron Surface Area: 120-150 m <sup>2</sup> /g

2.2.2.2. *Fabrication process of nanocomposite*

Mechanical dispersion techniques were used in this study, such as ultrasonication, high shear dispersion, and stirring, were intensively used. Without any additional chemicals, such as solvent and surface modification agent, the performance of fabricated nanocomposite was solely dependent on the morphology of nanoparticles. Identical dispersion/fabrication procedures were employed for all the selected nanoparticles (CNT, GNP, and ND), and the nanoparticles were added to epoxy resin, and pre-dispersed with 1-min hand-stirring by a spatula in a fume hood. Afterward, the mixture was subjected to a combination of high-shear dispersing and high-power ultrasonication methods. Firstly, a 30-minute high-shear disperser was employed to break down large particles in the mixture, with a controlled speed of 4000 rpm. Secondly, the slurry was transferred to a probe ultrasonic system for further dispersion. The 100% amplitude was applied, and a 15-second "on/off" cycle was used during the ultrasonication for an overall duration of 30 mins. For both high-shear dispersing and high-power ultrasonication, a water bath was used to avoid overheating, and the water was subjected to renewal every ten minutes.

After the dispersion procedure, the curing agent was added to the mixture, and the molar ratio to the epoxy resin was 1:1, which was mixed by mechanical stirring at 600 rpm for 10 minutes. For all the nanoparticles, three varied concentrations were used, which are 0.5, 1.0, and 2.0 percent by weight. The prepared samples were stored at room temperature for at least seven days before any experiments were conducted., as presented in Figure 3.



Figure 3. Examples of prepared nanocomposite samples

### 2.2.2.3. Characterization and performance evaluation techniques for developed nanocomposites

(a) *Particle size distribution by dynamic light scattering (DLS):* Achieving proper dispersion of nanoparticles is a critical aspect of their reinforcement in nanocomposites. The size of the nanoparticles can significantly affect their reinforcing ability, as larger agglomerates may lead to more significant defects and large microcracks. To evaluate the dispersibility of each nanofiller, we used dynamic light scattering (DLS) with a submicron particle sizing instrument (Nicomp 380) to study their particles size distributions. As identical dispersion procedure was applied to all nanofillers, the impact of nanoparticle shapes on their tendency to form agglomerates can be evaluated.

(b) *SEM & TEM imaging techniques:* A high-resolution analytical TEM device, the JEM-2100, was employed to investigate the morphologies and microstructures of nanofillers. In order to obtain clear images, the nanofillers were dispersed into ethanol at an appropriate weight ratio prior to TEM observation. To analyze the fracture toughness and wear resistance of the composites, a JSM-7600F Schottky field-emission scanning electron microscope (FE-SEM) was employed to record surface micrographs. Specifically, SEM images of the fracture and abraded surface were examined in this study.

(c) *Viscosity of nanofiller-epoxy mixtures:* After the nanofillers were properly dispersed into the resin, a viscosity test was carried out with a Brookfield DV-II viscometer to evaluate the impact of nanofillers on the polymeric matrix's rheological properties. The test was conducted at room temperature (23°C), using a #7 spindle at a rotation rate of 50 rpm. Results were only valid if the torque percentage fell between 10 and 90 percent; if not, the spindle or rotational speed required adjustment. Each sample underwent a minimum of three measurements, with the final result being the average of all values.

(d) *Coupon tensile test:* To determine the tensile properties of a polymeric nanocomposite reinforced with the nanofillers, coupon tensile tests were conducted according to ASTM D638. The tests were carried out using Shimadzu's EZ-X tester (Figure 4) with a loading rate of 1.0 mm/min, and the applied load and corresponding strain were recorded. From this data, the tensile strength ( $f = \frac{P}{A_0}$ ) and ultimate strain ( $\epsilon = \frac{L_0 - L}{L_0}$ ) were calculated, where P is the applied load,  $A_0$  is the original cross-sectional area, and  $L_0$  is the original length.



(a)



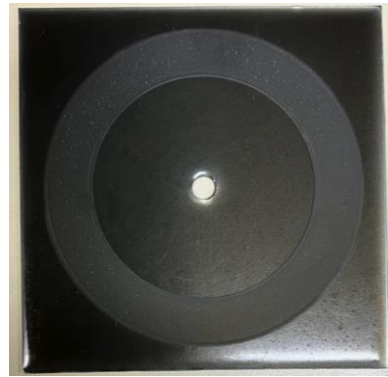
(b)

Figure 4. (a) Shimadzu's EZ-X tester, and (b) dog-bone sample

(e) *Abrasion resistance test:* To assess the wear resistance of the coating, the Taber abrasive method was used following ASTM D4060 (Figure 5). The surface of each specimen was rotated under two abrasive wheels at a speed of 72 revolutions per minute, while a load of 1000 g on each wheel was applied during the test. The abrasion resistance of the coatings was determined by measuring the mass loss, which is given by  $Mass\ loss = M_{intact\ coating} - M_{damaged\ coating}$ , where  $M_{intact\ coating}$  is the initial weight of the sample, and  $M_{damaged\ coating}$  is the remaining weight after abrasive cycles. A lower mass loss indicates stronger abrasion resistance in the nanocomposite, which can protect composite and substrates from damage caused by abrasion motions.



(a)



(b)

Figure 5. (a) Taber Abraser, and (b) nanocomposite after abrasion test

(f) *Adhesion test:* To evaluate the adhesive bonds between the nano-reinforced nanocomposite and the substrate, the pull-off bonding strength to the metal substrate was examined using a tension button test. Dollies with a diameter of 14 mm were glued to the top surface of the coated sample, and the adhesion strength was recorded during the test (Figure 6). The pull-off adhesive strength ( $\sigma_a = \frac{P}{A_0}$ ) was determined when the dolly was detached by applied load, where P is the applied tensile load, and  $A_0$  is the tested area.



Figure 6. Prepared sample with glued dollies

(g) *Water contact angle test*: The contact angle test was used to determine the wetting behavior of the nanocomposite surface in accordance with ASTM D7334. A camera was used to capture the image, while the angle  $\theta$  between the water droplet and the coated substrate was calculated by a computer from the image (Figure 7). The coating surface was categorized based on angle value as hydrophilic ( $\theta < 45^\circ$ ), hydrophobic ( $\theta > 90^\circ$ ), and in-between ( $45^\circ \leq \theta \leq 90^\circ$ ) when water was used as the test liquid.

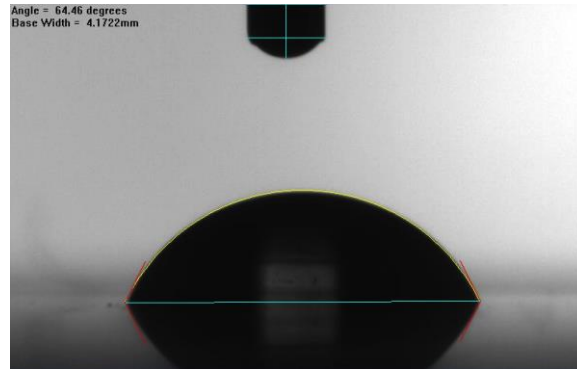


Figure 7. Image captured during water contact angle test

(h) *Single lap shear test*: Single Lap Joint (SLJ) adhesion tests for the CMC treated CNT and pristine CNTs modified healable epoxy resin on the cast-iron substrate: The SLJ test specimens will be designed based on ASTM D3165-0767 (Figure 9a). Two cast-iron plates are bonded by the modified healable epoxy at the bonding area, and two jaws are also bonded at each end of the adherents. The thickness of the adhesives is regulated at 0.2 inches for the specimens. SLJ tests will be performed using MTS Flex Test® SE loading frame (Figure 8). Monotonic tensile loading will be applied on the modified healable epoxy resin under displacement control mode at a constant rate until a shear fracture occurs.

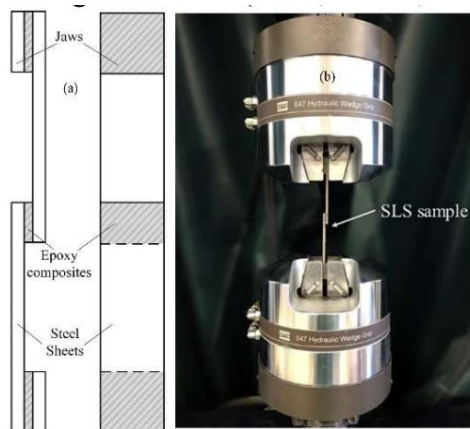


Figure 8. Single Lap Joint (SLJ) adhesion tests

(i) *Flexural properties test*: Flexural Strength, System Flexibility, Curvature, and Bend Analysis: the flexural strength of the produced samples was evaluated by using the MST loading machine (Figure 9), in accordance with ASTM D 790 standards and the prepared samples have dimensions of 100\*13\*3 mm.



Figure 9. Three-point bending flexural property tests

### 2.2.3. Task 3.3 Finite element numerical analysis (FEA)

#### 2.2.3.1. Three-dimensional finite element model description

We created a 3D finite element model in ABAQUS software [12] to simulate a cast-iron pipe rehabilitated by the CIPP liner buried in a subgrade structure. Two loading conditions on the FEA model are considered: 1) external subgrade load; 2) internal in-pipe pressure.

(a) *Model setup with subgrade loading condition:* Three buried depths (1, 2, and 3 m) of pipeline under the subgrade and seven liner thicknesses (from 0 to 8 mm) are analyzed in the parametric study. Figure 11 shows the schematic of the finite element model for the soil subgrade (brown) – cast-iron pipeline (silver) – epoxy resin liner (blue) system. The model component dimensions are listed in Table 5. Based on the references on three-dimension analysis for pipe elements [13], we apply eight-node linear brick solid elements (C3D8R) with reduced integration and hourglass control to model the subgrade, and four-node doubly curved thin shell elements (S4R) with reduced integration and hourglass control to model the pipe and liner. An isotropic, Mohr-Coulomb model is applied to simulate the external subgrade load on the pipeline. Linear elastic constitutive models are applied for the cast-iron pipeline and the epoxy resin liner since the pipeline and liner materials are much stiffer than the surrounding subgrade.

Table 5. Model component dimensions.

Component	Parameters	Value
Subgrade	Length (m)	4.0
Cast-iron pipeline	Length (m)	4.0
	Outside diameter (mm)	400.0
	Thickness (mm)	5.0
Epoxy resin liner	Length (m)	4.0
	Outside diameter (mm)	390.0
	Thickness (mm)	Varied

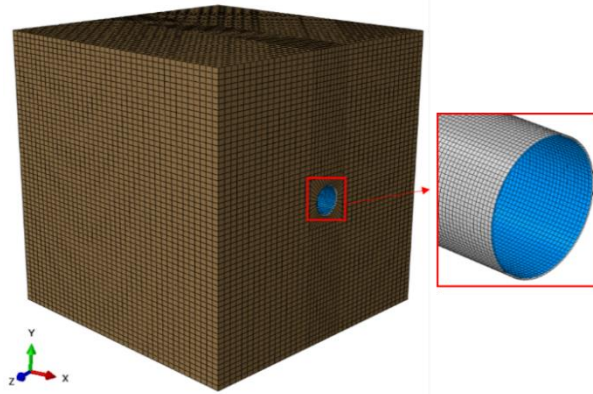


Figure 11. The 3D finite element model with meshes for the subgrade – pipeline – liner system (Brown: subgrade; Silver: cast-iron pipe; Blue: epoxy resin liner).

The material properties used in this finite element analysis (FEA) are listed in Table 6. For boundary conditions, the bottom displacement of the subgrade is fixed, the surrounding displacement is constrained in normal direction, and axial displacement of the pipe-liner is restrained. In this study, we assume an ideal operational environment, where the liner is perfectly bonded to the pipe's inner surface. A tie constraint is adopted to simulate the bonding condition between the pipe and the liner without any relative displacement. The interfacial interaction of the subgrade-pipe is defined as hard contact with no separation in the normal direction, and penalty contact in the tangential direction with friction coefficient 0.7. The gravitational acceleration  $9.81\text{m/s}^2$  is applied to model the gravity of the subgrade in a Static, General step in Abaqus.

Table 6 Material properties.

Component	Parameters	Value
Subgrade	Elastic modulus (MPa)	30
	Poisson's ratio	0.35
	Density (kg/m <sup>3</sup> )	1800
	Cohesion (Pa)	8000
	Internal friction angle (deg)	30
	Dilation angle (deg)	0.1
Cast-iron pipe	Elastic modulus (GPa)	148
	Poisson's ratio	0.287
	Density (kg/m <sup>3</sup> )	7200
Epoxy resin liner	Elastic modulus (MPa)	8000
	Poisson's ratio	0.3
	Density (kg/m <sup>3</sup> )	1200

(b) *Model setup with internal in-pipe pressure condition:* In addition to the subgrade loading condition, we also consider the internal in-pipe pressure from the natural gas in the finite element model. According to the literatures [1,14,15], the internal in-pipe pressure is the dominant loading factor compared to the subgrade load in the natural gas pipelines. Three internal in-pipe pressures (1, 1.5, and 2 MPa) and eight liner thicknesses (from 0 to 8 mm) are analyzed in the parametric study. The model component dimensions and material properties are similar as the information in previous section. The only differences are 1) the loading condition is the internal in-pipe pressure

only; 2) longitudinal movement are fixed at both ends of the pipe and liner, while radial movement is allowed to avoid stress concentration at the ends [13].

(c) *Model setup for damaged pipe rehabilitated by CFRP liner:* We create a three-dimensional finite element model in ABAQUS CAE. To ensure the accuracy and convergence of the finite element model, critical consideration is given to the selection of element types, boundary conditions, and mesh qualities by researchers [16]. In this study, 4-node shell (S4R) elements are chosen for the pipeline and liner, as their thicknesses are significantly smaller compared to other dimensions. The ends of the pipe-liner system are constrained by hinges to simulate a finite length pipe. A finer mesh is generated around the corrosion hole to achieve a higher accuracy. The CFRP liner is a composite material with multiple layers. To simplify the simulation, we model it as a homogeneous isotropic one-layer structure. Additionally, we assume an excellent bonding condition between the pipe and liner by setting the “tie” constraint in the FEA model. The inner surface of the pipe is defined as the primary surface, and the outer surface of the liner is defined as the secondary surface. External interference is simulated by considering in-pipe pressure only. We neglect external loads from surrounding soil in this study, as a recent study discovered that compared to the in-pipe pressure, buried depth has negligible influence on pipe’s mechanical responses [14]. Figure 12 presents the geometry and mesh of the model. The thickness of the cast-iron pipe is simulated as 5 mm, and a range of thicknesses (0.5 – 8 mm) of CFRP liner are studied to investigate the rehabilitation effect. To account for localized perforation caused by corrosion over time [17], a circular hole is applied at the top middle of the pipe in the model. The mesh size of the model is set at a uniform size of 12.5 mm, except for a finer mesh around the corrosion hole to capture more precise mechanical performance. The inner surface of the pipe is subjected to uniformly distributed pressure conditions of 1, 1.5, and 2 MPa via “Static, General” step in the simulation. Since CFRP is a brittle material, which fails upon yielding, we apply a liner elastic constitutive model for the liner material property. The cast-iron is considered as elasto-plastic in the simulation, with detailed parameters listed in Table 7.

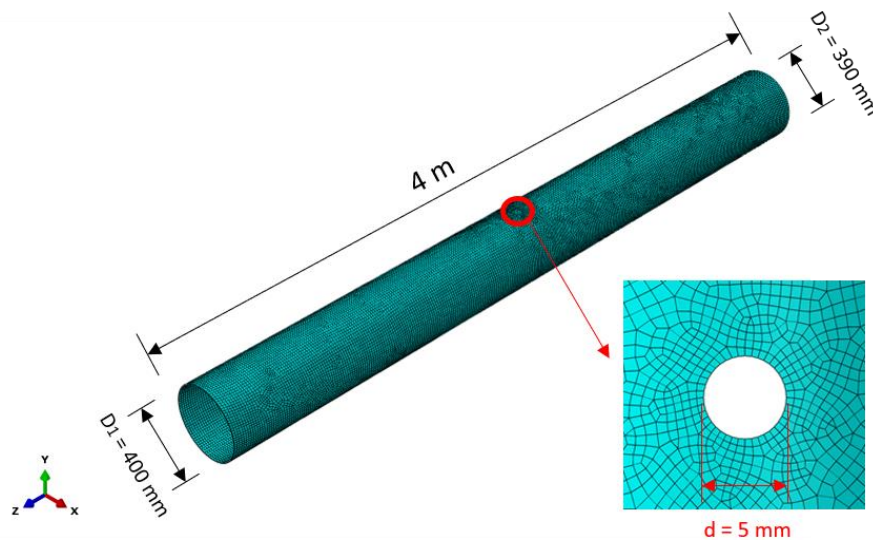


Figure 12. Geometry and mesh of the pipe-liner system. ( $D_1$  – outer diameter of the cast-iron pipe;  $D_2$  – outer diameter of the CFRP liner;  $d$  – diameter of the corrosion hole).

Table 7 Material properties in the FEA.

Parameter	Cast-iron Pipe	CFRP Liner
Elastic modulus (GPa)	148	200
Poisson's ratio	0.287	0.3
Density (kg/m <sup>3</sup> )	7230	1750
Yield stress (MPa)	428	2000
Ultimate stress (MPa)	497	2000
Plastic strain (%)	0.5	N/A

### 2.2.3.2 Model setup for neat epoxy sample under flexural testing

(a) *Initial Conversion of Experimental Data:* The material properties for neat epoxy in the finite element analysis is based on the flexural testing results of the neat epoxy samples at NDSU. Given that the flexural testing results are presented in the form of an engineering stress-strain curve, we convert it into true stress-strain data via simple determination method to describe the material properties [18]. Figure 13 shows the conversion results with a more accurate representation of the material behavior under flexural loads. The truss stress-strain curve is used as the material properties of the neat epoxy for the finite element models.

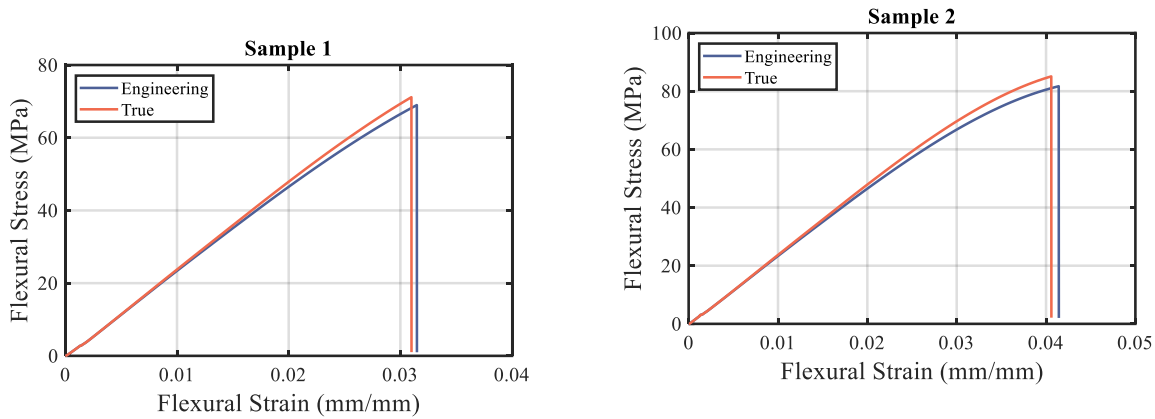


Figure 13. Engineering and true stress-strain behaviors in bending for epoxy samples.

(b) *FEA Model Setup:* We create three-dimensional (3D) FEA model in Abaqus to simulate the three-point bending test performed in the laboratory. The samples are made of neat epoxy with the dimension of  $100 \times 13 \times 3.9$  mm. The test setup consists of a mobile crosshead and two supports. The top crosshead with 5-mm radius locates at the midpoint of the specimen, and the two bottom supports with 5-mm radius are symmetrically placed with a 60 mm distance. 3D 8-node linear solid elements (C3D8R) are implemented for the mesh. The crosshead and supports are modeled as rigid bodies. The neat epoxy sample is brittle, which exhibits a linear constitutive relationship till it reaches the ultimate limit. Beyond the ultimate limit, the sample fails, indicating an absence of plastic deformation. Therefore, the epoxy sample is assigned an elastic material property. The flexural modulus and Poisson's ratio are from experimental results, and the ultimate stress is defined as yield stress with zero plastic strain. For the boundary conditions, the two bottom supports are fixed in all directions, and the top crosshead is constrained vertically only to apply the external load. A general contact interaction between three-point bending test setup and sample

is governed by the penalty method for tangential direction, employing a Coulomb friction coefficient of 0.2. In accordance with the experimental results, the samples failed at displacements of 5.5 mm and 7 mm in negative Y direction respectively. Therefore, an identical displacement control is applied on the reference point, situated at the center of the crosshead. We also implement finer mesh refinements in the central area of the sample. The FEA neat epoxy sample model with mesh is shown in Figure 14.

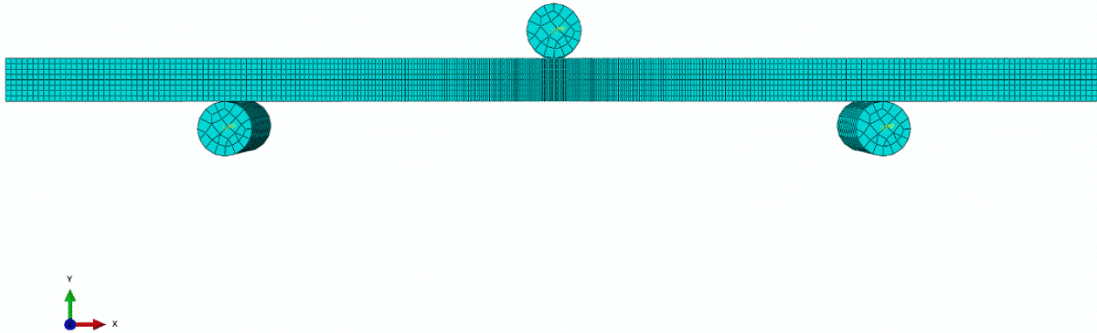


Figure 14. FE model with mesh.

#### 2.2.4. Task 3.4 Reducing the permeability and investigating the interfacial bonding chemical analysis

##### 2.2.4.1. Hydrogen models based on their density and self-diffusion properties

The focus of this part was on evaluating hydrogen models based on their density and self-diffusion properties and designing a calculation method for hydrogen permeability in self-healable epoxy resin. The choice of an appropriate hydrogen model is critical in accurately capturing the behavior of hydrogen molecules in molecular dynamics simulations of polymer materials. In our study, we investigated three commonly used hydrogen models: atomistic models, coarse-grained models, and reactive force fields. Atomistic models are characterized by the explicit representation of individual atoms, allowing for a detailed examination of hydrogen diffusion in polymers. Examples of force fields commonly employed for hydrogen in polymers include TraPPE, OPLS-AA, COMPASS, and CHARMM. Coarse-grained models offer a simplified representation of atoms, focusing on capturing essential system features. These models are advantageous when studying hydrogen permeability in larger polymer systems or over longer time scales. Parameters for coarse-grained models can be obtained through force matching or systematic coarse-graining approaches. Reactive force fields enable the explicit modeling of chemical reactions between hydrogen and polymer atoms, facilitating the study of hydrogen diffusion and permeation by capturing bond breaking and formation. ReaxFF and bond order potentials are examples of reactive force fields used to investigate the dynamic behavior of hydrogen atoms in polymer systems.

##### 2.2.4.2. Pore chemistry effect on the self-diffusion of hydrogen in pores

In this study, we evaluated rigid pore models and investigated pore chemistry effect on the self-diffusion of hydrogen in pores, and the utilized model is illustrated in Figure 10.

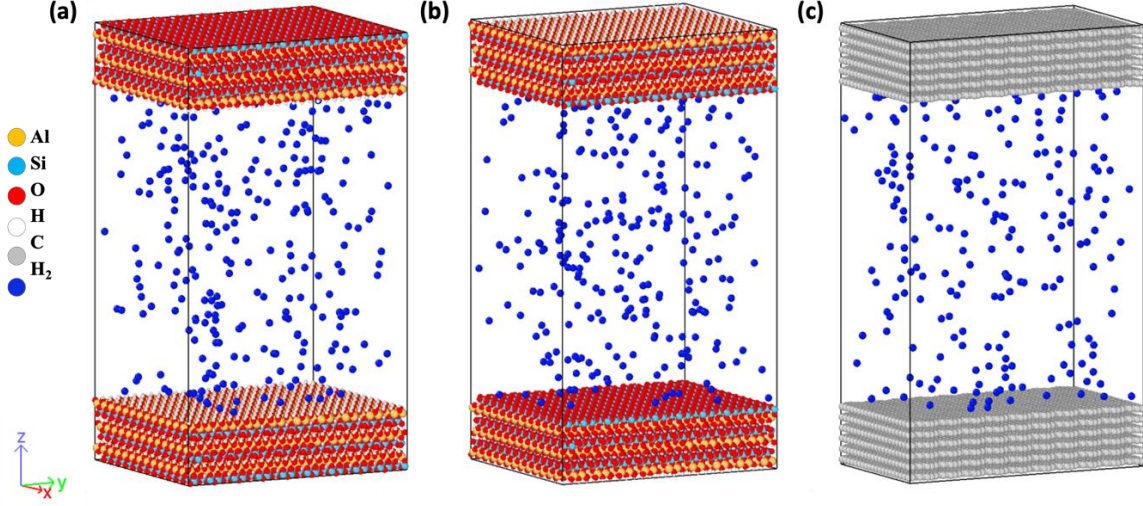


Figure 10. Hydrogen molecules confined in 3 types of nanopores. (a) Kaolinite pore with inward-facing  $\text{AlO}_4(\text{OH})_2$  surface. (b) Kaolinite pore with inward-facing  $\text{SiO}_4$  surface. (c) Graphene pore.

Self-diffusion coefficients for hydrogen are estimated from the mean-squared displacement of the molecules over time:

$$D = \frac{1}{2d} \lim_{t \rightarrow \infty} \frac{\langle [z(t) - z(0)]^2 \rangle}{t}$$

where  $d$  is the dimensionality of the particle displacement,  $t$  is the simulation time. For each system of  $N$  atoms, the normalized lateral velocity autocorrelation function is calculated as:

$$Z_{\parallel}(t) = \frac{\langle \sum_{i=1}^N \vec{v}_{xi}(t) \vec{v}_{xi}(0) \rangle + \langle \sum_{i=1}^N \vec{v}_{yi}(t) \vec{v}_{yi}(0) \rangle}{\langle \sum_{i=1}^N \vec{v}_{xi}(0) \vec{v}_{xi}(0) \rangle + \langle \sum_{i=1}^N \vec{v}_{yi}(0) \vec{v}_{yi}(0) \rangle}$$

where  $\vec{v}_i(t)$  is the velocity of a particle (index  $i$ ) at time  $t$ . Collisions of atoms with other atoms and with the solid pore surfaces results in an exponential decay of the velocity autocorrelation function (VACF), characterized by the following equation:

$$Z(t) = \exp(-t/\tau)$$

where  $\tau$  is the collision time, or the approximate time for the normalized VACF to decay from 1 to  $e^{-1}$ . The interaction energies between  $\text{H}_2$  and the pore surfaces are calculated as the standard 12/6 Lennard-Jones potential:

$$E = 4\epsilon \left[ \left( \frac{\sigma}{r} \right)^{12} - \left( \frac{\sigma}{r} \right)^6 \right] \quad r < r_c$$

where  $\epsilon$  is the dispersion energy,  $\sigma$  is the distance at which particle-particle potential energy is zero, and  $r_c$  is the cutoff radius (10 Å).

### 2.2.5. Task 4 Enabling self-sensing for the developed CIPP structural liner

To streamline the experimental design, the CIPP liner (Starline 200) was applied to a flat steel surface, accompanied by a 1mm thick layer of epoxy, as presented in Figure 15 (a) (b). In a bid to meticulously monitor the curing process and assess the load transfer between layers during mechanical deformation (Figure 15(c)), distributed fiber optic sensors were installed on both the steel and the inner surface of the liner (fabric surface).

These sensors, characterized by their compact size, boast a diameter of 125  $\mu\text{m}$  and a measurement gauge of 0.65mm. This design facilitates precise data capture while minimizing intrusion into the material structure, ensuring the integrity of the experimental conditions. The sensors' real-time monitoring capability is instrumental in providing insights into the dynamic interactions between the CIPP liner and steel substrate during various phases of mechanical stress and deformation (Figure 15(d)).

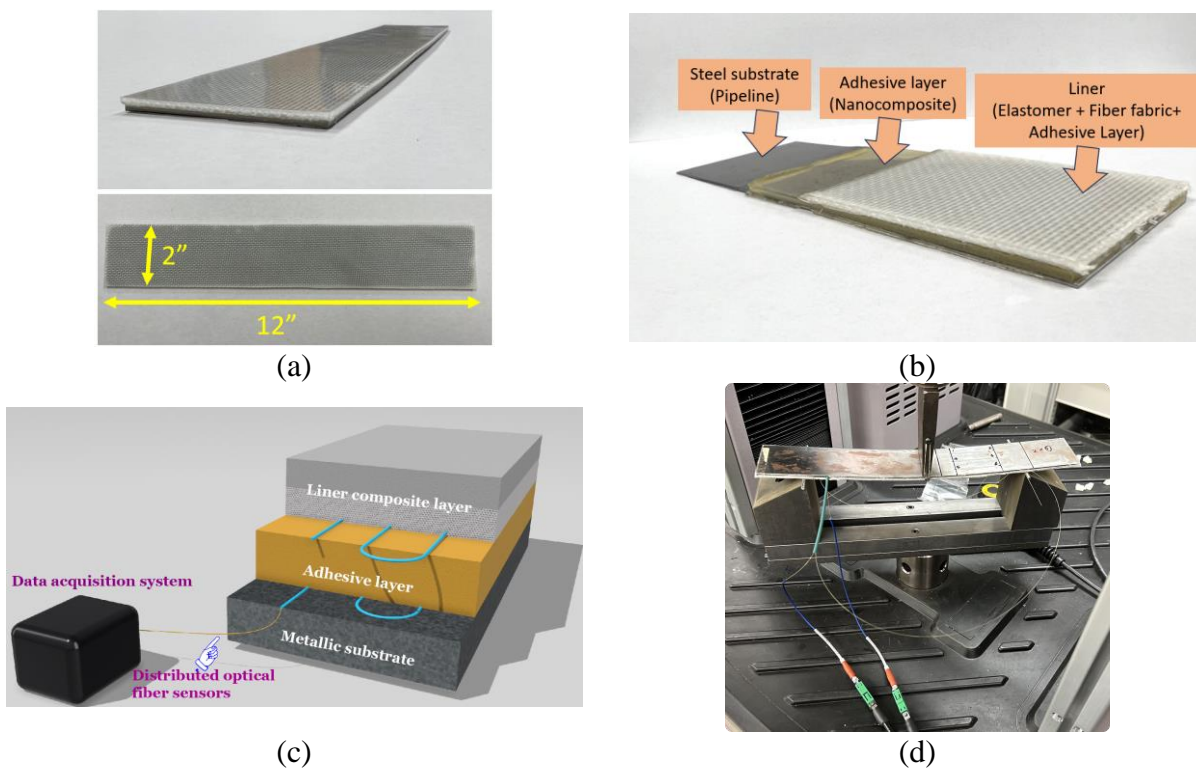


Figure 15. (a) (b) CIPP liner sample on flat steel substrate, (c) illustration of the CIPP sample with distributed fiber optic sensors, and (d) the CIPP liner under bending motion.

### 2.2.6. Task 5.1 Development of CIPP liner risk index for the pipeline integrity management enhanced by AI algorithms

The objective of this task is to efficiently predict the pipeline failure type through a machine

learning-based risk model. 50 years of spillage data in European cross-country oil pipelines is applied to train the model. In the methodology section, we predict the pipeline failure type through three machine learning-based risk models multivariable linear regression analysis (MVLRL). The collected 50 years of data and potential risk factors listed in CONCAWE report (2022) [19] is applied to train and test the models.

### 2.2.6.1. Data preparation

Pipeline failure is influenced by a range of factors, that can be defined as inputs in the risk model. According to the CONCAWE report (2022) [19] some of the most important factors include pipe diameter, service type, gross, net loss, leak detection, facility (pipeline location), facility part (such as bend, joint, and pipe run), age years, and land use. These data were collected from 779 data groups spanning from 1971 to 2020. Some of the various factors in the CONCAWE report (2022) contain categorical data, meaning they are qualitative rather than quantitative. The categorical factors include service, leak detection, facility, facility part, and land use. To analyze and train these categorical data with the machine learning algorithms, it is essential to define quantitative values for them. According to the CONCAWE report (2022), pipe diameter, gross, net loss, and age years are quantitative values with different units. It is necessary to normalize those values before training and testing the data. We normalize the data based on their range and each group is equally divided, as shown Table 8. The output includes five primary categories: mechanical, operational, corrosion, natural hazard, and third party.

Table 8 Variables' and factors' scale values.

	Factor	Details	Scale value
Input	Pipeline diameter ( $x_{PD}$ ) (inches)	$x_{PD} \leq 10$	1
		$10 < x_{PD} \leq 20$	2
		$20 < x_{PD} \leq 30$	3
		$30 < x_{PD} \leq 40$	4
		$40 < x_{PD} \leq 50$	5
	Gross ( $x_G$ ) ( $m^3$ )	$x_G \leq 1000$	1
		$1000 < x_G \leq 2000$	2
		$2000 < x_G \leq 3000$	3
		$3000 < x_G \leq 4000$	4
		$4000 < x_G \leq 5000$	5
	Net loss ( $x_{NL}$ ) ( $m^3$ )	$5000 < x_G \leq 6000$	6
		$x_{NL} \leq 800$	1
		$800 < x_{NL} \leq 1600$	2
		$1600 < x_{NL} \leq 2400$	3
		$2400 < x_{NL} \leq 3200$	4
	Age years ( $x_{AY}$ ) (years)	$3200 < x_{NL} \leq 4000$	5
		$x_{AY} \leq 10$	1
		$10 < x_{AY} \leq 20$	2
		$20 < x_{AY} \leq 30$	3
		$30 < x_{AY} \leq 40$	4
		$40 < x_{AY} \leq 50$	5

		$50 < x_{AY} \leq 60$	6
		$60 < x_{AY} \leq 70$	7
Output	Category (5) (Failure type)	Mechanical	1
		Operational	2
		Corrosion	3
		Natural hazards	4
		Third Party	5

### 2.2.6.2. Model groups

Correlation analysis is an important preliminary step in the risk assessment. It demonstrates the extent and direction of the correlation between two variables. The correlation map for ten different variables in the CONCAWE report (2022) is plotted in Figure 2. The map illustrates the relationship between these nine factors (input) and failure type (output). The correlation values between these nine factors and failure type are summarized in the last row or column in Figure 26. The factors are ranked according to the absolute value of the correlation coefficient from high to low as follows: “Facility”, “Leak detection”, “Age years”, “Pipe diameter”, “Land use”, “Facility part”, “Gross”, “Service”, and “Net loss”. According to Figure 26, the absolute value of the correlation coefficient for “Gross”, “Service”, and “Net loss” versus failure type is smaller than 0.1. We grouped the influencing factors into 9 types, as shown in Table 9.



Figure 26. Correlation map of pipeline variables.

Table 9 Model type details.

Model type	Variables
M1	$x_F$
M2	$x_F, x_{LD}$
M3	$x_F, x_{LD}, x_{AY}$
M4	$x_F, x_{LD}, x_{AY}, x_{PD}$
M5	$x_F, x_{LD}, x_{AY}, x_{PD}, x_{LU}$

M6	$x_F, x_{LD}, x_{AY}, x_{PD}, x_{LU}, x_{FP}$
M7	$x_F, x_{LD}, x_{AY}, x_{PD}, x_{LU}, x_{FP}, x_S$
M8	$x_F, x_{LD}, x_{AY}, x_{PD}, x_{LU}, x_{FP}, x_S, x_G$
M9	$x_F, x_{LD}, x_{AY}, x_{PD}, x_{LU}, x_{FP}, x_S, x_G, x_{NL}$

### 2.2.6.3. Multivariable Linear Regression (MVLRL)

Regression analysis is a popular statistical tool in data analysis. Multivariable linear regression analysis is a commonly used regression approach in risk assessment [20]. A mathematical equation is developed in the analysis to show the correlation between different variables and the target. In this report, as the pipeline failure type analysis involves more than two variables, the MVLRL approach is utilized for the risk model.

$$y_i = \beta_0 + \beta_1 x_1 + \beta_2 x_2 + \dots + \beta_i x_i + \epsilon_i \quad (1)$$

where  $\beta_i$  ( $i \geq 2$ ) is the regression parameter,  $x_i$  ( $i \geq 2$ ) is the predictor variable,  $\epsilon_i$  ( $i \geq 2$ ) is the random error, and  $y_i$  ( $i \geq 2$ ) is the response variable. In this report,  $x_i$  represents the influencing factors for pipeline failure type, and  $y_i$  represents the failure type.

There are three assumptions for the multivariable linear regression analysis chosen for this model: a) the dependent variable and predictor variables are in a linear relation; b) the residuals must be normally distributed; and c) the predictor variables are not highly correlated with each other [21,22].

- Field Testing: Not applicable in Yr 1.

## 3. Results and Discussions

### 3.1. Task 2: Development of healable and sustainable CIPP structural liner

#### 3.2.1. Task 2.1 Preparation of vitrimer epoxy resins, characterization, and optimization of the processing and curing conditions

##### 3.2.1.1. Vitrimer Properties of Thermally Cured Resin

To confirm the vitrimer properties of the starting epoxy anhydride system with glycerol performing the ring opening of the anhydride, self-healing and weldability tests were performed.

To test the self-healing of the coating, a razor blade was used to cut the coating down to the metal plate substrate. An optical microscope was then used to measure the width of the cut before and after the coating was repaired in a convection oven at 210 °C for 20 min. It can be seen from Figure 17 that the width of the scratch was significantly reduced by ~78% (from ~300 to ~65 μm).

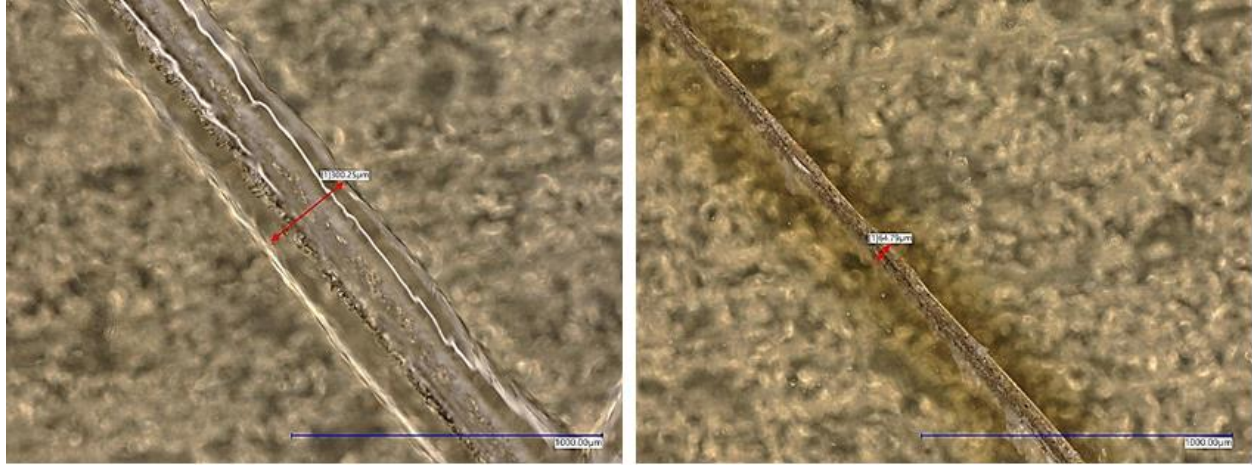


Figure 17. Photos of the coating before and after heating at 210 °C for 20 min.

To investigate the welding properties of the cured samples, the dumbbell shape sample was cut in half in the middle using a razor blade, then two halves were superimposed and held together under slight pressure for a welding time of 30 min at 210 °C (Figure 18). As can be seen in Figure 18 (c), the two halves were welded together after heat treatment.

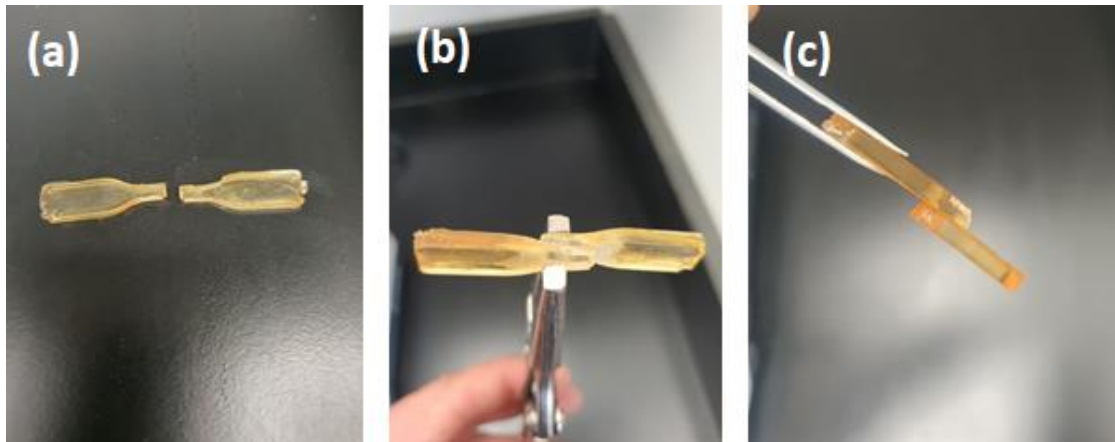


Figure 18. Photos showing the welding properties of vitrimer epoxy resin. (a) The cured specimen was cut in the middle using a razor blade, (b) cut halves were superimposed and held together under slight pressure for enough contact, and (c) welded sample after 30 min at 210 °C.

### 3.2.1.2. Adding Partial UV-Curability with Multifunctional Acrylates

The glycerol-catalyzed epoxy-anhydride vitrimer resin formulation was modified to be able to be UV-cured. This enables the resin to be partially cured using UV light, which could be used to create a flexible liner or prepreg woven fabric/fiber mat for pipe insertion. This was accomplished by adding a multifunctional acrylate and photoinitiator after mixing the epoxy resin, anhydride, and glycerol. Trimethylolpropane triacrylate (TMPTA) was added at 50 and 100 phr with 1 and 3 phr Omnirad TPO-L as the photoinitiator (PI), respectively. The formulations were then purged with nitrogen for 5 minutes at a flow rate of 10L/min, then cured for 10 minutes at a flow rate of 2.5L/min in a UV-curing enclosure to prevent oxygen inhibition (Figure 19). Once in place, the resin can be thermally cured to its long-term geometry.

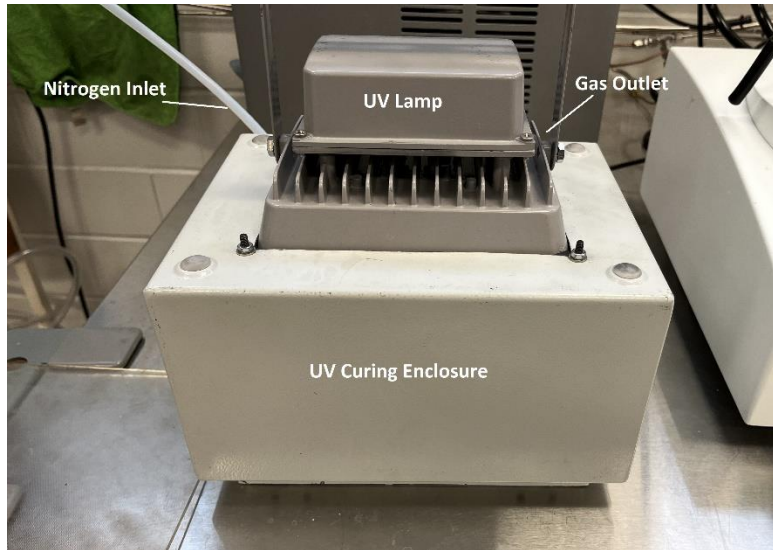


Figure 19. UV Curing Enclosure.

At 50 phr TMPTA and 1 phr PI, the resin remained liquid with a minor increase in viscosity after UV curing for 10 minutes. At 100 phr TMPTA and 3 phr PI, the resin solidified after UV curing for 5 minutes. Both formulations were able to be thermally cured after UV curing to produce stiffer specimens (Figure 20).

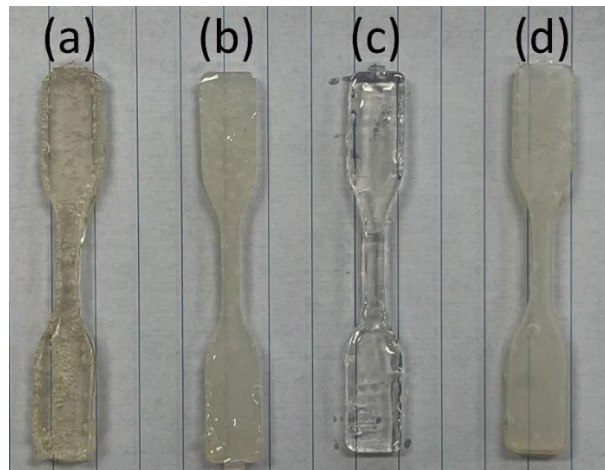


Figure 20. (a) Base epoxy-anhydride-glycerol formulation, (b) 50 phr TMPTA-1 phr PI after thermal curing, (c) 100 phr TMPTA-3 phr PI after UV curing, and (d) 100 phr TMPTA-3 phr PI after thermal curing.

The addition of TMPTA reduced the viscosity of the resin allowing it to be more workable near room temperature. This allows for easier addition/dispersion of filler/nanofiller material and easier resin impregnation of woven fabrics. This also allows for much easier degassing of the resin using centrifuge or vacuum methods. There are, however, downsides associated with this separate UV-curable acrylate system. One is the immiscibility of the epoxy-anhydride-glycerol system and the TMPTA that causes the resin to separate into two phases a couple days after mixing. The second is the acrylate interpenetrating polymeric network (IPN) does not contribute to the dynamic transesterification (DTER) reactions which impart the resin with vitrimer properties. Therefore,

TMPTA causes a decrease in the vitrimer properties of the resin. The 100phr TMPTA formulation was not able to be welded together.

### 3.2.1.3. Improving the Vitrimer Properties of the Partially UV-Curable Resin

Instead of a separate multifunctional acrylate system, a monofunctional acrylate with a primary hydroxyl functional group (2-hydroxyethyl acrylate), along with glycerol, was used to ring-open glutaric anhydride (GA) to create carboxy acrylate and dicarboxylic acid monomers (Figure 21). Once mixed with bisphenol a diglycidyl ether (BADGE) epoxy resin (DER-332), the resultant resin could then be UV cured and then thermally cured. Additional thermal curing can be used to increase the hardness of the samples further.

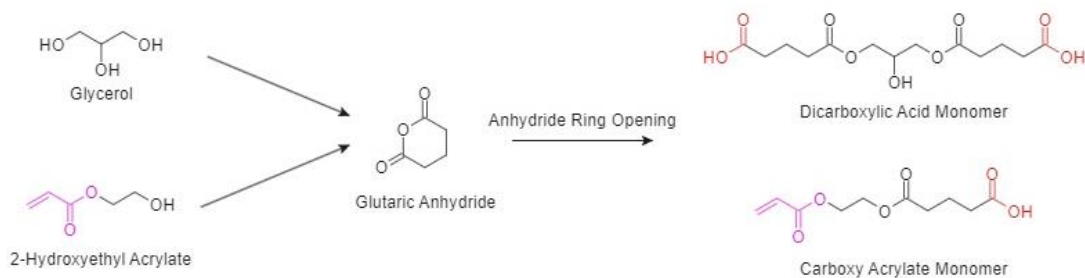


Figure 21. Ring-opening of glutaric anhydride using primary hydroxyl-containing monomers.

After just UV curing, the sample was too soft to be hardness tested and bent under its weight (Figure 22). After thermally curing for 1 hour, the resulting samples had a shore D hardness of 40 and dropped to 24 after 10 seconds (stress relaxation). UV curing before thermal curing prevents the evaporation of excess glycerol during thermal curing which would create large voids in the final cured product. After testing the welding capabilities at 210°C for 30 minutes, the sample had a hardness of 79 and stayed at 79 after 10 seconds. Unlike the previous TMPTA acrylate UV curable formulation, the sample displayed strong weldability and therefore retention of vitrimer properties (Figure 23).

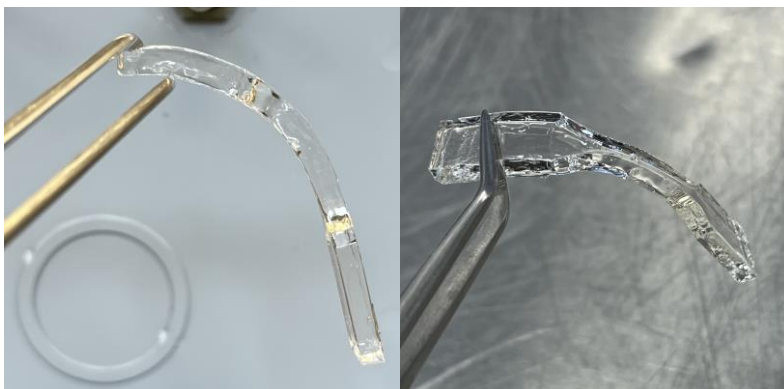


Figure 22. Flexible carboxy acrylate gel after UV curing.



Figure 23. Weldability of the partially UV curable formulation.

### 3.2.1.3. Fully UV-Curable Vitrimer Resins

Previously, glutaric anhydride (GA) was ring-opened using glycerol and a hydroxyl acrylate to introduce UV-curable acrylate groups into the resin. This was unsuccessful at synthesizing a fully UV-curable resin due to the high temperatures and times (190°C for >1 hr) needed to fully react the epoxy and resultant carboxylic acid from the anhydride ring-opening. For this reason, after UV-curing, the samples would need to undergo a thermal post-curing process.

Rather than having a hydroxyl acrylate ring-open the anhydride and the resultant carboxylic acid cure the epoxy, methacrylic acid (MAA) (with both a carboxylic acid and methacrylate functional group) was reacted with the epoxy directly forming a dimethacrylate using a commercial epoxy, bisphenol a diglycidyl ether (BADGE) (Figure 24). This is a simpler reaction scheme that forms a more crosslink-dense methacrylate resin that can be UV-cured.

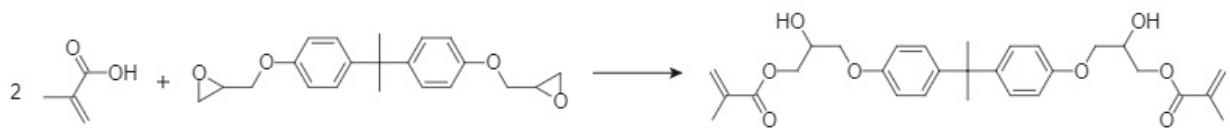


Figure 24. Scheme of MAA reacting with BADGE to form the dimethacrylate monomer.

### 3.2.1.4. Synthesis of UV-Curable Vitrimer Resin

BADGE and MAA were mixed in an equal epoxide to carboxylic acid functional group ratio. Photoinitiator (TPO-L) was added at a ratio of 1 molecule per 200 methacrylate groups. The mixture was then heated using a hot oil bath at 90°C and the resin was periodically tested by pipetting 1.5 g of material into a mold and then UV curing the resin. Two properties of the UV-cured polymer were investigated to get an estimate of the progress of the carboxylic acid and epoxide reaction, the strength and the transparency of the samples. If the reaction was incomplete the samples would be weak but also the unreacted BADGE would remain as a liquid dispersed in the sample making the sample opaquer. This formulation was checked after 0.5, 3.5, 5.0, 7.0, and

8.5 hours of heating and the samples got progressively stronger but even after 8.5 hours the sample was not completely transparent.

To speed up the synthesis of the dimethacrylate monomer and to catalyze the DTER mechanism, a reactive catalyst (Cat) was added. The catalyst was added at a loading of 1 molecule for every 100 epoxide/carboxylic acid groups (~1%). This formulation was heated at 90°C and tested at 10, 15, and 20 minutes. After 20 minutes of heating, the UV-cured samples were completely transparent and very strong (Figure 25). The resin also had a relatively low viscosity and did not experience premature methacrylate polymerization which can occur with too great of a catalyst loading. After this initial reaction, a reactive diluent can be added to reduce the viscosity and more catalyst can be added to help with the DTER mechanism.

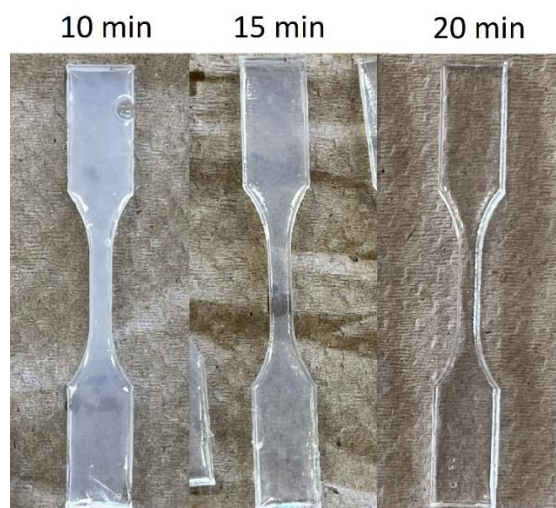


Figure 25. The increase in transparency and strength.

After determining a satisfactory formulation, the curing rate was determined by measuring the hardness of samples after increasing UV-curing times (Figure 26). After 4 minutes the formulation had cured the entire thickness and after 5 to 6 minutes the sample reached its maximum hardness.

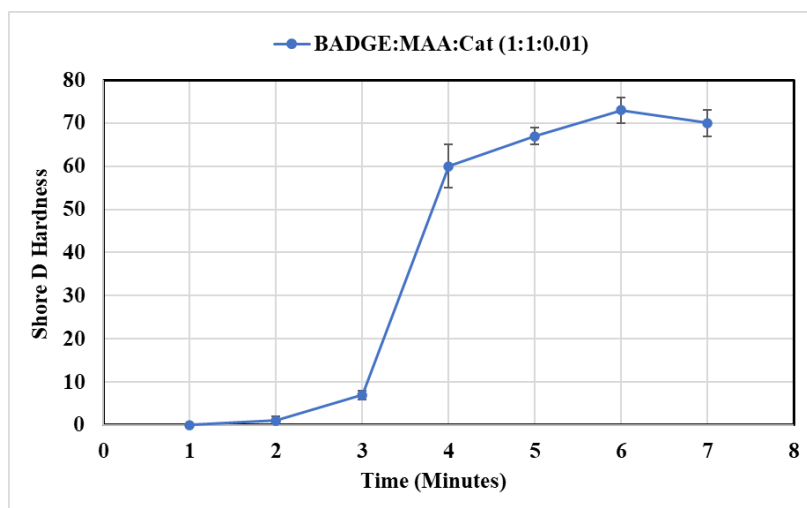


Figure 26. The Shore D hardness of the UV-curable resin after various curing times.

### 3.2.1.5. Improving UV-Curable Vitrimer Resin Workability

A catalyst is required to increase the rate of methacrylation of the bisphenol A epoxy resin (BADGE) and to lower the temperature of and improve the self-healing properties of the cured resin. The catalyst selected for this role is methacrylate functional which allows the catalyst to be covalently bonded to the polymer structure after curing. However, this functional catalyst (FC) has been spontaneously polymerizing with the resin shortly after being added leading to a viscous resin with significant polymer chain interactions making it difficult to work with.

Adding reactive diluent (RD) in a 0.5:1 to 1:1 functional group ratio allowed for the FC polymer to be dissolved resulting in a low viscosity resin. However, when adding additional FC to improve the self-healing properties the polymer came out of solution causing the resin to greatly increase in viscosity again. For this reason, the FC was replaced with a non-functional catalyst (NFC). Since this catalyst is non-functional, it does not covalently bond with the polymer and may act as a plasticizer in the resin once additional catalyst is added to improve the self-healing properties. If the NFC decreases the resin's properties too much, another option that can be tested is to incorporate an inhibitor to try and prevent the spontaneous polymerization of the FC.

## 3.2.2. Task 2.2 Investigating self-healing and mechanical properties of vitrimer epoxy resins

### 3.2.2.1. Self-Healing of UV-Curable Resin

The self-healing reaction of the UV-curable resin is activated at elevated temperatures and requires some pressure to mold two pieces together or fill cracks. Fractured tensile samples were adhered to each other at 150°C for 1 minute using a vice plier to apply pressure (Figure 27). Three formulations were tested: the base resin (0.01FC), the resin with 1:1 methacrylic reactive diluent (0.01FC 1MRD), and the resin with 1:1 methacrylic reactive diluent and 0.1:1 functional catalyst (0.1FC 1MRD). All three formulations adhered well and were unable to be separated at the point of adhesion and broke elsewhere when pulled apart. This signifies that a strong bond was formed during the self-healing process, but it is still necessary to obtain more quantitative results to compare formulations by mechanically testing, self-healing, and then retesting specimens.

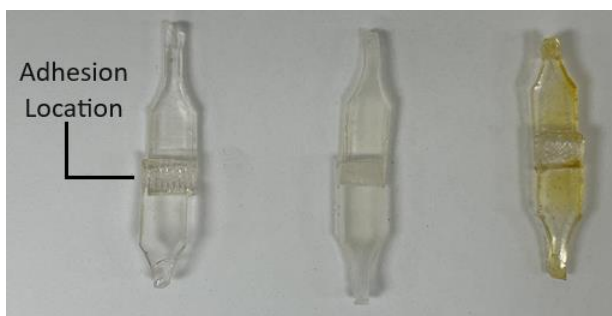


Figure 27. The adhesion of tensile specimens of 0.01FC (left), 0.01FC 1MRD (middle), and 0.1FC 1MRD (right).

Cracks were also cut into the surface of the 0.01FC 1RD formulation and then healed at 150°C for 5 minutes at 50psi in a hot press. Topographical images of the crack surface were taken before and after healing using an optical microscope to compare the change in the crack depth (Figure 28).

After healing, the crack depth was reduced from 450 to 120µm. When hot pressing the self-healing polymer, the polymer would spread out considerably. Confining the edges of the sample when self-healing to prevent this will allow the polymer to heal cracks more efficiently and mimic the field conditions of the self-healing of the liner more closely.

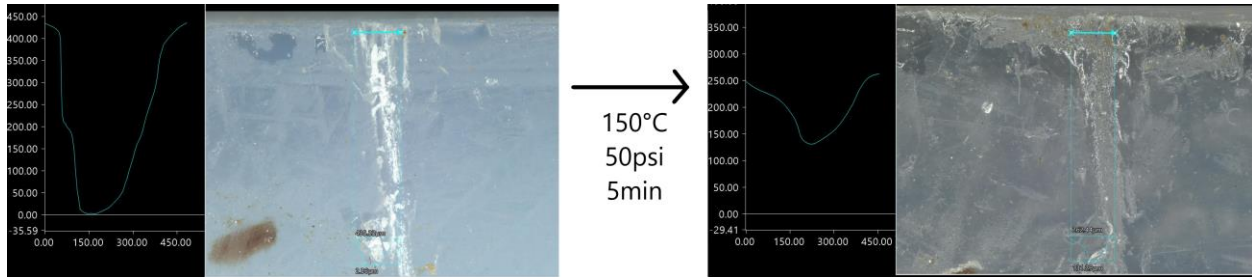


Figure 28. Topographical images before and after healing the self-healing polymer.

### 3.2.2.2. Tensile Properties of UV-Curable Vitrimer Resin

Tensile testing was performed on the base formulation, 0.5:1 methacrylic reactive diluent (MRD), and 1:1 MRD. With increasing MRD concentration, the strength, strain, modulus, and toughness all increased. The strength and modulus of the self-healing resin are less than that of the commercial resin while the strain and toughness are higher (Figure 29).

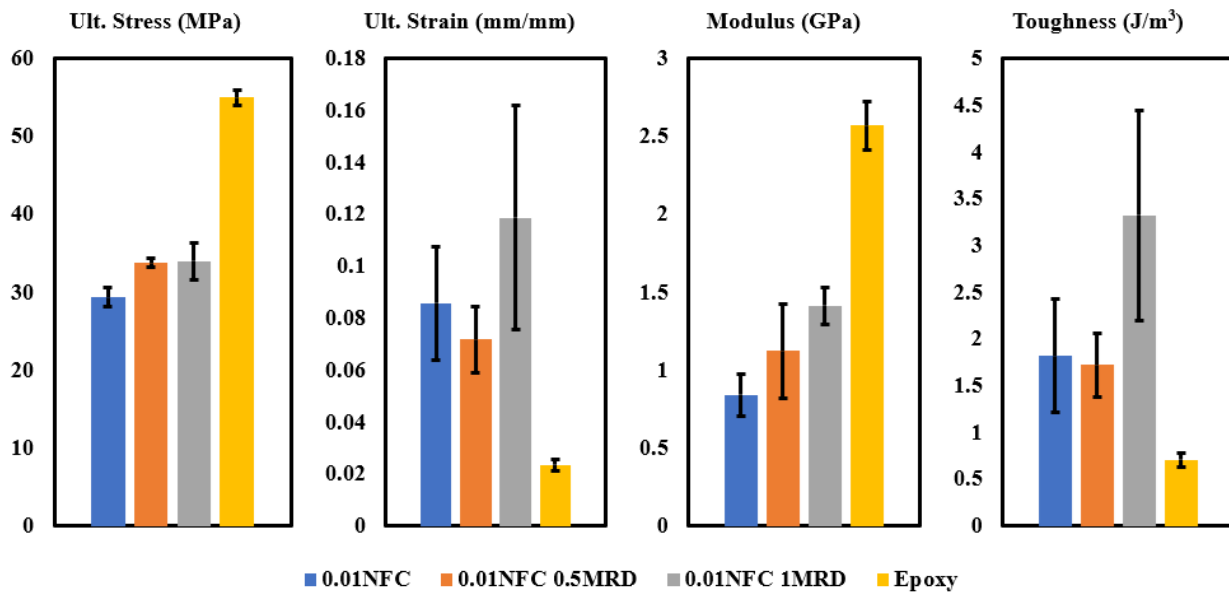


Figure 29. A summary of the tensile properties of the self-healing UV-curable resin compared to a commercial two-part epoxy system.

### 3.2. Task 3 Enhancing mechanical and bonding performances and reducing permeability of the healable CIPP structural lining through nanofiller

### 3.2.1. Task 3.1 High mechanical performance

#### 3.2.1.1. The morphology and particles size distribution of nanoparticles

The raw CNT, GNP, and ND nanoparticles are depicted in Figure 30 (a)-(c) using transmission electron microscopy (TEM) images. These high-resolution TEM visuals enable a detailed examination of the nanoparticles, which helps characterize the microstructures of all three distinct types.

Figure 30 clearly demonstrates that the nanoparticles can be classified as zero-dimensional (C60), one-dimensional (CNT), or two-dimensional (GNP) materials. This means that 0, 1, or 2 dimensions exceed 100 nm for each respective type. Such observations are in line with the study's assumptions, as one research goal was to evaluate the reinforcement properties offered by the unique shapes of these nanoparticles. Cylindrical carbon nanotubes (CNTs) with diameters between 50 and 100 nm were observed, while graphene nanoplatelets (GNPs) were seen as extremely thin, stacked single-layer sheets. Additionally, nanodiamonds displayed a consistent size distribution, with spherical particles averaging around 20 nm in diameter.

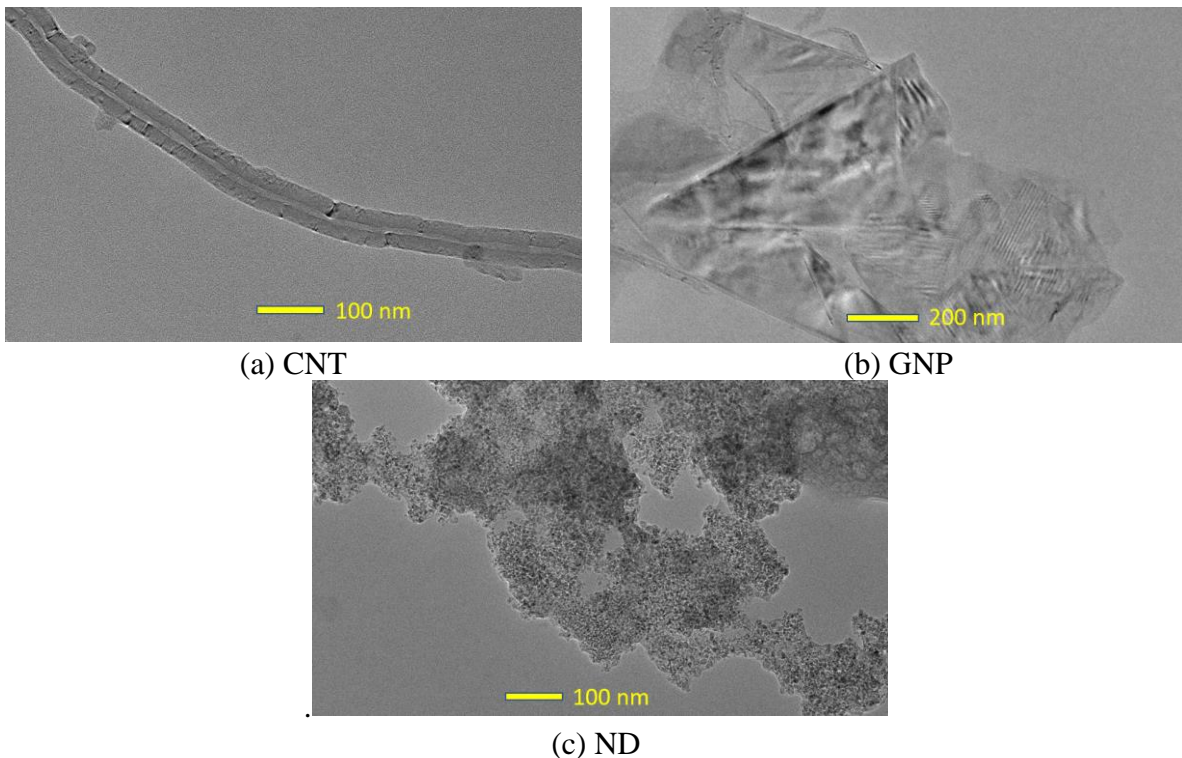


Figure 30. TEM image of (a) CNT, (b) GNP, and (c) ND

In order to characterize the particle size of the raw nanoparticle and also evaluate the effectiveness of the dispersion technique used (high-shear dispersion + ultrasonication), the particle size distribution of each type of nanoparticle was measured by the DLS technique. Results of the particle size distribution of nanoparticles before and after the dispersion procedure were depicted in Figure 31 (a) and (b), respectively.

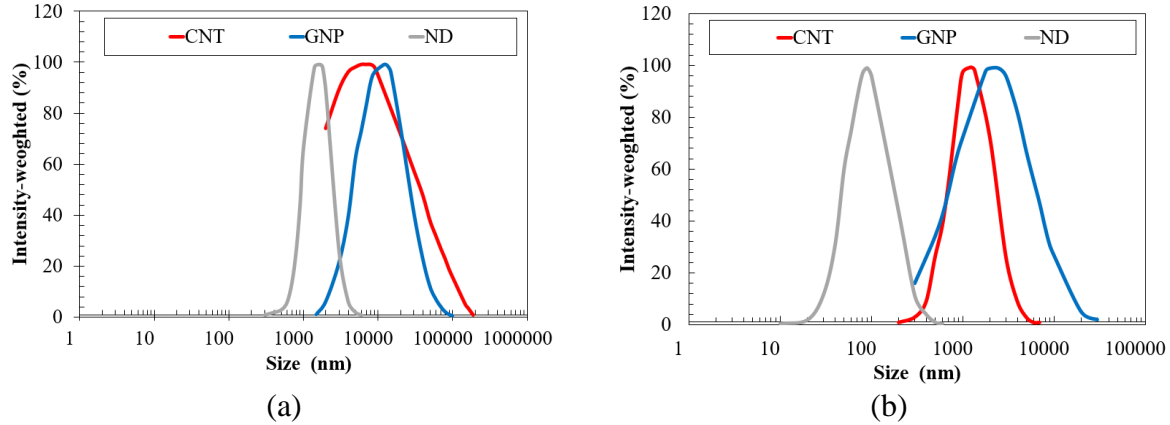


Figure 31. Particle size distribution (a) before and (b) after dispersion

Based on the results from Figure 31, the particle size of the tested CNT, GNP, and ND are ranged from  $10^3$ - $10^6$ ,  $10^3$ - $10^5$ , and  $10^2$ - $10^4$  nm, respectively. Apparently, all the nanoparticles have a high tendency to form agglomeration in their original state, which is reasonable due to the van der Waal forces are easily attract the nanoparticles to each together and the high surface area enhanced this effect [23]. The CNT nanoparticles ranged from 2000 to 100,000 nm, with a mean value of 18,000 nm. The GNP nanoplatelets are ranged from 1,000 to 100,000 nm; however, the mean value is 15,000 nm, and it is much smaller than CNT. On the other hand, the ND nanoparticles ranged from 200 to 6,000 nm, with a mean value of 1700 nm. The results indicated that the CNT has the highest tendency to form large-sized agglomerates in the composite, which is due to its fibrous shape and waviness that make the CNTs are easily to entangled with each other [24]. This assumption explains the reason why the largest-sized particles are found in CNT. On the other hand, the GNP is large because 1) even though the thickness is at the nanometer level (6-8 nm), the length and width are in micrometers (15 micrometers), and 2) the large surface area makes them easily to stack-up. The nanodiamonds (ND) were produced to 3-4 nm, and the particle size increased to an average of 1700 nm without applying any dispersion techniques. Therefore, results indicate that all nanoparticles have a tendency to form large-sized agglomerates due to the effect of van der Waal forces [25]; however, the size of agglomerates is highly dependent on the morphology and size of the individual particles.

The ability of the mechanical dispersion techniques to break down the particle is evaluated by measuring the particle size distribution after the dispersion process. As shown in Figure 31, the particle size of CNT was reduced to  $10^2$ - $10^4$ , where the original size was  $10^3$ - $10^6$  before dispersion. The GNP and ND were reduced to the range of  $10^2$ - $10^5$  and  $10^1$ - $10^2$ , respectively. Apparently, the combination of high-shear disperser and ultrasonication can effectively break down the nanoparticles agglomerates and reduce the particle size by over two order of degrees. At this point, the performance of nanocomposite will be significantly elevated by incorporating well-dispersed nanoparticles.

### 3.2.1.2. Viscosity of nanofiller-epoxy mixtures

The influence of adding CNT, GNP, and ND on the viscosity of epoxy is evaluated by a viscometer, and the results are presented in Figure 32. To directly indicate the influence of nanoparticles on the viscosity, changes on the value were presented by percentages, and pure epoxy

was considered as reference (100%). It is clear that the viscosity is highly dependent on the shape and concentration of the added nanoparticles. As shown in Figure 32 (a), CNT has the most influence on mixture's viscosity, compared to the GNP and ND. Significant increases were observed in all the tested concentrations due to the fibrous shape of CNTs, and the increase is highly dependent on the weight concentration of CNTs. The viscosity increased by 27%, 44%, and 342% when 0.5, 1.0, and 2.0% of CNTs were added, correspondingly. Apparently, the 2.0% of CNTs passed a threshold as the change in viscosity is much more significant compared to the others. On the other hand, the growth in viscosity in GNP-epoxy mixtures showed a close linear proportion to the weight concentration of GNPs, and the viscosity increased by 4%, 13%, and 45% when 0.5, 1.0, and 2.0% of GNPs were added, correspondingly. Differently, the spherical-shaped nanodiamonds have the least impact on the viscosity, the 0.5 and 1.0% groups decreased the viscosity by 5%, which contributed to the lubrication effect of nanodiamonds.

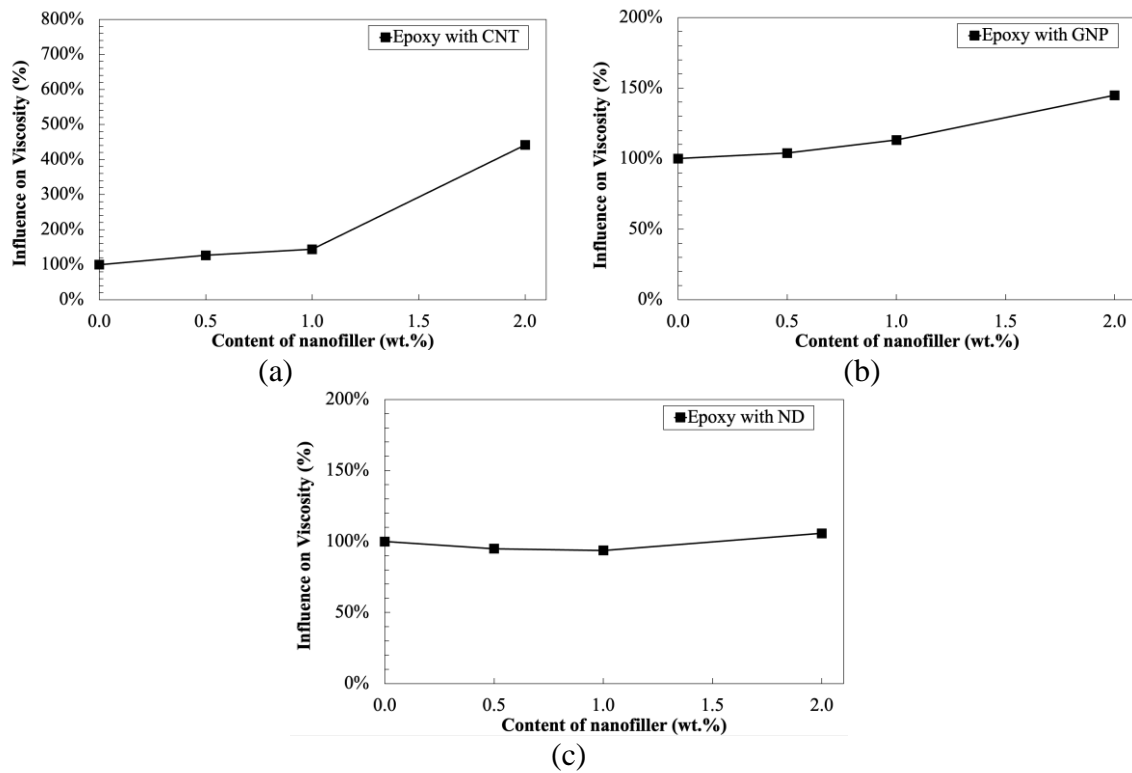


Figure 32. Influence of viscosity when adding (a) CNT, (b) GNP, and (c) ND nanoparticles

In conclusion, the study examined the effect of adding CNT, GNP, and ND nanoparticles on epoxy viscosity. The results indicate that viscosity is highly dependent on the shape and concentration of the nanoparticles. CNTs had the most significant influence on viscosity, while GNP-epoxy mixtures displayed a near-linear relationship with GNP concentration. Spherical-shaped nanodiamonds had the least impact, slightly decreasing viscosity due to their lubrication effect [26].

### 3.2.1.3. Tensile properties of developed nanocomposites

The tensile properties of nanocomposites are crucial for understanding the reinforcing ability of

nanoparticles and the performance of the developed nanocomposites. The influence of differently shaped nanoparticles (CNT, GNP, and ND) and weight concentration on the tensile strength and failure strain of epoxy-based nanocomposites are discussed below (Figure 33). Considering the overall results, the most significant enhancement in tensile strength was observed with 1.0 wt.% ND, showing a 52% improvement compared to pure epoxy. Furthermore, the 1.0% ND also demonstrated the highest increase in failure strain, which is twice as high as that of pure epoxy.

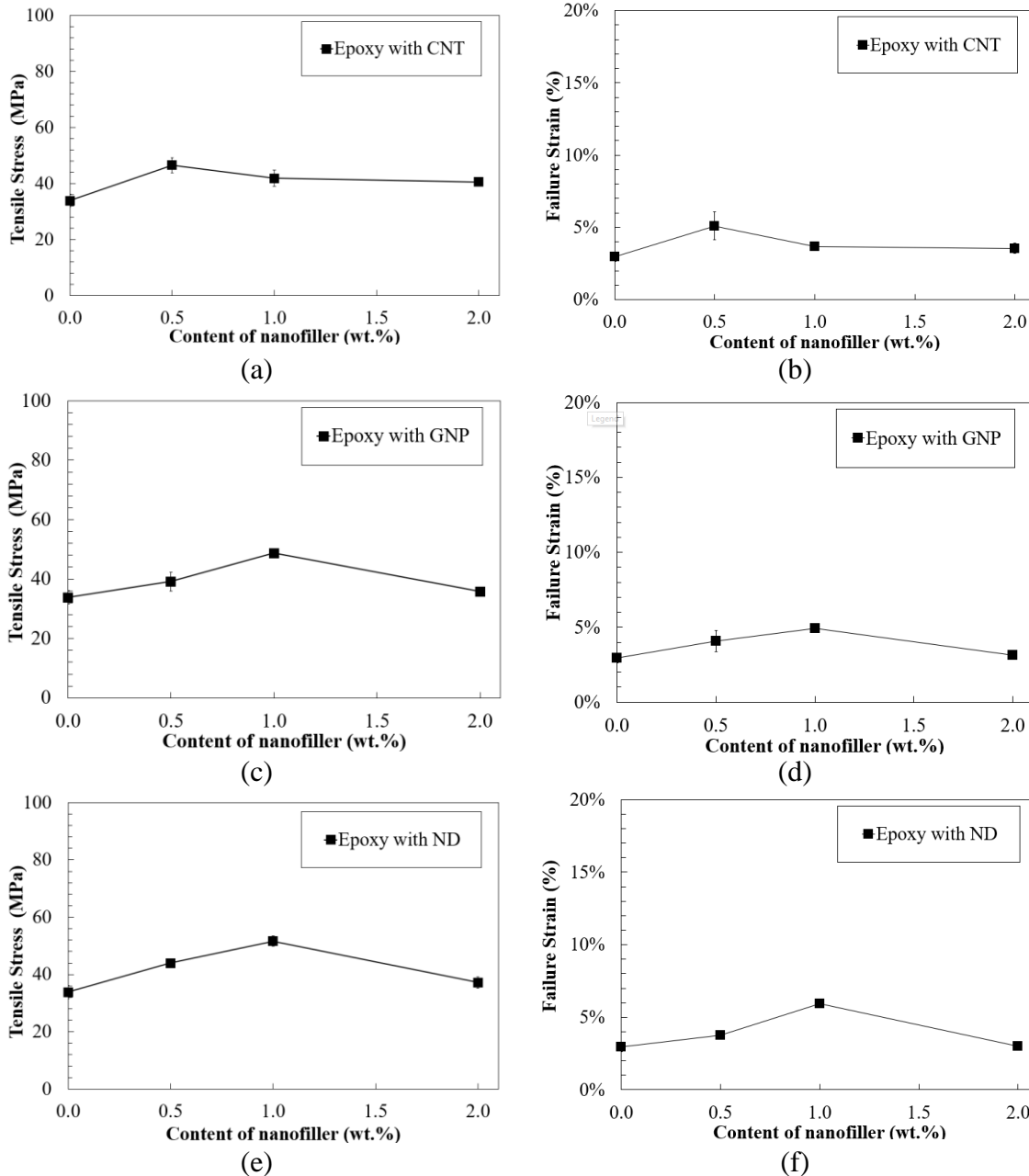


Figure 33. Tensile properties of (a)(b) CNT epoxy, (c)(d) GNP epoxy, and (e)(f) ND epoxy nanocomposites

For carbon nanotubes (CNT), the tensile strength increased with the addition of 0.5% CNT and then gradually decreased with higher concentrations. The failure strain showed a similar trend,

with an increase at 0.5% CNT, followed by a decrease at higher concentrations. The improvement in tensile properties could be attributed to the strong interaction between fibrous CNTs and the epoxy matrix, which enhances tensile strength and failure strain up to a certain concentration (0.5%). Beyond that, agglomeration and defects may negatively impact tensile properties once higher concentrations of CNTs are added (1.0 and 2.0%).

In the case of graphene nanoplatelets (GNP), the tensile strength increased at 1.0% GNP before dropping at 2.0% GNP. The failure strain experienced an increase when the concentration of GNP was up to 1.0% and a decrease at 2.0%. It seems that the high surface area of the platelet structure in GNPs can also form robust bonds with the epoxy matrix, enhancing tensile strength. Conversely, the negative effect caused by agglomeration was observed at higher concentrations compared to CNTs. This suggests that the 2-D structure is less prone to form agglomerates compared to 1-D nanoparticles.

For nanodiamonds (ND), the tensile strength reached a peak at 1.0% ND and then decreased at 2.0% ND. The failure strain showed a similar trend, with the highest value at 1.0% ND and then decreasing at 2.0% ND. The spherical shape of NDs may contribute to a better dispersion in the epoxy matrix, which could help in achieving improved tensile properties. However, at higher concentrations, the potential for agglomeration or defects may increase, leading to a reduction in tensile strength and failure strain.

The observed changes in tensile properties for nanocomposites containing CNTs, GNPs, and NDs can be attributed to various mechanisms such as the shape of the nanofiller, the interaction between the nanofiller and the polymer, and the influence of agglomerates on material performance. The shape and content of the nanofiller can have a substantial effect on the performance of the nanocomposite. A proper concentration of the nanofiller must be found, as too much agglomeration can negate the positive effects of the nanofiller. Optimizing the concentration and dispersion of nanofillers within the polymer matrix is critical to achieving the desired performance of nanocomposites.

As presented in Figure 34, the Scanning Electron Microscopy (SEM) images of the fracture surfaces after the tensile test provide valuable insights into the impact of nanoparticles on the mechanical properties of the epoxy-based nanocomposites. The observations reveal differences in the fracture surfaces of pure epoxy and nanocomposite samples, which can be linked to their overall mechanical performance.

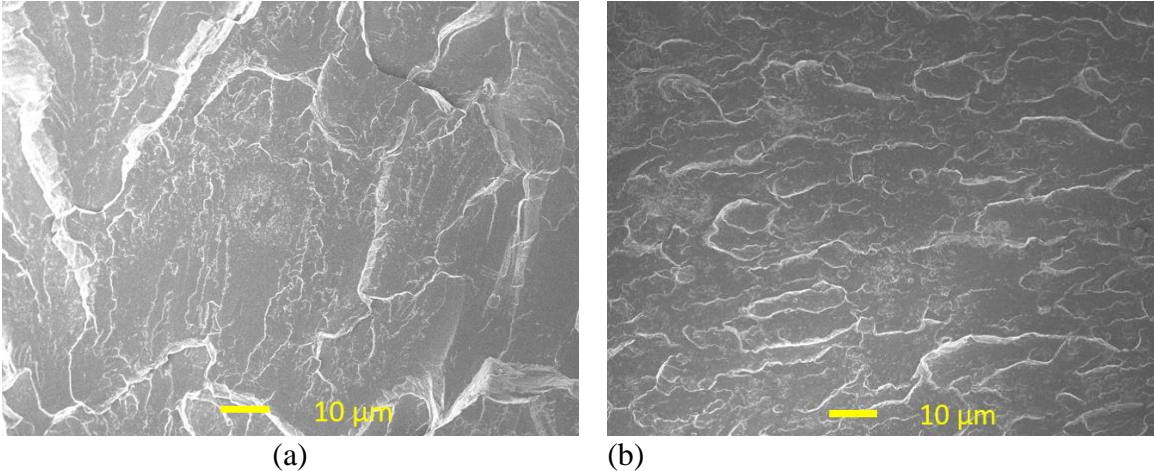


Figure 34. SEM image of fracture surface for (a) pure epoxy and (b) CNT epoxy

For pure epoxy samples, the SEM images display large fracture textures, which are indicative of a combination of plastic and brittle behavior. This characteristic is typically associated with low impact resistance and fracture toughness, resulting in weaker mechanical properties when subjected to tensile stress. In contrast, the fracture surfaces of nanocomposite samples with incorporated nanoparticles exhibit a rougher surface accompanied by compacted cracking cleavages. This observation suggests that the presence of nanoparticles enhances the energy absorption capacity of the material, leading to better resistance to fracture [27]. The rougher surface and compacted cleavages are likely a result of improved interaction between the nanoparticles and the epoxy matrix, which promotes more effective load transfer and energy dissipation during tensile testing.

#### 3.2.1.4. Abrasion resistance of developed nanocomposites

As illustrated in Figure 35, the impact of CNT, GNP, and ND with varying weight concentrations on the wear resistance of the nanocomposite was assessed by analyzing mass loss following the abrasion test. For carbon nanotubes, the addition of CNTs to the epoxy led to an improvement in wear resistance, with mass loss decreasing by 9% at 0.5% CNT, 40% at 1.0% CNT, and 52% at 2.0% CNT. For graphene nanoplatelets (GNP), there was no significant change in the mass loss at 0.5% GNP. However, when 1.0% of GNP was added, the mass loss decreased by 18%; furthermore, the reduction was substantial at 53% when 2.0% of GNP was incorporated.

For nanodiamonds, the mass loss followed a different trend than GNP. At the sample group with 0.5% ND, substantial reinforcement on abrasion resistance was observed, with a 24% decrease in mass loss. When 1.0% and 2.0% ND were incorporated into the epoxy matrix, there was a significant reduction (above 60%) in the mass loss. These findings demonstrate that the shape and weight concentration of nanoparticles play a crucial role in the wear resistance of epoxy. The addition of CNTs, GNPs, and NDs all contribute to a reduction in mass loss, the highest improvement was found at ND (0D), with the most significant improvements observed at higher weight concentrations.

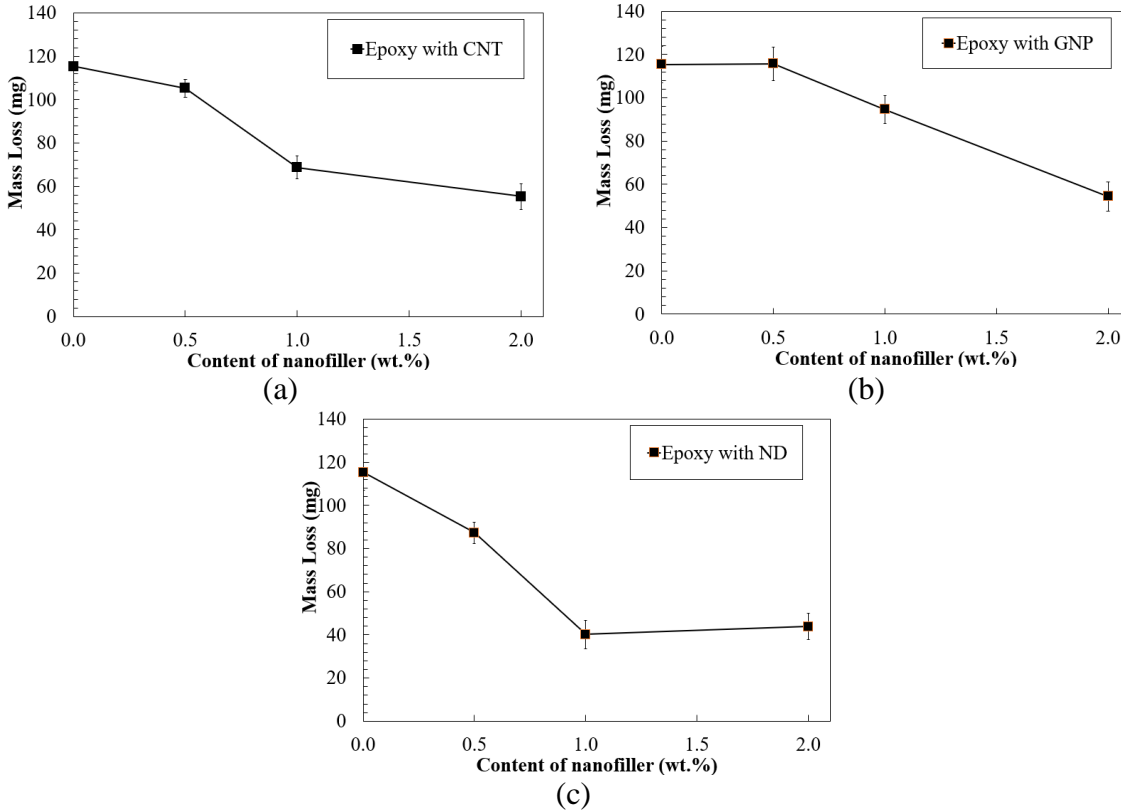


Figure 35. Abrasion resistance in terms of mass loss for (a)CNT epoxy, (b) GNP epoxy, and (c) ND epoxy nanocomposites

The changes in wear resistance upon the addition of nanoparticles (CNT, GNP, and ND) to the epoxy can be attributed to various mechanisms, including agglomeration of nanoparticles at higher concentrations, the interaction between differently shaped nanoparticles and the polymer, defects in nanocomposites, and load transferability of nanoparticles in the polymer. The interaction between differently shaped nanoparticles and the polymer can significantly impact wear resistance, by providing strong interlocking, enhanced load transferability, or lubrication effects.

The Scanning Electron Microscopy (SEM) images of the abraded surfaces after the abrasion test offer valuable insights into the wear resistance of pure epoxy and epoxy-based nanocomposites. As presented in Figure 36, the observations reveal differences in the abraded surfaces, which can be associated with the material's ability to withstand wear forces.

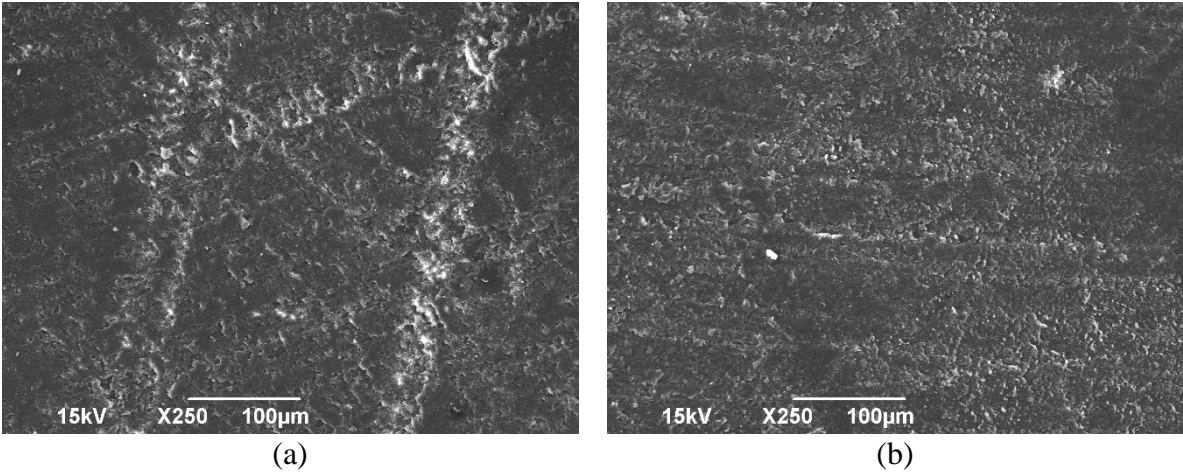
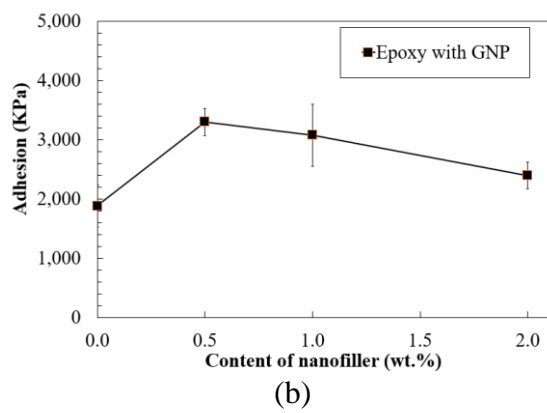
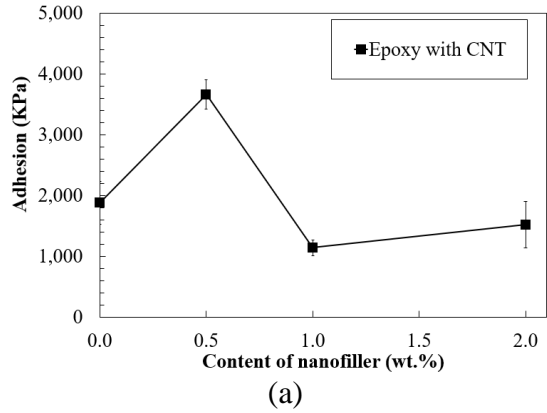


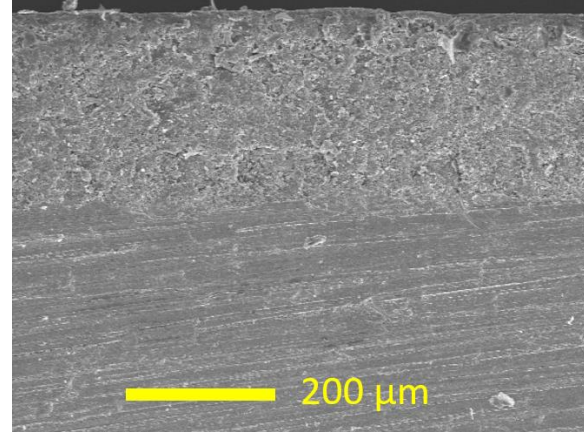
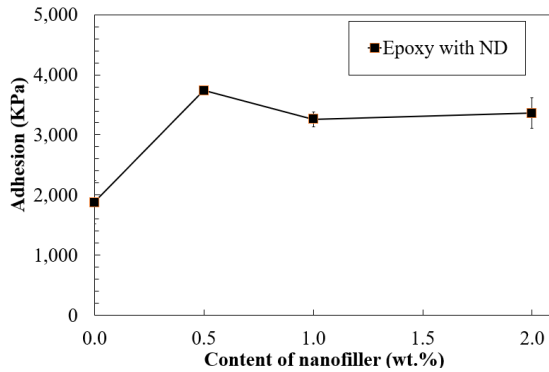
Figure 36. SEM image of abraded surface for (a) pure epoxy and (b) CNT epoxy

For pure epoxy samples, the SEM images display large fracture textures, suggesting plastic deformation. This characteristic indicates low load transferability to wear forces, resulting in low wear resistance. Consequently, pure epoxy materials may not perform well under abrasive conditions due to their inherent mechanical limitations. On the other hand, the abraded surfaces of nanocomposite samples with incorporated nanoparticles exhibit a smoother surface with fewer and smaller cracks[28]. This observation indicates that the tested nanocomposites have greater resistance to abrasion, suggesting that the presence of nanoparticles in the epoxy matrix improves the material's load transferability to wear forces. The enhanced wear resistance can be attributed to the strong interfacial interactions between the nanoparticles and the epoxy matrix, which help to distribute wear forces more effectively across the material.

3.2.1.5. Adhesion of developed nanocomposites

The adhesion strength of nanocomposite to steel substrate is an important property, as it directly impacts the overall performance of the nanocomposite coating (Figure 37). The influence of CNT, GNP, and ND with varied weight concentrations on the adhesion strength is discussed below.





(c)

(d)

Figure 37. Adhesion between nanocomposite and steel substrate for (a)CNT epoxy, (b) GNP epoxy, and (c) ND epoxy nanocomposites. (d) Cross-section image of coating substrate interface

The cross-section SEM images were captured and Figure 37 (d) is used as a representative; all the nanocomposites showed strong interfacial bonding without obvious defects at the interface. Therefore, the adhesion of the tested nanocomposite was solely dependent on the bond between the nanocomposite and substrate.

For carbon nanotubes (CNT), the addition of CNTs to the epoxy led to varied results. The adhesion strength increased substantially at 0.5% CNT, while it decreased when 1.0% and 2.0% CNT were added. This could be attributed to the strong interaction between the fibrous CNTs and the epoxy matrix, which improves adhesion at certain concentrations, while at higher concentrations, agglomeration may negatively affect the adhesion strength. Graphene nanoplatelets increased the adhesion strength at lower concentrations of GNPs (0.5% and 1.0%) and then decreased at 2.0% GNP. Apparently, the platelet structure of GNPs can also improve the adhesion strength of nanocomposite. However, at higher concentrations, the GNP-epoxy interaction may be hindered due to agglomeration, leading to a reduction in adhesion strength. For nanodiamonds, the adhesion strength increased consistently with the addition of NDs at all weight concentrations. The spherical shape of NDs also contribute to improving the interlocking properties of nanocomposite, which could help in achieving better adhesion strength between the epoxy and the steel substrate.

In summary, the findings demonstrate that the shape and weight concentration of nanoparticles play vital roles in the adhesion strength of nanocomposite coatings to the steel substrate. The addition of CNTs, GNPs, and NDs all contribute to varying degrees of adhesion strength improvement.

### 3.2.1.6. Flexural properties of developed nanocomposites

Continuing with previous study, study in this period focuses on evaluating the influence of nanoparticles on the flexural properties of polymeric composite. Consistent with previous study, the nanoparticles include carbon nanotubes (CNT), graphene nanoplatelets (GNP), and nanodiamonds (ND). It can be seen from Figure 38 that the optimal concentration for these investigated nanoparticles is between 0.5 to 1.0 wt.%.

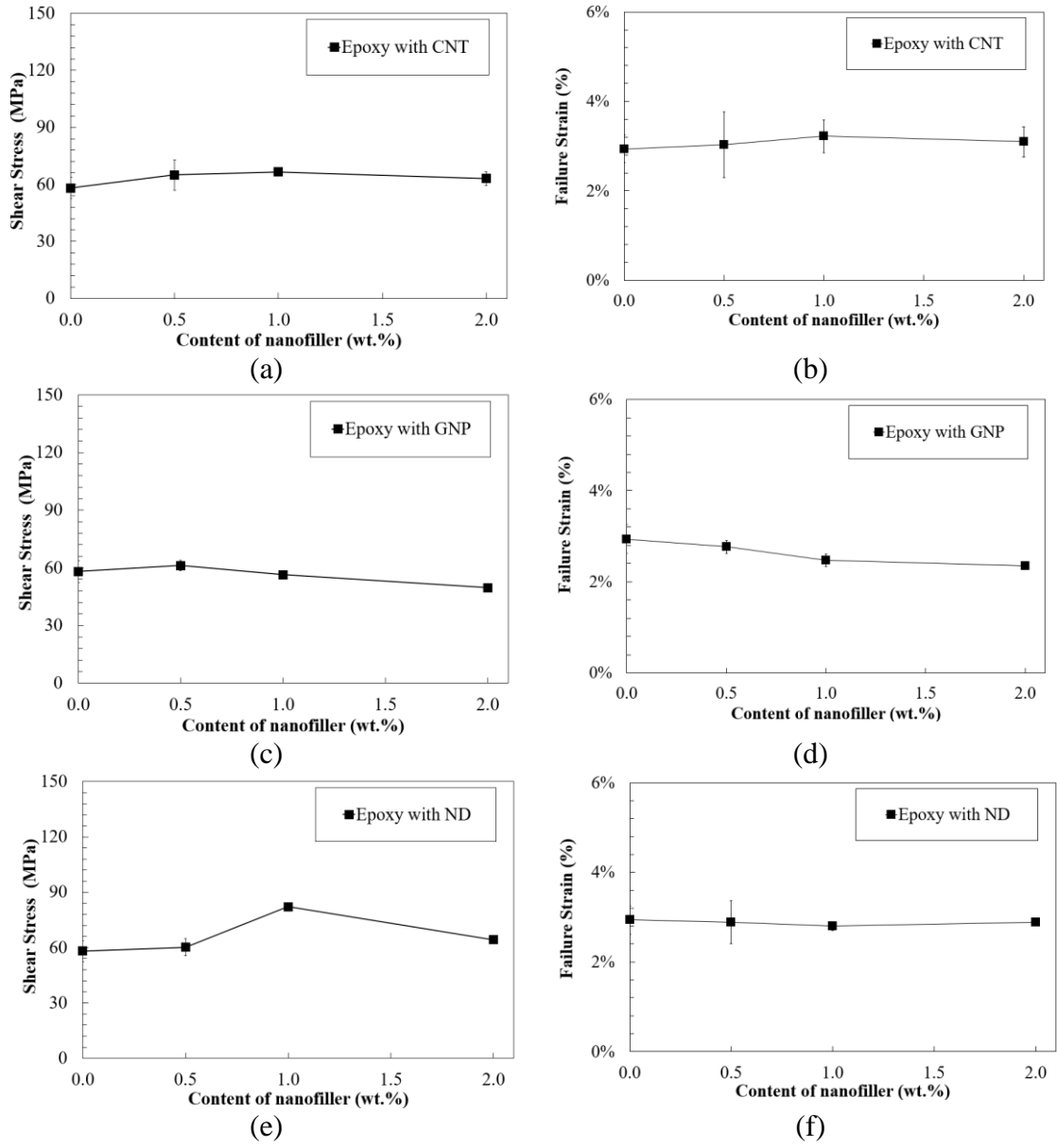


Figure 38. Figure 4. Flexural properties of neat epoxy with and without nanoparticle reinforcement. (a)-(b) Epoxy with CNT, (c)(d) Epoxy with GNP, and (e)(f) Epoxy with ND

3.2.1.7. Water contact angle of developed nanocomposites

The water contact angle measurements provide important information about the wettability of epoxy-based nanocomposites reinforced with CNT, GNP, and ND, as presented in Figure 39. Interestingly, the addition of these nanoparticles, regardless of their concentration, does not lead to significant changes in the water contact angle. The pure epoxy has a water contact angle of around 55 degrees, while nanocomposites exhibit values around 60 degrees.

The wettability of a surface depends on two factors: 1) the surface tension of the materials themselves, and 2) the texture of the surface [29]. Since the results from water contact angle showed no significant changes, it can be suggested that the incorporation of nanoparticles does not

significantly affect either of these factors. This observation may be caused by the fact that the nanoparticles were evenly dispersed into the epoxy matrix, consequently, all the nanoparticles are covered by epoxy in the matrix and maintaining the overall surface properties of the material.

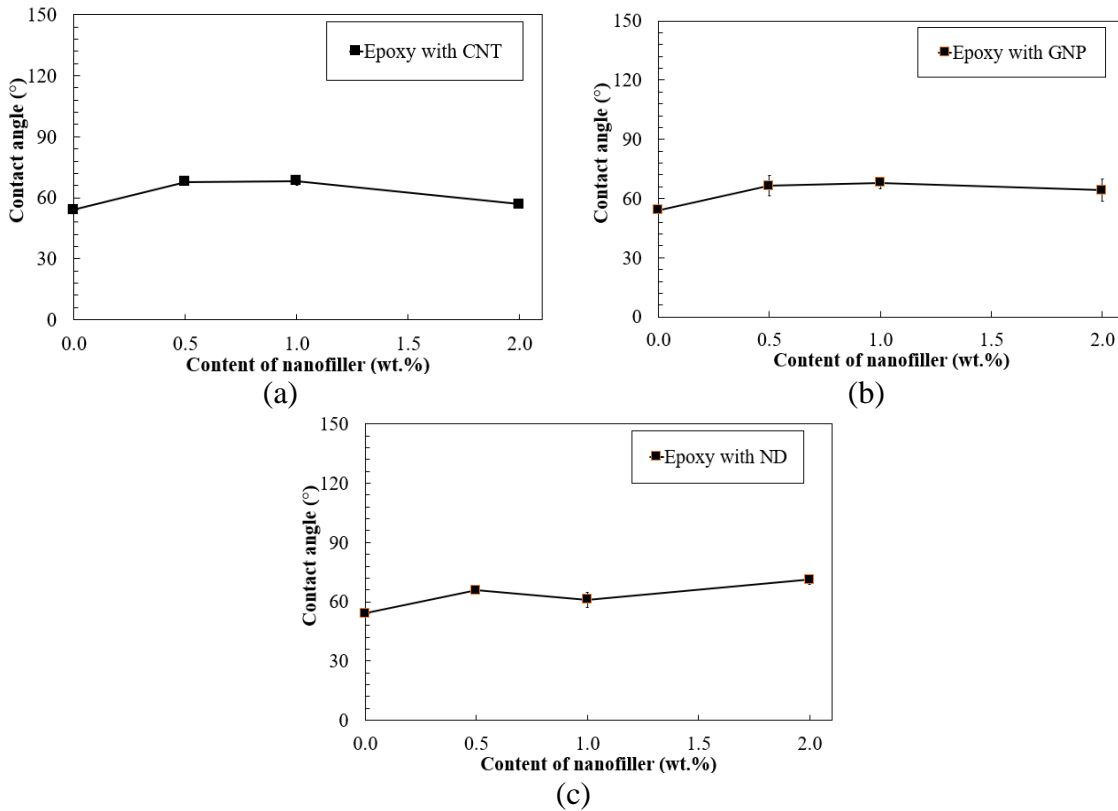


Figure 39. Water contact angle of (a)CNT epoxy, (b) GNP epoxy, and (c) ND epoxy nanocomposites.

### 3.2.1.8. Findings and conclusions

In conclusion, this study has thoroughly investigated the influence of different shaped nanoparticles, including carbon nanotubes (CNT, 1D), graphene nanoplatelets (GNP, 2D), and nanodiamonds (ND, 0D), on the performance of epoxy-based nanocomposites. The effects of varying weight concentrations of these nanoparticles were also assessed, providing valuable insights into the relationship between nanoparticle shape, concentration, and the resulting properties in the nanocomposites.

- The comprehensive experimental studies, such as TEM/SEM imaging, particle size distribution, viscosity tests, tensile properties tests, abrasion resistance tests, adhesion to the substrate, and wettability, have led to several key findings that shown below:
- The shape and concentration of nanoparticles play a significant role in the properties of nanocomposites, such as viscosity, tensile/flexural properties, and wear resistance.
- The tensile/flexural properties showed that the addition of CNT, GNP, and ND improved the strength and failure strain of the epoxy-based nanocomposites to varying degrees,

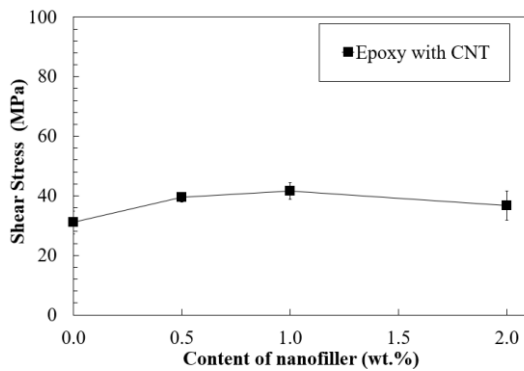
depending on the shape and concentration of the nanoparticles.

- The abrasion resistance of the nanocomposites was significantly enhanced with the incorporation of CNT, GNP, and ND. The smoother surface and reduced number of cracks observed in the SEM images of the abraded surface demonstrated the increased load transferability to wear forces and improved wear resistance.
- The adhesion strength of the nanocomposite coatings to the steel substrate increased with the addition of nanoparticles.
- The water contact angle showed no significant changes upon the addition of CNT, GNP, and ND nanoparticles, regardless of their concentration. This suggests that the wettability of the nanocomposites remains relatively constant, as both surface tension and texture of the materials are not significantly impacted by the addition of these nanoparticles.

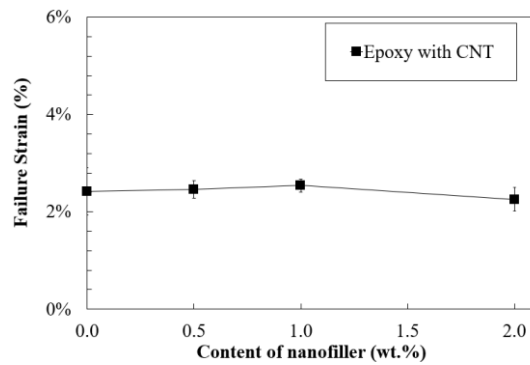
Several key factors contribute to the observed changes in nanocomposite properties: such as 1) the dispersion and agglomeration of nanoparticles, 2) the interaction between nanoparticles and the polymer matrix, which is determined by the morphology of nanoparticles, and 3) the influence of nanoparticles on the viscosity of mixtures, which increased viscosity directly results in the defects in the composite.

### 3.2.2. Task 3.2 Enhanced bonding performance

Continuing with previous study on nanocomposite performance evaluation, study in this period focuses on evaluating the influence of nanoparticles on the shear bonding properties. Figures 40 show the testing results for the flexural properties with epoxy composite reinforced with CNT, GNP, and ND. It can be seen that the optimal concentration for these investigated nanoparticles is between 0.5 to 1.0 wt.%.



(a)



(b)

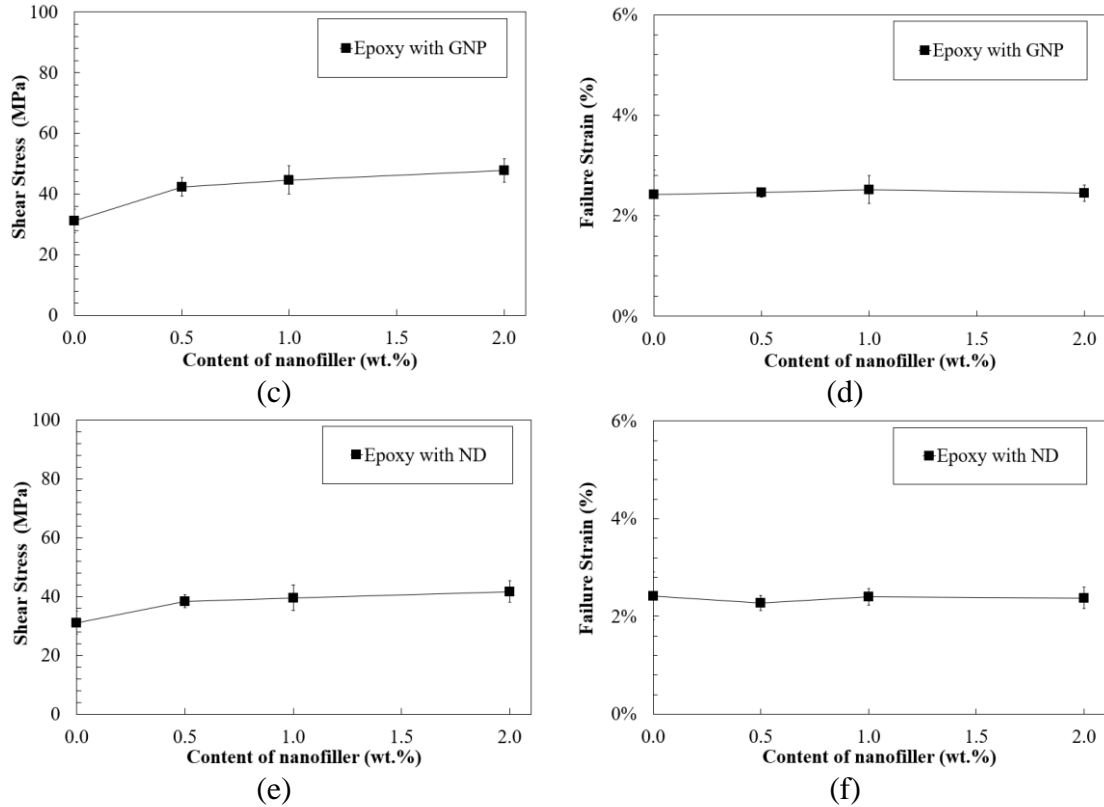


Figure 40. Single Lap Joint adhesion of neat epoxy with and without nanoparticle reinforcement. (a)-(b) Epoxy with CNT, (c)(d) Epoxy with GNP, and (e)(f) Epoxy with ND

### 3.2.3. Task 3.3 Reducing the permeability and investigating the interfacial bonding chemical analysis

#### 3.2.3.1. Hydrogen models based on their density and self-diffusion properties

To assess the performance of different hydrogen models, we tested four models: two united models from Buch [30] and Frost [31], and two 2-site models from Cracknell [32] and Yang [33]. Our evaluation focused on comparing the predicted density and bulk self-diffusion properties at different temperatures. The results, presented in the tables and figure below, indicate that the united model proposed by Forst et al. exhibits satisfactory accuracy in predicting these properties in bulk hydrogen across varying temperatures and pressures.

By systematically evaluating these hydrogen models, we can make an informed choice regarding the most suitable model for our future simulations of hydrogen permeability in self-healable epoxy resin. These findings provide a solid foundation for further investigations and design of molecular dynamics simulations to explore the behavior of hydrogen in the selected polymer systems.

Table 10 Density & Self-Diffusion Properties of Bulk Hydrogen at 1 atm.

T (K)	Experimental $\rho$ (g/cm <sup>3</sup> )	Buch <sup>1</sup> United Model		Frost et al. <sup>2</sup> United Model		Cracknell <sup>3</sup> Two-Site Model		Yang & Zhong <sup>4</sup> Two-Site Model	
		$\rho$ (g/cm <sup>3</sup> )	error	$\rho$ (g/cm <sup>3</sup> )	error	$\rho$ (g/cm <sup>3</sup> )	error	$\rho$ (g/cm <sup>3</sup> )	error
90.3	2.72E-04	2.72E-04	<b>0.14%</b>	2.72E-04	<b>0.13%</b>	2.75E-04	<b>1.13%</b>	2.76E-04	<b>1.26%</b>
273	9.00E-05	8.99E-05	<b>0.02%</b>	9.01E-05	<b>0.14%</b>	9.06E-05	<b>0.80%</b>	9.01E-05	<b>0.22%</b>
293.2	8.38E-05	8.39E-05	<b>0.06%</b>	8.38E-05	<b>0.03%</b>	8.33E-05	<b>0.56%</b>	8.44E-05	<b>0.68%</b>

T (K)	Experimental $D_s$ (cm <sup>2</sup> /s)	Buch <sup>1</sup> United Model		Frost et al. <sup>2</sup> United Model		Cracknell <sup>3</sup> Two-Site Model		Yang & Zhong <sup>4</sup> Two-Site Model	
		$D_s$ (cm <sup>2</sup> /s)	error	$D_s$ (cm <sup>2</sup> /s)	error	$D_s$ (cm <sup>2</sup> /s)	error	$D_s$ (cm <sup>2</sup> /s)	error
90.3	0.192	0.170	<b>11.23%</b>	0.174	<b>9.55%</b>	0.219	<b>14.15%</b>	0.211	<b>9.84%</b>
273	1.285	1.257	<b>2.16%</b>	1.278	<b>0.56%</b>	1.298	<b>1.00%</b>	1.183	<b>7.94%</b>
293.2	1.400	1.490	<b>6.39%</b>	1.395	<b>0.34%</b>	1.427	<b>1.93%</b>	1.352	<b>3.44%</b>

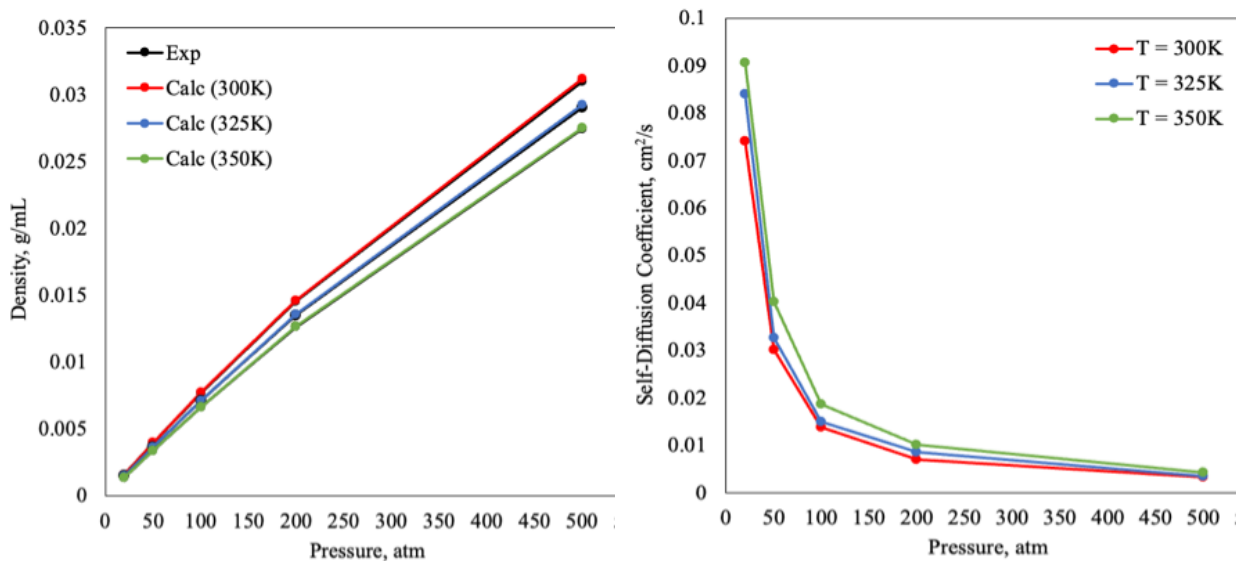


Figure 41. Density and Self-Diffusion of Bulk Hydrogen at Varying Temperatures and Pressures: the Frost et al. [31] United Model vs the Experimental Measurements [32].

### 3.2.3.2. Pore chemistry effect on the self-diffusion of hydrogen in pores

As presented in Figure 42, at low pressures, self-diffusion coefficients demonstrate that H<sub>2</sub> diffusion is faster in graphene pores than in kaolinite nanopores, despite H<sub>2</sub> having stronger attractive intermolecular interactions with graphene. Lateral VACF results reveal a faster decay time for H<sub>2</sub> molecules in kaolinite, suggesting that H<sub>2</sub> molecules have more collisions with the kaolinite surface than the graphene surface. So, slower self-diffusion in kaolinite may be explained by greater surface roughness.

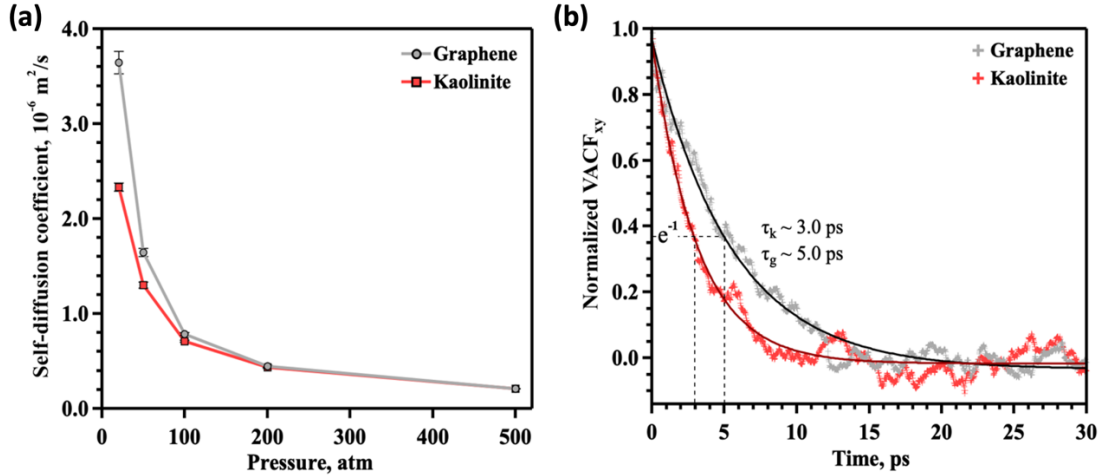


Figure 42. Diffusion behavior of  $\text{H}_2$  in 2 nm kaolinite (Al surface) and graphene pores. (a) Total self-diffusion coefficients at pressures ranging from 20-500 atm. (b) Normalized lateral velocity autocorrelation functions at  $P = 20 \text{ atm}$ .

### 3.2.4. Task 3.4 Finite element numerical analysis to guide the design of the developed high-performance healable CIPP structural liner

#### 3.2.4.1. Subgrade loading results.

The subgrade load is an important and permanent factor for pipe and liner design. This section presents the effect of buried depth and epoxy resin liner thickness on the mechanical performance of cast-iron pipelines. In the simulation of external subgrade loading, no internal pressure is considered. Figure 43(a) shows the relationship between the maximum principal stress and the buried depth for the bare pipe and the pipe rehabilitated with the 4mm CIPP liner. The maximum principal stresses increase with the buried depth for both types of pipes, caused by the increased subgrade load. Compared to the bare pipe, the maximum principal stresses of the lined pipe are reduced by 31.3%, 20.2%, and 14.2% at the 1, 2, and 3 m buried depth, respectively. The results show the improvement of the mechanical performance of the liner rehabilitation on the cast-iron pipe. Figure 43(b) shows the relationship between vertical displacement and the buried depth for the bare pipe and the pipe rehabilitated with the 4mm CIPP liner. It is shown that the vertical displacement decreases with the increase of buried depth for both bare pipe and lined pipe. The surrounding subgrade is consolidated due to the natural settlement. Therefore, more load dissipates as more subgrade is considered. The results align with the previous [34], where the vertical displacement of the pipeline had no obvious change with liner rehabilitation. This is because the pipeline displacement was mainly affected by surface loading even with liner rehabilitation.

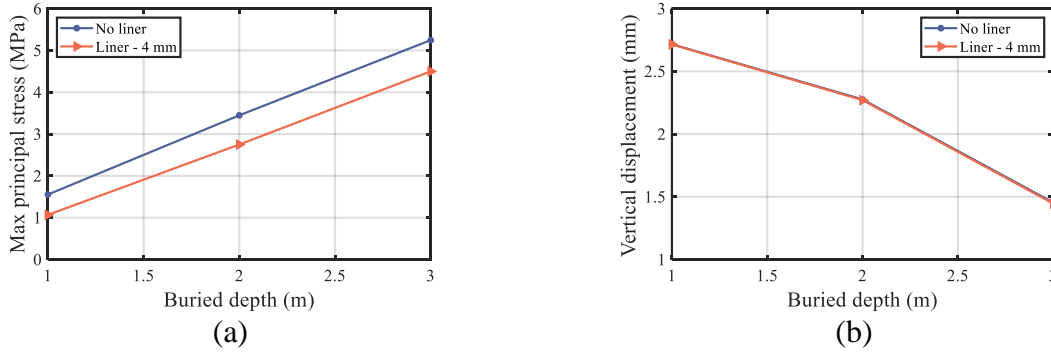


Figure 43. Mechanical performance of the cast-iron pipe with and without liner rehabilitation under subgrade load: (a) maximum principal stress versus buried depth; (b) vertical displacement versus buried depth.

Figure 44(a) shows the parametric study results regarding the effect of buried depth and CIPP liner thickness on the cast-iron pipe. The maximum principal stress of the pipe increases with the buried depth, while decreases with liner thickness. The von Mises stress of epoxy resin liner with different thicknesses and buried depths is shown in Figure 44(b). With the presence of CIPP liner and increased liner thickness, the maximum principal stress of pipeline continuously decreased, while the von Mises stress of liner increased. the liner bears up to 40% of the total stress. Figure 44(c) shows the relationship between the stresses in cast-iron pipe and 2mm liner with different buried depth. It is shown that the buried depth has little effect on the stress in liner, while the stress in pipeline increases significantly with the buried depth. It is the pipe that bears most of the subgrade load before the pipe is damaged. Similar results were presented by [14].

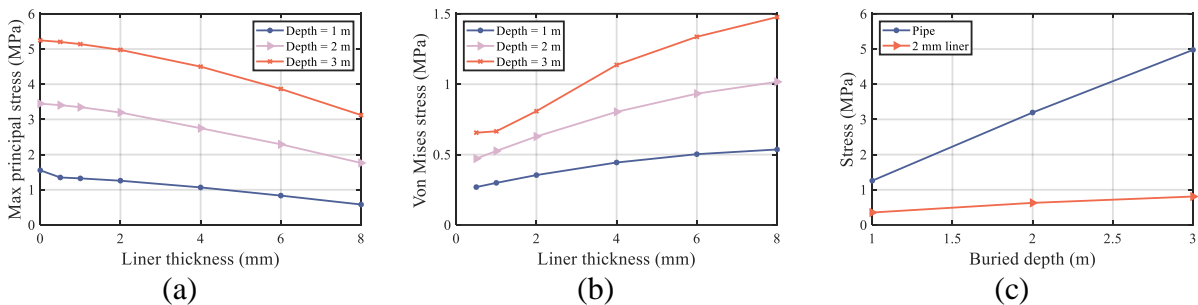


Figure 44. (a) The relationship between maximum principal stress of cast-iron pipe and liner thickness at different buried depth; (b) the relationship between von Mises stress of epoxy resin liner and liner thickness at different buried depth; (c) stress in the cast-iron pipe (blue) and the epoxy resin liner (red) versus buried depth.

### 3.2.4.2. Internal in-pipe pressure results.

The effect of internal in-pipe pressure on the mechanical performance of pipe-liner system is studied in this section. According to the American Water Works Association (AWWA) Manual of Water Supply Practices [35], the specific maximum working pressure of pipeline with the diameter up to 78 inches is 250 psi (1.72 MPa). Therefore, pipelines rehabilitated by epoxy resin liner with seven thicknesses (from 0 to 8 mm) and three internal pressures (1, 1.5, and 2 MPa) are simulated with the finite element models. Figure 45(a) shows the relationship between the maximum

principal stress of the pipe and the in-pipe pressure for the bare pipe and the pipe rehabilitated with the 4mm CIPP liner. The maximum principal stress of cast-iron pipe decreases by 6.6% as rehabilitated by CIPP liner. Figure 45(b) shows the vertical displacements versus in-pipe pressure of the bare pipe and the lined pipe. The vertical displacement of the lined pipe is relatively stable compared to the bare pipe, showing the effectiveness of the CIPP liner in displacement restoration.

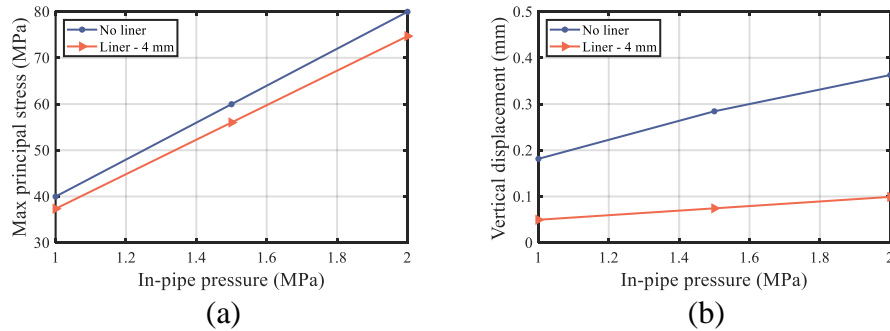


Figure 45. Mechanical performance of the cast-iron pipe with and without liner rehabilitation under in-pipe pressure: (a) maximum principal stress versus in-pipe pressure; (b) vertical displacement versus in-pipe pressure.

The effect of liner thickness and in-pipe pressure on cast-iron pipe mechanical performance are illustrated in Figure 46(a). The maximum principal stress of the pipe decreases as the liner thickness and internal pressure decrease. With a 15 mm-thick epoxy resin liner, the pipe stress decreases by 16.5%. Figure 46(b) shows the von Mises stress of the liner under the various in-pipe pressure and liner thicknesses. With the increase of liner thickness and in-pipe pressure, the von Mises stress of liner decreases. From the results, it is shown that stresses in the liner are mainly affected by internal in-pipe pressure. Thicker liners result in the smaller liner stress and bears the in-pipe pressure more evenly. The results are well aligned with the published results by [36], where the authors analyzed the in-pipe pressure and concluded that stress and vertical displacement of pipeline and liner increased with in-pipe pressure. It is recommended that CIPP liner thickness should increase as the in-pipe pressure increases.

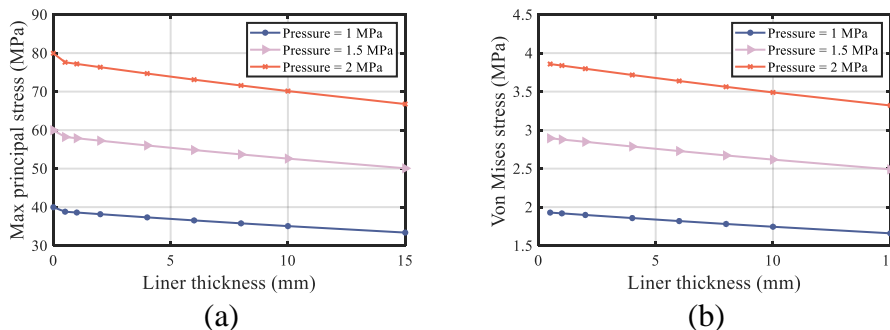


Figure 46. (a) The relationship between maximum principal stress of cast-iron pipe and liner thickness with different in-pipe pressure; (b) the relationship between von Mises stress of epoxy resin liner and liner thickness with different in-pipe pressure.

The computational analysis of the pipe-liner shows the rehabilitation effect of CFRP liners with various thicknesses and in-pipe pressure on the mechanical responses of the damaged cast-iron

pipes. Different thicknesses of CFRP liner (ranging from 0 mm to 8 mm) are used to rehabilitate pipes with in-pipe pressure of 1 MPa, 1.5 MPa, and 2 MPa. Figure 47(a) shows the maximum principal stress of cast-iron pipe, and Figure 47(b) displays the displacement of the pipe with different CFRP liner thicknesses and in-pipe pressure. The figures exhibit that stress and displacement of the cast-iron pipe decrease with the increase of the liner thickness and the decrease of the in-pipe pressure. The rehabilitation effect of CFRP liner is the most obvious when the thickness is increased from zero to 2 mm, resulting in a 76% decrease in pipe stress and an 81% decrease in pipe displacement. The findings are well aligned with the results of [36], who conducted a numerical analysis to study the rehabilitation effect of the GFRP on concrete pipes and stated that increasing the GFRP liner thickness to 3 mm greatly improved the mechanical performance of the pipe. The FEA results in the section indicate that implementing a CFRP liner and increasing its thickness can effectively enhance the structural integrity of the damaged cast-iron pipe.

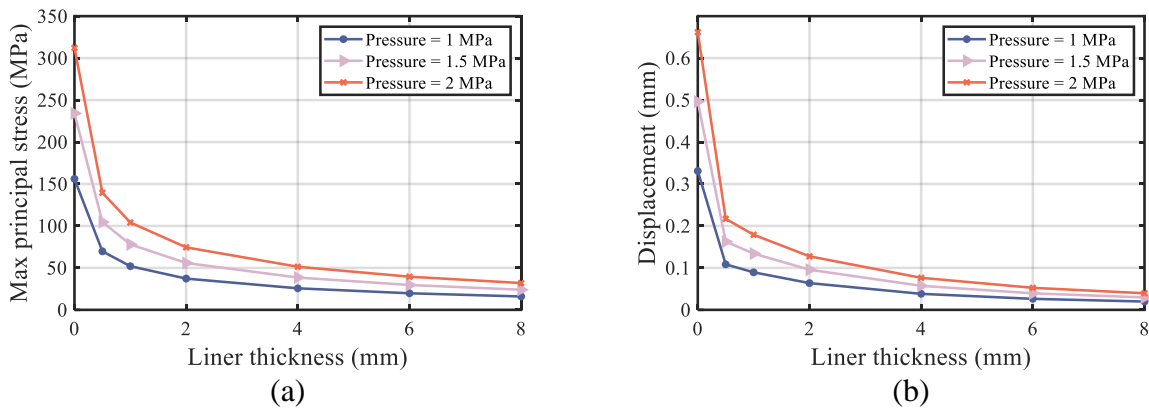
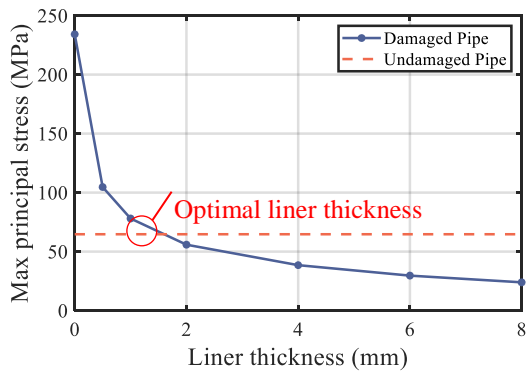


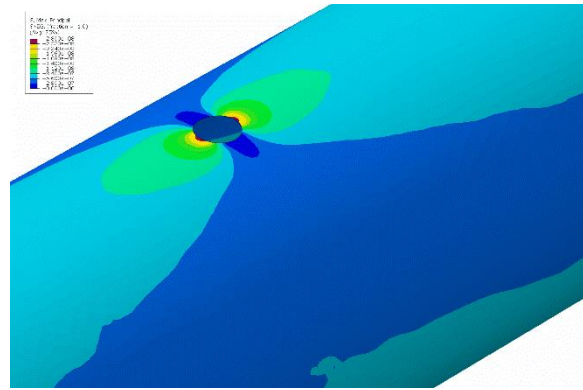
Figure 47. Mechanical responses of the cast-iron pipe versus CFRP liner thickness under different in-pipe pressure conditions.

Additionally, we conduct a parametric study and compare an undamaged cast-iron pipe with damaged cast-iron pipes rehabilitated by CFRP liners with different liner thicknesses. All pipes are exposed to 1.5 MPa in-pipe pressure. Figure 48(a) shows the maximum principal stress of the pipes. The red dashed line shows the response of the undamaged pipe under 1.5 MPa without any rehabilitation, and the blue dot line shows the performance of damaged pipes rehabilitated by liners with different thicknesses. According to the figure, the rehabilitated damaged pipe with a 1.5 mm CFRP liner achieves a comparable performance to that of the undamaged one. With further rehabilitation, the performance will continue to improve, but the improvement is not significant. Figure 48(b) depicts the stress nephogram of the damaged pipe without the liner. The higher stresses concentrate along the longitudinal edges of the hole, while the lower stress values are observed at the transverse edges. These findings are consistent with the research by [14]. Next, Figure 48(c) shows the comparative analysis of the displacement of the pipe. It can be observed that the CFRP liner with a thickness of 2.5 mm has optimal performance in rehabilitating damaged cast-iron pipes. The displacement nephogram shown in Figure 48(d) aligns with the stress nephogram to some extent, with the largest displacement observed at the longitudinal edges. These findings regarding the optimal liner thickness can be used for appropriate CFRP liner design in practice. The optimal design has the potential to advance the sustainability of the underground pipeline system in the U.S. by prolonging its service life and promoting its resilience against

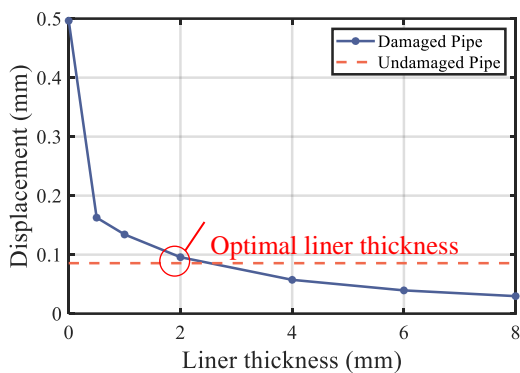
external corrosion.



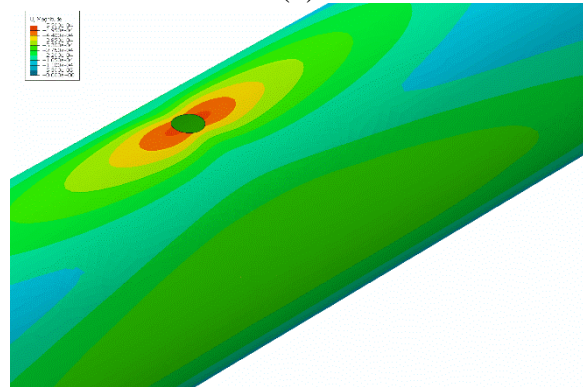
(a)



(b)



(c)



(d)

Figure 48. Mechanical performance of the damaged pipe with FEA nephograms.

For the finite element analysis of neat epoxy samples under flexural testing, the flexural stress-strain curves derived from both experimental and simulation outcomes are plotted in Figure 49. It is shown that the accuracy of the ultimate stress prediction by FEA is 99% for sample 1 and 97% for sample 2. And the residuals of stress between experimental and simulation are 3% for sample 1 and 13% for sample 2. The minor disparity is caused by the assumptions made in the elastic constitutive model of epoxy, consequently leading to the simulation's display of a linear curve until failure. Furthermore, minor deviations are inevitable during the flexural tests, due to manual pouring and the sample surface are not absolutely smooth. Overall, the FEA well predicts the three-point bending performance of neat epoxy samples, which can be used as a reliable tool for further sensitivity studies.

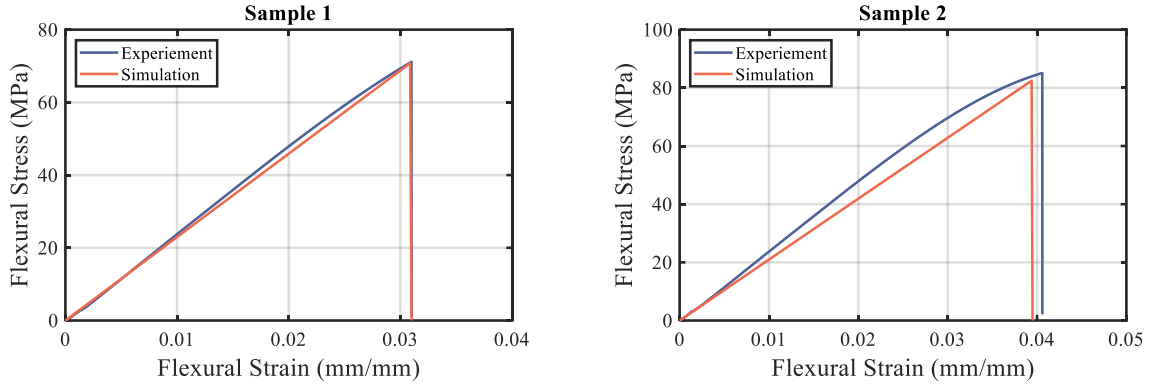


Figure 49. Comparison of three-point bending test results.

### 3.2.4.3. Findings and Conclusions

In this report, a 3D finite element model is developed to analyze the mechanical properties of the cast-iron pipelines rehabilitated by epoxy resin liners under subgrade load and internal in-pipe pressure. Various factors such as buried depth, liner thickness, and internal in-pipe pressure are analyzed through the parametric study. The findings of this study are summarized as follows: 1) A positive correlation is demonstrated between the liner thickness and rehabilitation effect. 2) Compared to the subgrade loads, the in-pipe pressure has a dominant effect on the pipeline and liner, with more than ten times impact of the subgrade loads. 3) With the rehabilitation of the structural liner, the maximum principal stress of pipeline is stable (~10 MPa) with the deep soil cover, while increases by 40 MPa with the increased in-pipe pressure from 1 MPa to 2 MPa. 4) An optimal design needs to be considered based on the pipe damage severities to balance the cost and liner rehabilitation effect.

With the increasing demand for sustainable and cost-effective pipeline solutions, the utilization of CIPP technology becomes a popular choice. Quality and performance control of CIPP liners remains a challenge. The findings of this research provide significant insights for the optimal CIPP liner design and offer valuable guidance for the trenchless construction and maintenance procedures of pipeline infrastructures.

We also investigate the effect of CFRP liner rehabilitation on aged cast-iron pipelines through finite element analysis. Considering that these pipelines have been buried underground for nearly a century, corrosion is inevitable. To study the localized damage to the entire pipe and determine the amount of CFRP needed for rehabilitation, we model corrosion as a circular hole on the middle top of the pipe. The main findings of our study can be summarized as follows:

The maximum principal stress and displacement of the pipe have a positive correlation with in-pipe pressure and a negative correlation with liner thickness. The rehabilitation effect of CFRP liner is significantly affected by its thickness. At the first 2 mm, the rehabilitation effect is significant. With further increase of the liner thickness, the rehabilitation effect is not obvious.

Compared to undamaged pipe, the damaged pipe has a similar stress and displacement response when rehabilitated by 1.5 mm and 2.5 mm CFRP liners, respectively. Further increasing the liner thickness can strengthen the pipe, but the effect diminishes after the optimal points. The maximum principal stress and displacement exhibit a similar trend around the corrosion hole. Higher values

are found at the longitudinal edges, while the lower values are located at the transverse edges.

Overall, our study provides valuable insights into the factors, liner thickness and in-pipe pressure, influencing the effectiveness of CFRP liner rehabilitation for aged cast-iron pipelines. The effect of in-pipe pressure and CFRP liner thickness, applicability to different severities of pipelines, and stress concentration areas are analyzed through the detailed FEA. These insights can enhance the design and implementation of effective CFRP liner rehabilitation strategies, ultimately contributing to the improved sustainability and resilience of aged pipelines.

### **3.3. Task 4 Enabling self-sensing for the developed CIPP structural liner**

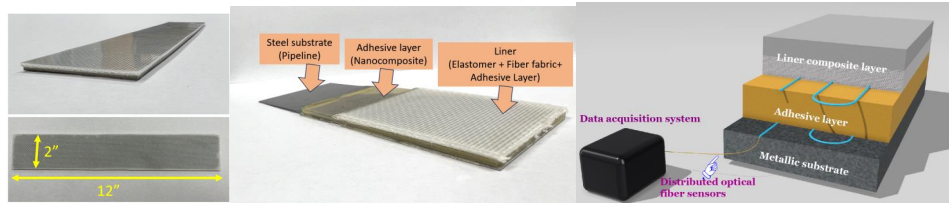
#### **3.3.1. Task 4.1 Development of embedded distributed fiber optic sensors for self-sensing structural liner**

In the continuation of our exploration, the integration of distributed optical fiber sensors within composite materials has unveiled intricate details about the behavior of structural liner systems under various conditions. The real-time data acquisition capability of these sensors has proven instrumental in capturing dynamic changes occurring during the curing process, offering insights that are pivotal for enhancing the structural integrity and longevity of these systems.

In this study, we explored the integration of distributed optical fiber sensors into composite materials, with a particular focus on structural liner systems. An optical sensor was embedded within a 12x2-inch CIPP liner specimen (as shown in Figure 50(a)), serving to monitor internal strain during the curing process.

Figure 50(b) presents the evolution of curing strain on the steel surface over a span of 36 hours, providing an overview of strain distribution across the entire specimen. To gain a more nuanced understanding of the curing process, we conducted internal curing strain measurements at two specific locations, denoted as Point 1 and Point 2, as illustrated in Figure 9(c). The strain development at Point 2 is particularly noteworthy, as it exhibited a positive strain, could be attributed to the shrinkage of the adjacent epoxy, resulting in an unusual strain pattern. Consequently, this area may be susceptible to cracking before other surface areas. Figure 9(d) further emphasizes the significance of our findings by pinpointing potential vulnerable zones within the liner.

Figure 50(e) displays the curing strain observed on the inner surface of the CIPP liner (fabric surface). The results clearly illustrate a notable disparity between the curing strain experienced on the fabric surface compared to the steel substrate. Importantly, the strain development on the fabric surface exhibits significantly higher magnitudes, encompassing both negative and positive strain values, when contrasted with the steel surface.



(a)

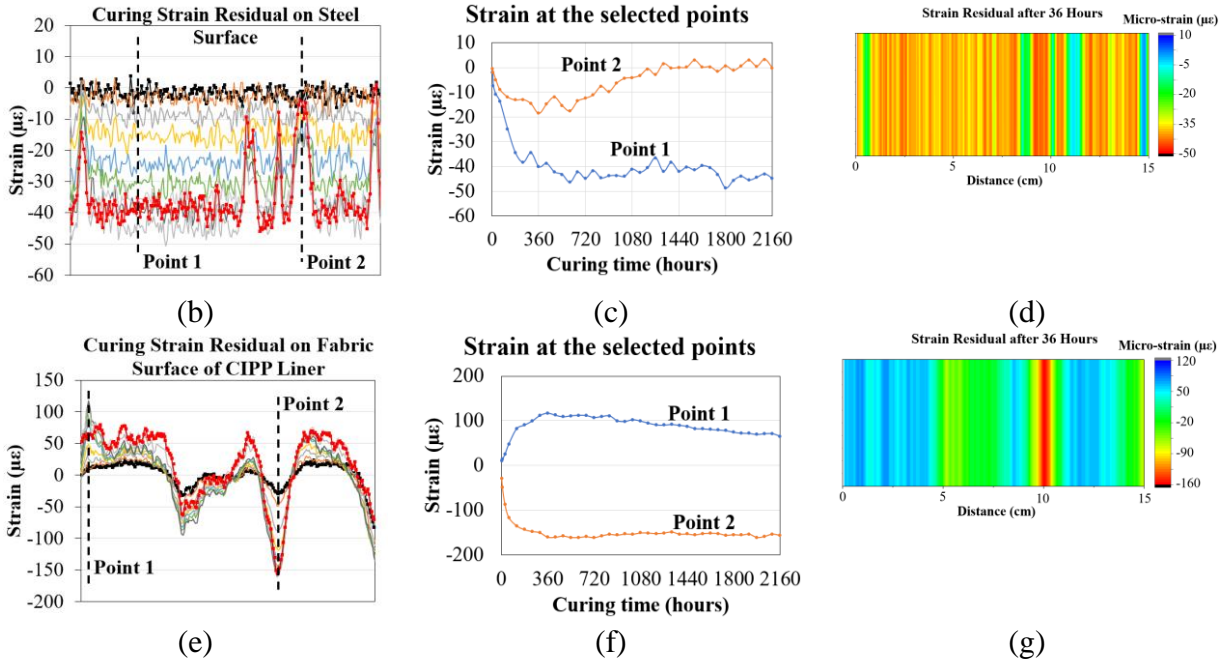


Figure 50. (a) Illustration of the CIPP sample with distributed fiber optic sensors, internal strain on (b)(c)(d) steel surface, and (e)(f)(g) CIPP liner surface.

The real-time data acquisition capability of these sensors has proven instrumental in capturing dynamic changes occurring during the curing process, offering insights that are pivotal for enhancing the structural integrity and longevity of these systems. The strain patterns observed at different locations within the CIPP liner, as captured by the embedded optical sensors, have provided a wealth of information. The positive strain at Point 2 (on steel surface), attributed to the shrinkage of adjacent epoxy, has raised questions regarding the uniformity of curing strain distribution and its implications on the overall structural integrity. This observation has instigated a deeper investigation into the material composition and sensor placement to mitigate potential vulnerabilities.

### 3.3.2. Task 4.2 Investigating the load transfer between layers of the CIPP liner and the cast-iron substrate

This study examined the integration of distributed optical fiber sensors into a CIPP liner and assessed the strain/load transfer between the layers of the CIPP liner and the steel substrate. The experimental setup, as depicted in Figure 51(a), involves a liner sample affixed to a flat steel

substrate, subjected to a three-point bending motion. Throughout this process, the distributed optical fiber sensors meticulously record the strain alterations occurring on both the steel and CIPP liner surfaces.

The results for steel and the CIPP liner are presented in Figure 51(b) and (c), respectively. Evidently, under identical bending displacements, there can be significant variation in the strain development between the CIPP liner and the steel substrate. A striking observation is the pronounced variation in strain development between the two layers under identical bending displacements. For the steel surface, the strain gravitates towards zero at the end of the measured range, with the peak strain, approximately 90 micro strain, situated at the midpoint of the range. In contrast, the liner surface exhibits a strain value of around 80 micro strain at the extremity, with the maximum soaring over 250 micro strain. Additionally, the contrasting strain patterns underscore a complex interplay of mechanical properties and stress distribution between the CIPP liner and steel substrate. The steel, with its inherent rigidity and strength, exhibits a more uniform and restrained strain pattern. In contrast, the CIPP liner, characterized by its flexibility and composite nature, exhibited some sharp peaks in the strain. These findings can provide valuable insights for the research team in understanding the relationship between collected strain values in the CIPP liner and the steel substrate.

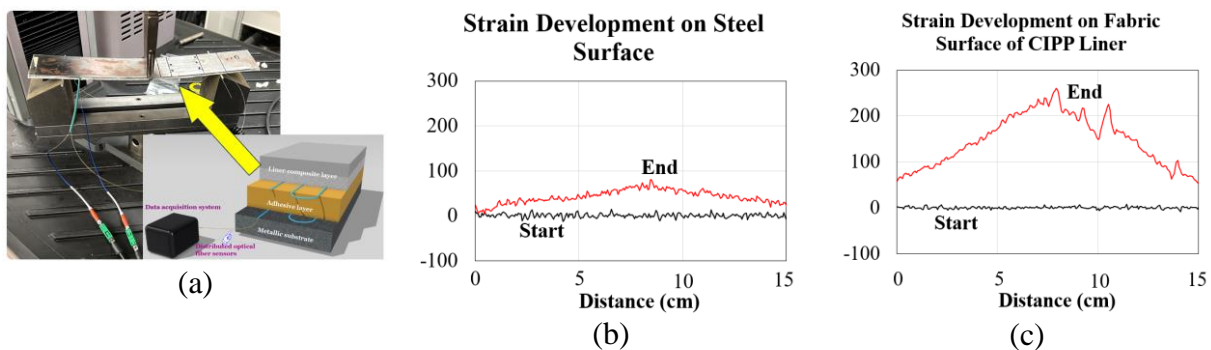


Figure 51. (a) Illustration of the CIPP sample with distributed fiber optic sensors, strain development under displacement on (b) steel surface, and (c) CIPP liner surface.

### 3.4. Task 5 Integration of the multifunction with the pipeline integrity management system

#### 3.4.1. Task 5.1 Development of CIPP liner risk index for the pipeline integrity management enhanced by AI algorithms

##### 3.4.1.1. Best model selection

The “Facility”, “Leak detection”, “Age years”, “Pipe diameter”, “Land use”, and “Facility part” are considered in the subset analysis. The MINITAB statistical package is used to identify the best linear regression model. As shown in Table 11, there are 11 model types with 6 variables. The Mallows  $C_p$  value compares the accuracy and bias of the full model to a model with a subset of predictor variables, as shown in Equation (2) [37,38].

$$C_p = \frac{SSE_p}{MSE(full)} + 2p - n \quad (2)$$

where  $n$  is the total sample size,  $p$  is the number of regression parameters in the model,  $SSE_p$  is the sum of squared errors for model  $p$ , and  $MSE(full)$  is the variance of the residuals of a model containing all possible predictor variables. When the model bias is zero,  $C_p$  value equals to  $p$ . Therefore, smaller value difference between  $C_p$  and  $p$  indicates better model performance [15], [16]. For model type 11 in Table 11, the value of  $p$  (7) equals to the value of  $C_p$  (7) with zero value difference. Thus, we consider all six variables in the multivariable linear regression model for better prediction accuracy.

Table 11 Best model type.

Model type	Factors	$p$	Mallows $C_p$	Pipe diameter	Leak detection	Facility	Facility part	Age years	Land use
1	1	2	25.4			*			
2	1	2	88.1					*	
3	2	3	14.5	*		*			
4	2	3	19.8			*		*	
5	3	4	9.4	*		*		*	
6	3	4	9.5	*	*	*			
7	4	5	4.1	*	*	*		*	
8	4	5	10.2	*	*	*	*		
9	5	6	5.4	*	*	*	*	*	
10	5	6	5.8	*	*	*		*	*
11	6	7	7.0	*	*	*	*	*	*

### 3.4.1.2. Regression model establishment

The multivariable linear regression process is programmed in Matlab for model type 11. We randomly train 75% of the total data (584/799) to get the multivariable linear regression equation as shown in Equation (3) and use 25% of the total data (195/799) to test the algorithm.

$$y_{Failure\ type} = 4.2411 - 0.2823x_{PD} + 0.0896x_{LD} - 0.8193x_F + 0.0300x_{FP} + 0.1973x_{AY} - 0.0978x_{LU} \quad (3)$$

where,  $x_{PD}$  is the scale value of “Pipe diameter”.  $x_{LD}$  is the scale value of “Leak detection”.  $x_F$  is the scale value of “Facility”.  $x_{FP}$  is the scale value of “Facility part”.  $x_{AY}$  is the scale value of “Age year”.  $x_{LU}$  is the scale value of “Land use”.

The total original test data contains 195 groups of data, but there are some missing data in the dataset. After removing invalid data points, there are 115 groups of data left. As the category data the failure type must be integers, we round up the output values to for the prediction results. Figure 52(a) shows the comparison of predicted test data from MVLRL algorithm and the true value in the test data. While there is some deviation between predicted and true values, the regression values

are clustered around the true values. Figure 52(b) illustrates the random 30 data groups' regression results obtained from the results dataset. The true value matches well with the regression value.

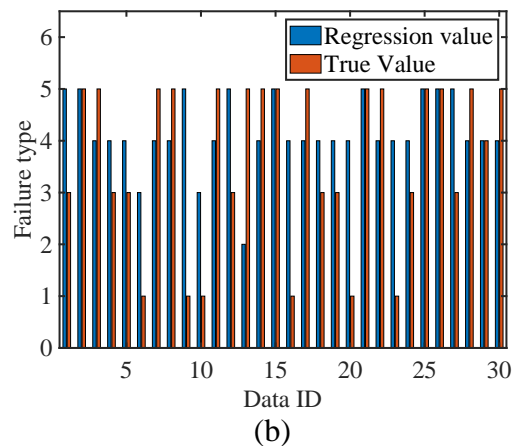
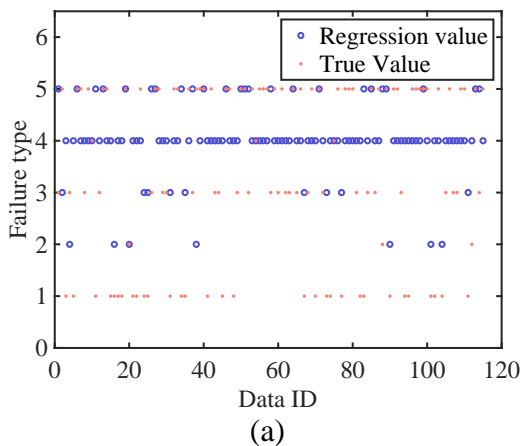
### 3.4.1.3. Residual analysis

In the residual analysis, the upper and lower bounds are obtained by polynomial fitting of the confidence intervals of the residuals. In Figure 52(c), the standardized residuals for all trained data are presented, with only 8 residual outliers that are outside the upper and lower bounds. The percentage of outliers is 1.5%, indicating that the results are normal. In addition, the residuals are scattered around the zero line, indicating that the linear regression model can fit the real values well.

### 3.4.1.4. Assumption verification

Three assumptions for multivariable linear regression analysis are verified as follows. In the best model selection part, correlation analysis reflects the linear relationship between two variables. A low absolute correlation coefficient indicates a low linear relation between two variables. We remove three low absolute correlation coefficient variables and keep the six high absolute correlation coefficient variables. In this way, the assumption a) is satisfied.

The normal P-P plot reflects the degree of conformity between the actual cumulative probability of a variable and the theoretical cumulative probability and can be used to examine whether the data obey a certain distribution type. If the data demonstrates a normal distribution, the data points should largely coincide with the theoretical straight line. We get normalized residual data from SPSS and then draw the normal P-P plot of standardized residuals. Figure 52(d) shows the cumulative distribution function (CDF) of the residual data. The distribution of residuals ranges from zero to one. The residual trend (blue point) is close to the theoretical straight line (red line), which means the residuals are normally distributed in this model. Therefore, assumption b) is verified.



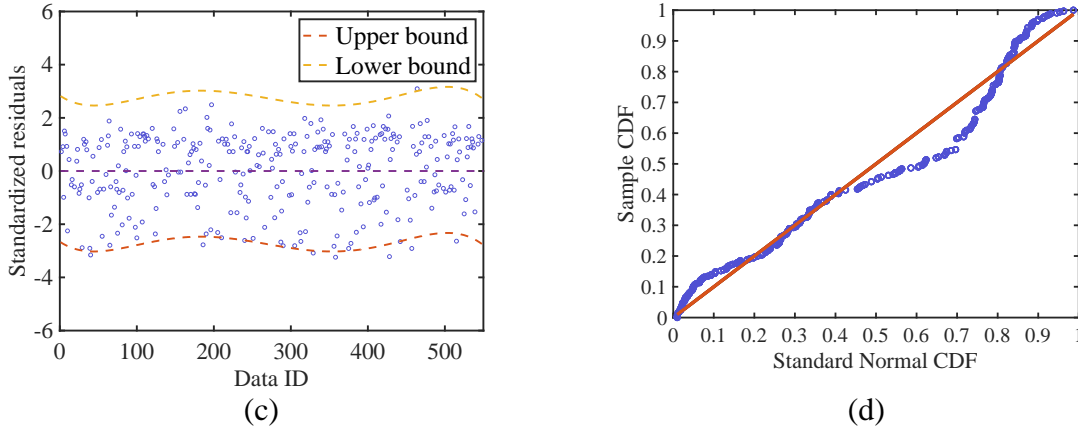


Figure 52. Failure type MVLN prediction results (a) comparison between MVLN results and true value in the test data; (b) bar chart of the comparison. Residual analysis: (c) plot of standardized residuals; (d) normal P-P plot of standardized residuals.

We use Variance Inflation Factor (VIF) values to test whether the predictor variables are correlated with each other. According to the interpretation role of the VIF [41], six predictor variables are found to be moderately correlated, as shown in Table 12. However, the largest VIF value was 1.214, which is very close to 1, indicating a lack of correlation among the variables, and thereby indicating that assumption c) is verified.

Table 12 VIF of predictor variables.

Predictor variable	Statistics VIF
Pipe diameter	1.060
Leak detection	1.044
Facility	1.176
Facility part	1.083
Age years	1.123
Land use	1.214

### 3.4.1.5. Findings and conclusions

The objective of this report is to develop efficient risk assessment models for pipelines by applying the machine learning approaches. Based on the literature on various factors and models of pipeline risk, we establish three machine learning-based risk model through MVL. Eight influencing factors are considered: “Facility”, “Leak detection”, “Age years”, “Pipe diameter”, “Land use”, “Facility part”, “Service”, and “Gross”. The pipeline failure types are predicted through the developed machine learning models. The MVLN results show that 25% of testing data aligns well with the real values, with only 1.5% of the residual outliers. In addition, the distribution of residuals ranges from zero to one and matches the theoretical straight line well. The biggest VIF value (1.214) for the predictor variable is close to one, which means the influencing factors are not highly correlated with each other. According to the results, the MVLN, GPR and SVM are reliable machine learning algorithms for pipeline risk evaluation.

#### 4. Future work

In Year 2, according to the planned schedule as shown in Table 13, the major future work as aligned include:

- (1) Complete 90% of Task 2 Development of healable and sustainable CIPP structural liner. Specifically, for Task 2, the mechanical properties of the resin with varying reactive diluent and catalyst content will be investigated to further narrow down the self-healing resin formulation. Work will be done to quantify self-healing tests so that properties between formulations can be compared. Work will also be done to decrease the temperature requirement for self-healing to bring it below a temperature that will not damage the liner. This resin will also be tested in nanoparticle composites, woven fabric composites, and with a commercial liner.
- (2) Complete 80% of Task 3 Enhancing mechanical and bonding performances and reducing permeability of the healable CIPP structural lining through nanofiller. Specifically, for Task 3, further experimental research on CNT, GNP, and ND will be carried out, focusing on their reinforcing capabilities. In addition, the underlying mechanisms of reinforcement will be investigated. Simultaneously, alternative dispersion methods, such as employing surface modification agents, will be explored. The nanoparticle distribution and the performance of the resulting nanocomposites will be assessed. Consequently, a comparative analysis will be conducted between nanocomposites fabricated using surface modification dispersion techniques and those employing mechanical dispersion methods, as reported in this study.
- (3) Complete 70% of Task 4 Enabling self-sensing for the developed CIPP structural liner. Specifically, for Task 4, the data gathered on curing strain residuals and strain resulting from mechanical deformation across various layers of CIPP liners has proven the efficacy of the sensors in pinpointing areas prone to early structural vulnerabilities. The real-time data acquisition facilitated by these embedded sensors is crucial, providing dynamic insights into strain variations and enabling informed decisions for enhancing structural integrity. The future studies are planning to integrate these sensors with CIPP liners that are augmented with nano-reinforcements. This advancement aims to explore the compounded benefits of enhanced material strength and real-time monitoring.
- (4) Complete 60% of Task 5 Integration of the multifunction with the pipeline integrity management system. Specifically, for Task 5, in this report, the quantitative values are normalized based on experience. The developed models are meaningful for pipeline failure assessment. It can evaluate the pipeline risk conditions and predict the failure types based on observed categorical and numerical data, which is meaningful for the long-term development of pipeline service in society, the environment, and the economy. It can also help pipeline operators to manage risks in an effective and efficient way which will promote the safety and sustainability of pipeline operations in the future. The future study will focus more on risk assessment by considering liner failure risk, in-service risk, construction and environmental risk.

(5) Complete 70 % of Task 6 Reporting and student mentoring. Specifically, complete four quarterly reports, one annual report for Yr 2, mentor the postdoc, graduate students, and undergraduate students for this project.

Table 13 Project schedule for Yr 2

Tasks (Milestones, Completion Date)	Year 1				Year 2				Year 3			
	Q1	Q2	Q3	Q4	Q1	Q2	Q3	Q4	Q1	Q2	Q3	Q4
Task 1 (Milestone 1) (M.1: 01/10/2023)	x											
Task 2 (Milestone 2) (M.2: 10/10/2024)	x	x	x	x	v	v	v	v				
Task 3 (Milestone 3) (M.3: 01/10/2025)	x	x	x	x	v	v	v	v				
Task 4 (Milestone 4) (M.4: 04/10/2025)		x	x	x	v	v	v	v				
Task 5 (Milestone 5) (M.5: 07/10/2025)			x	x	v	v	v	v				
Task 6 (Milestone 6) (M.6: 09/30/2025)	x	x	x	x	v	v	v	v				

## **References**

- [1] Farrag K. Evaluation of Structural Liners for the Rehabilitation of Liquid and Natural Gas Piping Systems. 2015.
- [2] Primus Liner Product Specifications, Liners by Primus Line® n.d. <https://www.primusline.com/en/product/liner>.
- [3] Fiberspar Pipeline, Engineering Guide, Section 1.2. n.d. [www.fiberspar.com](http://www.fiberspar.com).
- [4] The Starline Trenchless Technology n.d. [http://www.starlinett.com/products/frame\\_cip.html](http://www.starlinett.com/products/frame_cip.html).
- [5] Fu G, Shannon B, Rathnayaka S, Deo R, Kodikara J. State of the art literature review on CIPP liners. Melbourne, Australia: Monash Univ 2020.
- [6] Stewart HE, O’rourke T, Wham B, Netravali A, Argyrou C, Zeng X, et al. Performance testing of field-aged cured-in-place liners (CIPL) for cast iron piping. Ithaca, NY: Cornell Univ 2015.
- [7] Allouche EN, Bainbridge K, Moore ID. Laboratory examination of a cured in place pressure pipe liner for potable water distribution system. North American Society for Trenchless Technology (NASTT) NO-DIG 2005.
- [8] Downey D, Heavens J, Ngo S. Principles and practice for the design and selection of pressure pipe lining systems. Proc. North American Society for Trenchless Technologies No-Dig Show and Exposition, 2007.
- [9] Alam SZ. Experimental and numerical evaluation of cured in place pipe lining system for high temperature applications in sewer pipes. Louisiana Tech University; 2011.
- [10] Sahu SK, Rama Sreekanth P. Mechanical, thermal and rheological properties of thermoplastic polymer nanocomposite reinforced with nanodiamond, carbon nanotube and graphite nanoplatelets. *Advances in Materials and Processing Technologies* 2022;8:2086–96.
- [11] Sahu SK, Badgayan ND, Sreekanth PR. Rheological Properties of HDPE based thermoplastic polymeric nanocomposite reinforced with multidimensional carbon-based nanofillers. *Biointerface Res Appl Chem* 2022;12:5709–15.
- [12] Systemes D. ABAQUS/CAE User’s Manual, Version 6.14. Providence, RI: Dassault Systemes Simulia Corp 2014.
- [13] Mosadegh A, Nikraz H. Finite Element Analyses of Buried Pipeline Subjected to Live Load Using ABAQUS 2015.

- [14] Lu H, Wu X, Ni H, Azimi M, Yan X, Niu Y. Stress analysis of urban gas pipeline repaired by inserted hose lining method. *Composites Part B: Engineering* 2020;183:107657.
- [15] Patel H, Salehi S. Structural integrity of liner cement in oil & gas wells: Parametric study, sensitivity analysis, and risk assessment. *Engineering Failure Analysis* 2021;122:105203.
- [16] Babuska I, Szabo B. On the rates of convergence of the finite element method. *International Journal for Numerical Methods in Engineering* 1982;18:323–41.
- [17] Melchers RE. Post-perforation external corrosion of cast iron pressurised water mains. *Corrosion Engineering, Science and Technology* 2017;52:541–6.
- [18] Jia L-J, Kuwamura H. Ductile fracture simulation of structural steels under monotonic tension. *Journal of Structural Engineering* 2014;140:04013115.
- [19] Larive J. Performance of European cross-country oil pipelines. Statistical summary of reported spillages in 2006 and since 1971 2008.
- [20] Grant SW, Collins GS, Nashef SAM. Statistical Primer: developing and validating a risk prediction model†. *European Journal of Cardio-Thoracic Surgery* 2018;54:203–8. <https://doi.org/10.1093/ejcts/ezy180>.
- [21] Ec A. *Introduction to Multivariate Regression Analysis* 2010.
- [22] Poole MA, O’Farrell PN. The Assumptions of the Linear Regression Model. *Transactions of the Institute of British Geographers* 1971:145. <https://doi.org/10.2307/621706>.
- [23] Ma P-C, Siddiqui NA, Marom G, Kim J-K. Dispersion and functionalization of carbon nanotubes for polymer-based nanocomposites: A review. *Composites Part A: Applied Science and Manufacturing* 2010;41:1345–67. <https://doi.org/10.1016/j.compositesa.2010.07.003>.
- [24] Alian A, Meguid S. Molecular dynamics simulations of the effect of waviness and agglomeration of CNTs on interface strength of thermoset nanocomposites. *Physical Chemistry Chemical Physics* 2017;19:4426–34.
- [25] Jiang J, Oberdörster G, Biswas P. Characterization of size, surface charge, and agglomeration state of nanoparticle dispersions for toxicological studies. *Journal of Nanoparticle Research* 2009;11:77–89.
- [26] Kim JG, Yun T, Chae J, Yang GG, Lee GS, Kim IH, et al. Molecular-level lubrication effect of 0D nanodiamonds for highly bendable graphene liquid crystalline fibers.

ACS Applied Materials & Interfaces 2022;14:13601–10.

- [27] Alexopoulos ND, Paragkamian Z, Poulin P, Kourkoulis SK. Fracture related mechanical properties of low and high graphene reinforcement of epoxy nanocomposites. *Composites Science and Technology* 2017;150:194–204.
- [28] Chen J, Zhu N, Niu F, Peng Y, Su J, Zhu Y. Influence of agglomerated diamond abrasive wear on sapphire material removal behavior. *Diamond and Related Materials* 2020;108:107965.
- [29] Sousa MF, Loureiro HC, Bertran CA. Anti-scaling performance of slippery liquid-infused porous surface (SLIPS) produced onto electrochemically-textured 1020 carbon steel. *Surface and Coatings Technology* 2020;382:125160.
- [30] Buch V. Path integral simulations of mixed para-D<sub>2</sub> and ortho-D<sub>2</sub> clusters: The orientational effects. *The Journal of Chemical Physics* 1994;100:7610–29.
- [31] Frost H, Düren T, Snurr RQ. Effects of surface area, free volume, and heat of adsorption on hydrogen uptake in metal-organic frameworks. *The Journal of Physical Chemistry B* 2006;110:9565–70.
- [32] Cracknell RF. Molecular simulation of hydrogen adsorption in graphitic nanofibres. *Physical Chemistry Chemical Physics* 2001;3:2091–7.
- [33] Yang Q, Zhong C. Molecular simulation of adsorption and diffusion of hydrogen in metal-organic frameworks. *The Journal of Physical Chemistry B* 2005;109:11862–4.
- [34] Shou KJ, Chen BC. Numerical analysis of the mechanical behaviors of pressurized underground pipelines rehabilitated by cured-in-place-pipe method. *Tunnelling and Underground Space Technology* 2018;71:544–54.
- [35] Association AWW. *Steel pipe: a guide for design and installation*. vol. 11. American Water Works Association; 2004.
- [36] Fang H, Yang K, Li B, He H, Xue B. Parameter analysis of wall thickness of cured-in-place pipe linings for semistructured rehabilitation of concrete drainage pipe. *Mathematical Problems in Engineering* 2020;2020.
- [37] Hocking RR. A Biometrics Invited Paper. The Analysis and Selection of Variables in Linear Regression. *Biometrics* 1976;32:1. <https://doi.org/10.2307/2529336>.
- [38] Olejnik S, Mills J, Keselman H. Using Wherry's Adjusted  $R^2$  and Mallows's  $C_p$  for Model Selection From All Possible Regressions. *The Journal of Experimental Education* 2000;68:365–80. <https://doi.org/10.1080/00220970009600643>.

- [39] Senouci A, Elabbasy M, Elwakil E, Abdrabou B, Zayed T. A model for predicting failure of oil pipelines. *Structure and Infrastructure Engineering* 2014;10:375–87. <https://doi.org/10.1080/15732479.2012.756918>.
- [40] Zuccaro C. Mallows' Cp Statistic and Model Selection in Multiple Linear Regression. *Market Research Society Journal* 1992;34:1–10. <https://doi.org/10.1177/147078539203400204>.
- [41] Daoud JI. Multicollinearity and Regression Analysis. *J Phys: Conf Ser* 2017;949:012009. <https://doi.org/10.1088/1742-6596/949/1/012009>.